Functionally Graded 3D-Printed Scaffolds through Direct Ink Writing: Bridging Ceramics and Metals for Enhanced Multifunctionality

Maarten Harmen Zwart

TU Delft

Functionally Graded 3D-Printed Scaffolds through Direct Ink Writing: Bridging Ceramics and Metals for Enhanced Multifunctionality

Master thesis

by

Maarten Harmen Zwart

Master thesis:	
Supervisors:	Prof. dr. Amir A. Zadpoor, dr. Niko E. Putra, Sara Panahkhahi, dr. Mohammad J. Mirzaali
Supporting supervisor:	Lorenzo Kunkels
Committee:	Prof. dr. Amir A. Zadpoor, dr. Peyman Taheri, dr. Mohammad J. Mirzaali
Defense date:	March 8, 2024
Place:	Faculty of Mechanical, Maritime and Materials Engineering, Delft
Student number:	4569563

Abstract

Over two million bone grafts are performed worldwide, each year. The preferred method is using auto-grafts, but there are two important downsides. There is often insufficient tissue to harvest and the scar at the harvesting side is painfull for the patient. Therefore there exists a great need to improve synthetic grafts.

Traditionally, synthetic bone scaffolds are made from only one material, this can either be a (bioactive) ceramic or metals. The former has the benefit of promoting bone growth, but has insufficient mechanical properties. Metals on the other hand have no issue competing with bone in terms of mechanical properties, but they may not be biocompatible nor aid osteo-induction.

In this study direct ink writing was used to produce multimaterial Ti6Al4V and akermanite scaffolds. The goals was to combine the favourable mechanical properties of Ti6Al4V alloy with the osteo-inductive properties of akermanite. Composites of Ti6Al4V and akermanite were evaluated as well, but similar to akermanite ceramic on itself, their mechanical performance was deemed insufficient. Akermanite and Ti6Al4V was found to react and form titanium silicide and a calicum compound, presumed to be calcium oxide. A core shell scaffold was designed which uses a Ti6Al4V shell and an akermanite composite core in order to achieve both adequate mechanical and improved bioactive properties. This scaffold performed comparable to cortical bone in stiffness, and boasted superior strength.

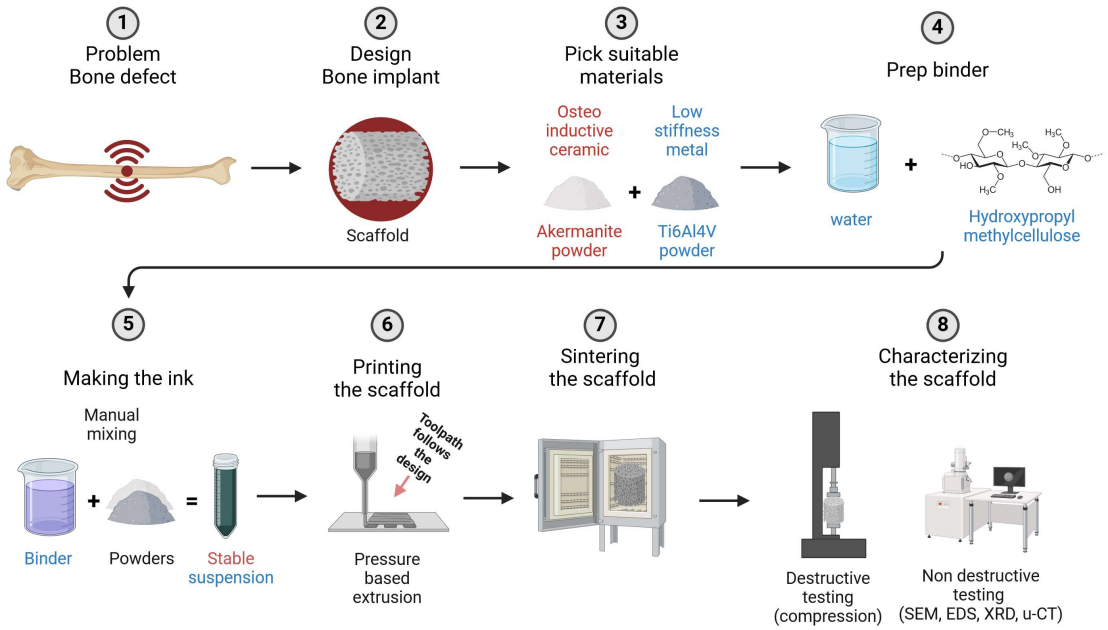

Figure 1: Graphical abstract describing the research flow from problem statement to characterizing the the created scaffolds. Made using BioRender.com

Contents

1 Introduction

1.1. Problem statement and clinical relevance

Musculoskeletal tumours, infections and trauma can lead to large bone defects [1]. This type of defect is unable to heal on fully without intervention. Treatment options rely on grafts, which can minimize the need for amputations and may provide a better functional outcome for the patient. Various types of grafts exists, namely, autografts, allografts and synthetic grafts. There are a number of downsides to using autografts, however, they are still the preferred option [2] over synthetic biomaterials. With over two million bone grafts performed worldwide, each year [3], there is a great need to improve synthetic bone implants.

While autografts are often considered the preferred option because of their perfect histocompatibility, often, insufficient can be harvested from the patient. Additionally, autografts cause greater patient discomfort due to the removal of tissue at a harvesting site. An allograft on the other hand may be rejected because of low histocompatibility [1]. Synthetic bone implants aim to mimic the mechanical and functional properties of bone. For the mechanical properties bio-inert metals, such as, Ti6Al4V have been used. In order to promote bone in-growth, bone-like ceramics may be added.

Engineered porosity can be used as a means to lower the overall mechanical properties of metal implants, such that, they can be used in biomedical applications [4]. Additionally, the porosity can also be used to promote bone in-growth [5, 6]. In this study Ti6Al4V was chosen for it's high strength, low stifness, good corrosion resistance and related biocompatability. Through engineered porosity the effective stiffness can be altered, to increase compliance and reduce stress-shielding effects. Mechanical properties such as stiffness largely depend on density according to the Gibson and Ashby model [7, 8]. Design is a common method of incorporating macroscale porosity, on the microscale in powder metallurgy the sintering conditions can also be used.

Mechanical properties similar to bone are just one of the requirements for a proper bone implant, another property perhaps as important is stimulating osteoinduction. For promoting bone in-growth merely choosing a large pore size is insufficient. Materials which aid osteoinduction are, generally, similar to bone. Candidates include ceramics like hydroxyapatite, tricalcium phosphate and akermanite. In this study akermanite will be used exclusively, as hydroxyapatite was found to be unstable when sintered in proximity of Ti6Al4V. The interested reader is encouraged to check out Appendix C which covers that endeavour.

Akermanite is a naturally occurring mineral that promotes osteo-induction [9] similar to hydroxyapatite. Unlike hydroxyapatite [10] though, there is no indication that akermanite decomposes below it's melting point [11]. The chemical formula of akermanite is $Ca_2MgSi_2O_7$, as such, it isn't substantially different from hydroxyapatite which also contains phosphate and hydroxide groups. The orthosillicate group (Si_2O_7) and magnesium on the other hand are exclusive to akermanite.

In this thesis, we seek to answer three research questions related to metallic bone scaffolds complemented with ceramics:

- Can mechanical properties similar to that of bone be obtained with Ti6Al4V through design and sintering conditions?

- Will interfaces between Ti6Al4V and akermanite-Ti6Al4V composite successfully bond?
- Do these multifunctional scaffolds still have sufficient mechanical properties compared to bone?

For each of these three questions an initial hypothesis was formed. The first hypothesis was that extrusion based 3D printing would be a capable process for reducing the density through design. And, manipulating the sintering conditions ought to have significant influence as well. Second, since both the pure Ti6Al4V and the composite contain Ti6Al4V, the interface is expected to bond, to some degree. Third, the mechanical properties of multifuctional multimaterial scaffolds will depend on those of the individual parts and the design, with strong Ti6Al4V alloy in both parts it is expected to perform well.

Besides these research questions, Appendix B describes a new ink and process. These methods don't quite fit in with the three research questions mentioned earlier, but are certainly worth a read for the curious reader after the main matter. These texts discus new methods (metastable ink, layer desiccation), and new software tools for the printer used in this study (A processing script for Cura, a modern slicer). Additionally, it closely tracks with the recommendations for developing a more versatile printing platform in the discussion.

2

Materials and methods

2.1. Introduction

In this chapter, the procedures employed for manufacturing and testing Ti6Al4V, mixed material and mixed multi-material scaffolds is presented. It begins with a carefully chosen but rather simple scaffold design, similar in geometry as has been used in earlier works by others. One such work, which did not only have similar geometry, but also tried porosity grading through design came from Diloksumpan et al [12]. That study had a number of similarities to the work done in this thesis project, such as: employing the same manufacturing technology[1], using similar spacing and attempting to include an apatite into the scaffold. Initially this thesis project differentiated itself by looking into much stronger metallic scaffolds, featuring more gradual grading[2], exploring lowering stiffness through intentional partial sintering and address the multi material interface. Because of some inexplicable results for density graded scaffolds the focus was changed, to instead be on multimaterial scaffolds. The work done on density/stiffness grading through design can be seen in Appendix A.

After the design is introduced the chapter continues with the materials and methods used for manufacturing semi-finished scaffolds. Then follows a section on the post processing required, and what parameters need to be tuned in order to achieve partial sintering. The remaining sections focus on characterization of porosity, mechanical properties, structure and morphology through SEM imaging, EDS analysis, CT imaging and XRD analysis. These characterizations are important in order to understand the mechanical properties such as strength, stiffness and brittleness[3]. And, verify geometrical structure, as well as chemical composition.

2.1.1. Introduction to Direct ink writing/Extrusion-based 3D printing

Extrusion based 3D printing in particular direct ink writing (DIW) [13] is an additive manufacturing process where material is extruded out of a nozzle. It has the benefits of being low cost, versatile and having low process complexity. Its versatility comes from two aspects: the wide range of materials that can be printed (with some post processing), and the ease with which multi material printing is possible. Metals, ceramics and polymers have all been successfully processed using this additive manufacturing technique. One of it's major downsides are the inherent low precision due to nozzle related minimal linewidth and the start-stop process behaviour.

At least four factors set it apart from inkjet technologies, which can create pixel-like single spots of material. These factors are: start break, a period before ink flows out, stop break, a period until oozing stops, flowrate discrepancies when the printhead changes velocity, and ink deformation during and after extrusion. There has been an effort in recent years particularly from consumer 3D printing groups to overcome the first three issues. A technique called pressure advance (PA) [14] sometimes also called linear advance was developed. This technique takes into account the compression energy put into the material essentially treating it like a spring system [15, 16]. Instead of assuming the flowrate is correct

[1] Although, a different printer (RegenHU, Villaz-St-Pierre, Switzerland) was used.

[2] With increases in spacing of less $7\,\mu m$ per layer instead of $100\,\mu m$.

[3] Brittleness is related to energy absorption before breaking, in other words, the area under the stress-strain graph up to yield.

based on the printer specific volumetric extrusion mechanism, pressure advance tries to preemptively start and stop the extrusion to actually match the desired flowrate. This preemptive correction can be seen in Figure 2.1. Before flow is required material is already being pushed in, but before the move is finished material is also already pulled out. When done correctly the intended amount of material gets deposited this means that it potentially solves three out of four process non-idealities.

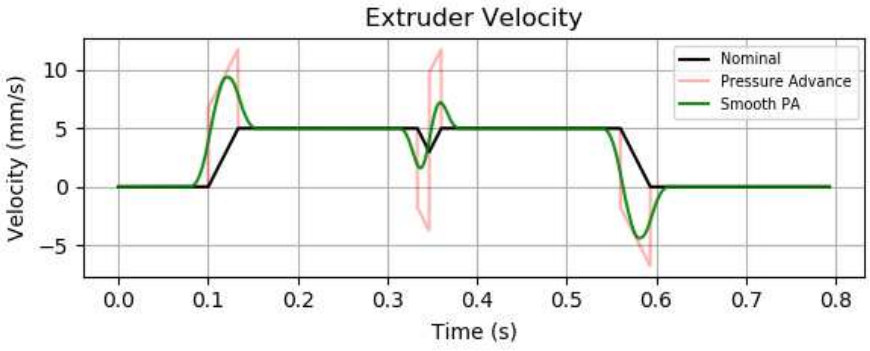

Figure 2.1: Pressure advance kinematics as used in the Klipper project reproduced from [17].

The fourth issue that prevents DIW from producing spot/pixel like depositions is ink deformation. When ink is extruded a number of forces are applied to it: driving forces pushing it out of the nozzle, ground reaction forces from the print surface, shear forces from the side to size movement and internal forces. The last two are detrimental, because ink does not end up only directly under the nozzle, when it can be easily spread around instead. Non-zero tear stress makes the ink stick to itself creating smearing and tear-off artifacts. Resistance to tearing can be a useful property when printing overhangs but these artifacts raise doubts about whether this rheology choice is optimal.

Besides precision there is also accuracy, in other words how close are the printed structure to their CAD-model counterpart. Nozzle size, machine kinematics, semi-stochastic events and machine instructions, among others, are factors in this. Nozzle size and machine movement are almost trivial; if the toolpath deviates from the demanded toolpath, inaccuracy is the inevitable result. Semi-stochastic phenomena, however, are not trivial, and can include events such as air pockets in the ink, clogging, and inconsistencies in the ink. These events are not truly stochastic though, as ink preparation and handling before printing sets them up to occur.

Direct ink writing is a versatile process but not without its flaws. While the technique is still in it's infancy in the sense that it has seen limited commercial adoption, it has already seen widescale use in research and small scale prototyping. If shortcomings like high variability (due to inaccuracy) and poor resolution are mitigated it could become a useful tool for multimaterial additive manufacturing. And open up research possibilities into advanced multimaterial biomedical implants which can not be made by any other manufacturing technique.

2.2. Scaffold design

Scaffold design for this research was done such that they'd be suitable for pressure driven extrusion-based 3D printing. A software package delivered with the printer named GeSiM Robotics (GeSiM Bio-instruments, Germany) was used to design the scaffolds. The shape of the scaffold was chosen to be cylindrical with a diameter of 10 mm and a height of almost 10.5 mm. Every layer was sliced such that it could be printed as 1 continuous line, the design linewidth was 410 µm and the line distance was between 400 µm. Every layer except the first was 328 µm thick for a total of 32 layers, the first one was approximately 280 µm thick to ensure good adhesion. Neither layer height nor line distance were chosen arbitrary, these were chosen such as to fall into a range favourable for bone in-growth [18]. For this pores needed to be bigger than 100 µm, but preferably >300 µm.

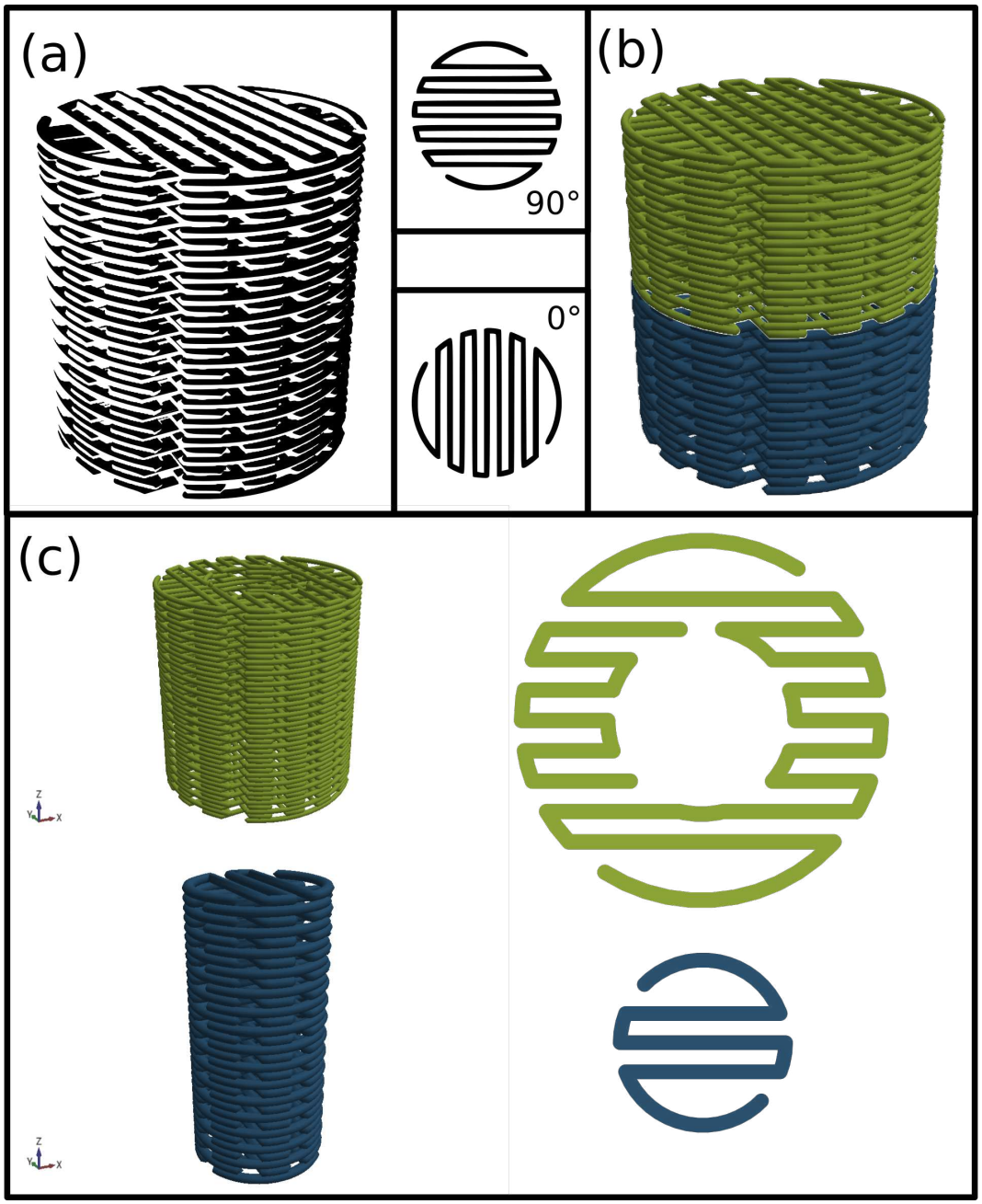

Figure 2.2: Two geometrically unique designs: (a) Ungraded design with 400 µm strut spacing. It will be produced from Ti6Al4V (Ti) and Ti6Al4V + Akermanite composite (TiAk), and has a 90° shift in layer direction between layers. (b) A half-half (HH) design where the top half consists of Ti6Al4V and the bottom has added akermanite. (c) Core-shell (CS) designs where the Ti offers strength and the TiAk composite promotes bone in-growth. It was produced with a Ti core and TiAk shell, and vice versa.

There were two geometrically unique designs. The first (Figure 2.2a) was the simplest as it consisted of only one material or half-half (Figure 2.2b). Every layer a 90° angle shift between layers occurs so that printed lines are perpendicular with each other. The second geometrically unique design (Figure 2.2c) consists of two parts, a core and a shell. From here on out Ti6Al4V, akermanite, Ti6Al4V + akermanite composite, half half and core shell will be abbreviated where appropriate as Ti, Ak, TiAk, HH, CS, respectively. For the core shell the material of the core will be specified first and then the material of the shell, for example: CS (Ti) (TiAk). With the different material compositions this brings the total number of designs to five: Ti, TiAk, HH, CS (Ti) (TiAk) and CS (TiAk) (Ti).

For clarity when we speak of multimaterial two distinct compounds are meant, so while the TiAk has the materials Ti6Al4V and akermanite it is only one compound. The HH scaffold was the same as the $400\,\mu$m design mentioned earlier, with the exception that from the 17^{th} layer onward the material changes to the second mixture. The CS scaffolds consisted of a $5\,$mm core and a shell going from $5\,$mm to $10\,$mm, with either Ti or TiAk forming the core. The choice of this shell thickness wasn't arbitrary but was similar to medial part of the femur [19].

Initially the goal had been to also look into grading in density as a means to manipulate stiffness. To investigate this scaffolds with line spacing of $200\,\mu$m and with variable line spacing between $200\,\mu$m and $400\,\mu$m were designed, and made. Ultimately, the results obtained from this were counter intuitive, and simply impossible to defend without explanation for the behaviour. In summary the design with $200\,\mu$m line spacing was stiffer as the coarser $400\,\mu$m design as expected. However, the density graded design was stiffer than both, an unexpected result we were unable to explain without simulations. These results can still be seen in Appendix A.

2.3. Ink formulations and preparation

Methylcellulose (MC) and hydroxypropyl methylcellulose (HPMC) are polymers derived from cellulose, which unlike regular cellulose are water soluble. These are commercially available in varying molecular weights and hydroxypropyl substitution degree, and are widely used [20, 21, 22] either as a drug delivery aid, binder, or as a rheology modifier. In this study it was used to improve ink stability and as a binder.

For this study viscous inks were prepared from titanium alloy (Ti6Al4V) powder, akermanite powder and binder. To prepare a 5.5w% binder solution, first $150\,$mL of distilled water was heated to $80\,^{\circ}$C. To a beaker $5.8\,$g of HPMC (H7509, Sigma-Aldrich, Germany) powder was added. After the water temperature had reached $80\,^{\circ}$C, exactly $100\,$g[4] was transferred to a clean beaker. A stirbar was added, and it was heated again to $70\,^{\circ}$C. Stirring was applied with a rate of 500 RPM. Slowly, the HPMC powder was added into the water. At $70\,^{\circ}$C HPMC is insoluble in water and in this way the powder could be properly dispersed without forming lumps. After $5\,$min the heating was turned off and the mixture was covered with some aluminium foil to prevent water evaporation. As the mixture cooled the HPMC dissolved, and the stirring stopped because of the large viscosity increase. Before the binder was used for ink making, it was kept undisturbed until air bubbles had disappeared.

[4] Making the solute concentration $0.58\,\mathrm{g\,L^{-1}}$.

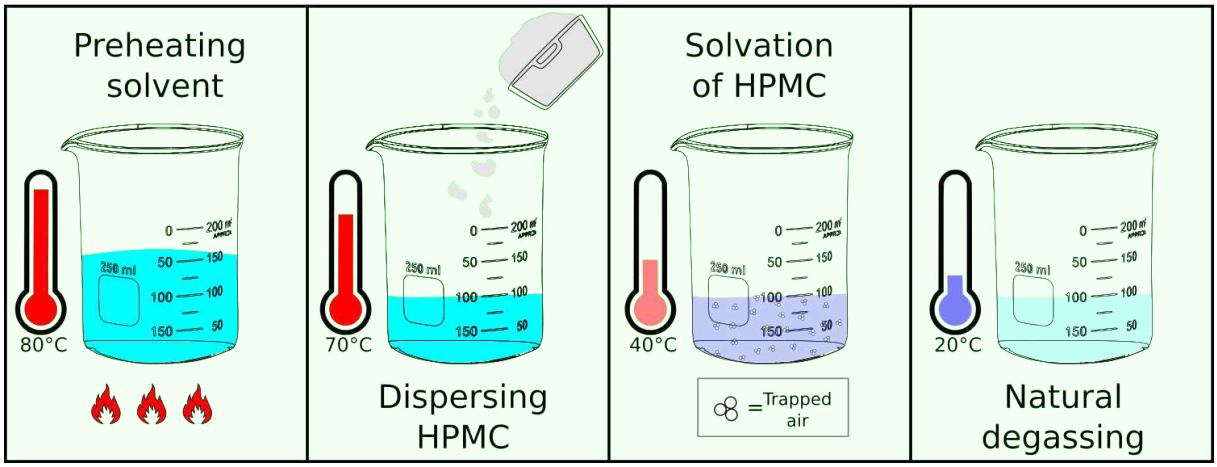

Figure 2.3: Preparation route of the HPMC binder from left to right. First, the solvent is preheated to above the gelation temperature of HPMC. Next, the required volume is mixed with HPMC under medium stirring, HPMC doesn't dissolve at these elevated temperatures. Then, under continued stirring the mixture is allowed to cool down, HPMC starts to solvate. Finally, the mixture is left to stand in order to remove larger gas bubbles.

To make the ink, 21.4 g of spherical Ti6Al4V powder (91-5497, AP&C/General Electric, Boston, Massachusetts, United States) and 4.5 g of binder[5] were added to a beaker. With a mixing spatula this was combined into a thick paste without lumps. After mixing it was transferred into 10 mL cartridge which was then sealed with a piston. Before printing this ink was directly extruded into another 10 mL cartridge, this was done to homogenize the ink and get rid of large air bubbles. After this cartridge was sealed with a piston and fitted with a nozzle it was ready for printing.

[5]Consisting of 4.25 g of water and 0.25 g of dry binder.

2.3.1. Ti6Al4V and akermanite ink

Akermanite is a naturally occurring mineral that promotes osteo-induction [9] similar to hydroxyapatite. Unlike hydroxyapatite [10] though, there is no indication that akermanite decomposes below it's melting point. The chemical formula of akermanite is $Ca_2MgSi_2O_7$, and this isn't substantially different from hydroxyapatite which also contains phosphate and hydroxide groups. The orthosillicate group (Si_2O_7) and magnesium on the other hand are exclusive to akermanite.

Akermanite ink was prepared by mixing four components, namely, spherical Ti6Al4V powder[6], akermanite powder, binder and additional water. The akermanite powder (Material Technology Innovations Co. Ltd., China) had a particle size >63 µm, and irregular morphology. In order to get the 90:10w% ratio 27 g of Ti6Al4V was mixed with 3 g of akermanite, along with 6 g of binder, and 1.2 g of water. This extra water was necessary to make the ink less dry/viscous. All four components were added to a beaker and mixed by hand. After mixing they were transferred to a syringe barrel. Just as before it was homogenized by extruding into another syringe barrel before printing.

2.3.2. Rheology testing

Rheology of the binder and suspensions was characterized using a MCR302 rheometer (Anton Paar GmbH, Germany). All tests were performed in the rotational mode at a temperature of $25\,^{\circ}$C. Material was placed under the rotor disk and any excess was removed from the sides of the disk before the testing. The results can be seen in Figure 2.4. All mixtures had declining shear stress with increased shear rate, a property known as shear-thinning.

Additions of powder to the binder greatly increases the (dynamic) viscosity. Because powder volume makes up over half the total ink volume, powders grinding against each have a major effect on viscosity. Another noticeable result is that the binder alone at low shear rate has a dynamic viscosity of approximately 200 Pa s, at 5.5 wt%. The manufacturer (Sigma Aldrich) specifies a viscosity of 2600 mPa s to 5600 mPa s at $20\,^{\circ}$C and 2wt%. A 2.75 times increase in binder weight fraction thus results in a 35-75 times increase in viscosity

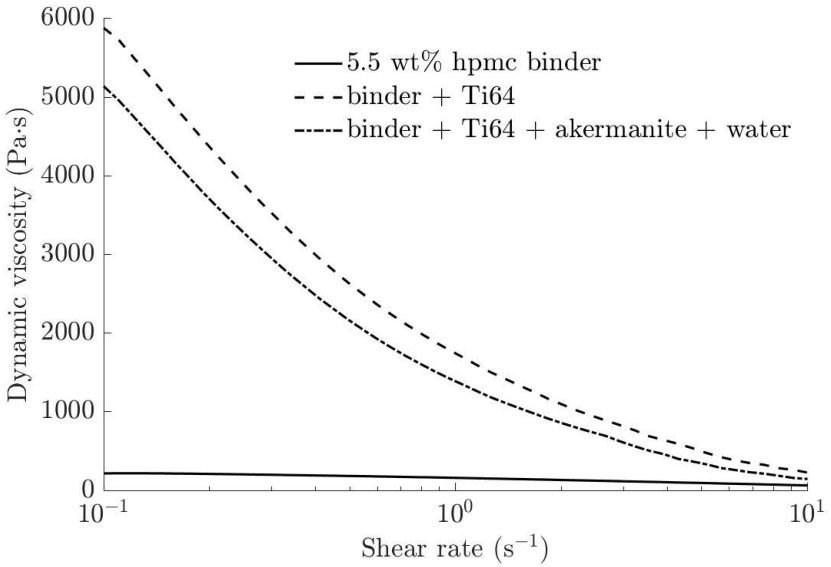

Figure 2.4: Ink and binder dynamic viscosity as a function of shear rate. All mixtures displayed shear-thinning behavior.

[6]The same powder that was used for all other ink.

2.4. Fabrication

This section discusses everything related to the fabrication of the scaffolds about the printing process to the post processing needed, via sintering.

2.4.1. Gesim Bioscaffolder

For the fabrication of all scaffolds a Gesim Bioscaffolder 3.2 (GeSiM Bio-instruments, Germany) (bio-)printer was used. Extrusion is driven by gas pressure. It has up to 3 independent extruders, one of which can be heated, and has advanced features such as tip calibrations, Z-height offset calibration and automated tip cleaning[7]. Printing material is stored in single-use 10 mL Nordson EFD (Nordson Corporation, Westlake, Ohio, United States) syringe barrels that come with an optional piston and have a luer lock connector. The pressure driven system and single-use barrels eliminate the possibility of cross contamination of different printing materials.

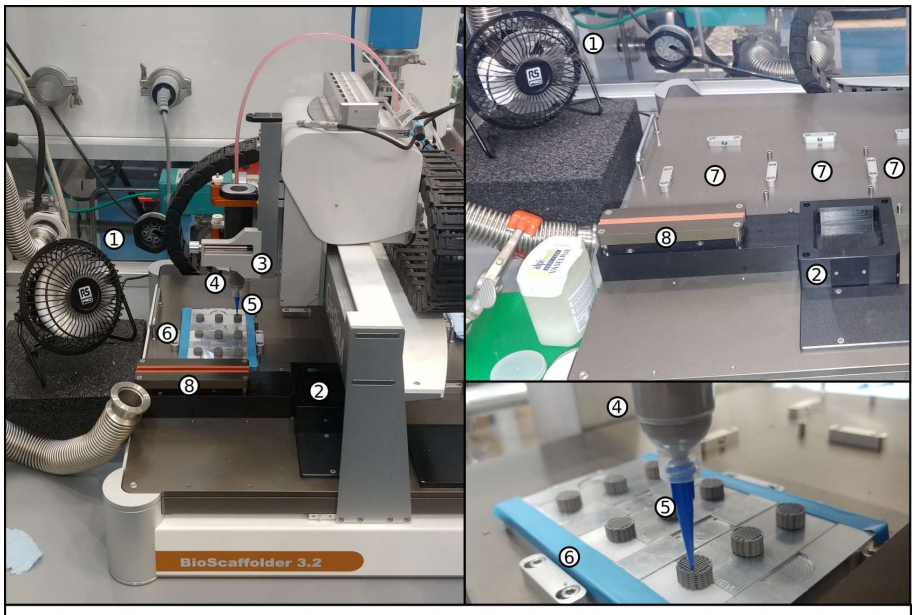

1. Blower fan 2. Tip calibration tool 3. Z-height sensor 4. Syringe barrel
5. Conical nozzle 6. Build surface (glass) 7. Wellplate slots 8. Tip cleaner

Figure 2.5: The 3D printer and peripherals with legend.

[7] It wasn't operational on the machine used in this study.

The Gesim Robotics software that comes with the Bioscaffolder can perform gcode generation, suitable for printing (very) basic scaffold geometries. It also comes with it's own slicer for processing stereolithography (STL) files[8]. However, it's features are limited, and some that would be particularly useful were missing. In order to print successfully, sufficient ink drying is critical. For this reason, printing has to happen layer by layer rather than sequentially. This allows each layer printed to dry during the printing of other scaffolds on the buildplate. Drying time was in fact the speed bottleneck, rather than machine kinematics. The required behaviour could only be achieved with long sequences[9].

2.4.2. Printing of the scaffolds

Printing of the scaffolds using the Gesim Bioscaffolder printer began with the preparation of a sequence file. First, the gcode file for every layer was created with the built in tool[10]. For the 400 µm spacing scaffolds, 2 gcode files each were needed, one for a $0°$, and another for a perpendicular $90°$ geometry. The core shell scaffolds required 4 gcode files.

Some additional parameters had to be entered into the tool for the gcode to be generated in particular print speed ($3.5\,\mathrm{mm\,s^{-1}}$), extrusion pressure (200 kPa to 250 kPa), start break (1 s), tear-off distance (5 mm) and tear-off speed ($5\,\mathrm{mm\,s^{-1}}$). Then, a sequence for 9 scaffolds had to be made resulting in sequences of 288 steps. After 9 steps (1 layer) the next 9 steps were offset 328 µm so that it'd be printed 328 µm higher than the previous layer. Finally, the machine itself needed to be configured by uploading a configuration file, running initialization (homing sequence) and performing Z-offset calibration on the printing surface.

Before printing a new batch of ink was prepared, the binder was always prepared beforehand, and was never more than 3 weeks old. The use of fresh binder can be quite important, as it can degrade and change properties over time through dehydration and formation of mold. Because the binder is water soluble and the solvent is water no heating was required during printing[11]. The ink syringe barrel was fitted with a 410 µm conical nozzle, fitted with a pressure connection, positioned in the holder and connected to the pressure line. Tool calibration was performed using the 'TipCalibratorGen2' module using the 'SlowApproach' mode selected from the 'Manual' tab in Gesim Robotics. After this, a small amount of ink was purged to fill the conical tip after which it was manually wiped with a paper towel. After that, the sequence created earlier was ran. During printing a small USB powered blower fan provided airflow over the build plate to aid drying, it wasn't used during multimaterial printing as it led to tip clogging.

[8] The Gesim Robotics software on the accompanying computer hadn't been updated since 2019, the STL slicer function wasn't actually implemented in this version

[9] The 32 layer scaffolds required a 288 step sequence, each step corresponding to the execution of a gcode file.

[10] Located under the 'Scaffold' tab in Gesim Robotics

[11] Heating would be detrimental as the binder gelates when heated.

2.4.3. Sintering of scaffolds

Prior to debinding and sintering the scaffolds possessed little strength. To remove the binder, and sinter the particles a STF16/180 tube furnace (Carbolite Gero Ltd., UK) was used. Across two alumina crucibles 8 or 9 samples were placed. Each crucible contained 4 samples and a sacrificial material on either side, the crucibles were, additionally, covered with a titanium plate. Prior to any heating the tube furnace was flushed for $2\,\mathrm{h}$ with pure argon >99.9% at a high flow rate. After two hours, debinding was performed by heating to $350\,^{\circ}\mathrm{C}$ at a rate of $2\,^{\circ}\mathrm{C\,min^{-1}}$ and held at $350\,^{\circ}\mathrm{C}$ for $1\,\mathrm{h}$. During debinding a large mass fraction of the methylcellulose is broken down, but some of the the carbon backbone remains. Thermogravimetic analysis done by others on methylcellulose showed that up to 90% of starting mass is lost [23]. After the debinding had finished, the temperature was increased to $1200\,^{\circ}\mathrm{C}$ at a rate of $10\,^{\circ}\mathrm{C\,min^{-1}}$ where it was held for $6\,\mathrm{h}$.

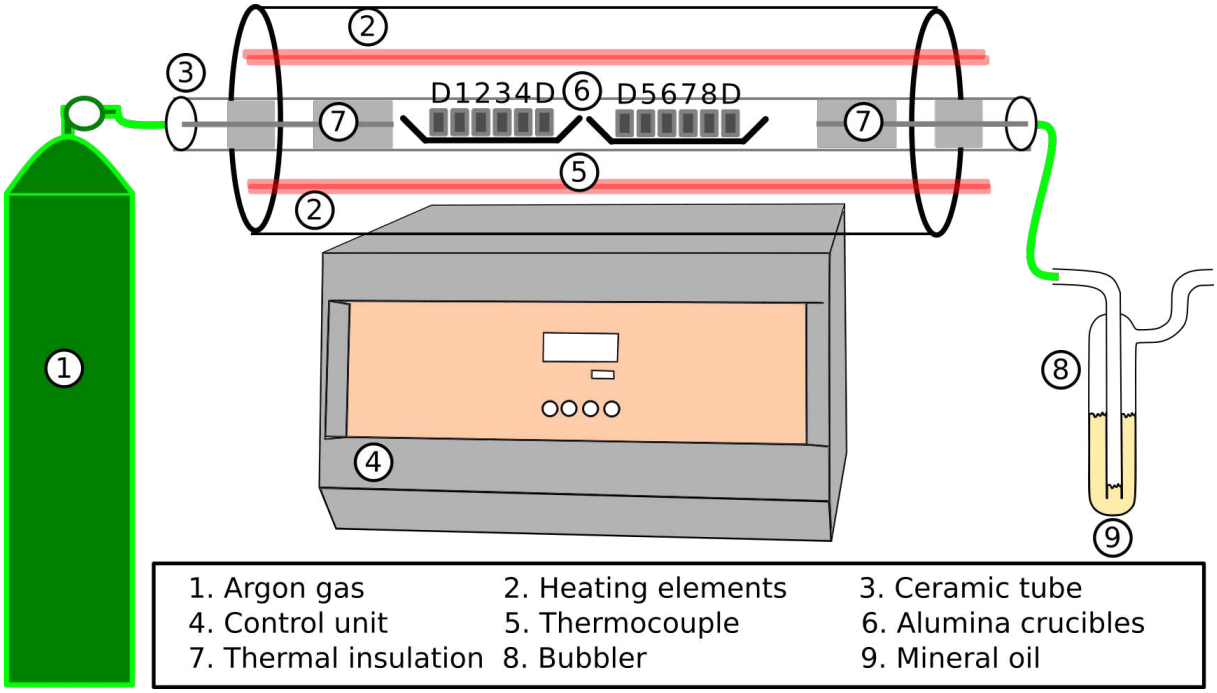

Figure 2.6: Tube furnace inert atmosphere sintering setup

The furnace was a basic model and did not support temperature profiles, therefore cooldown was uncontrolled and the cooling rate exceeded $20\,^{\circ}\mathrm{C\,min^{-1}}$. After the furnace had cooled down the samples were removed and stored in sample boxes until further characterization.

Evaluating partial sintering

One set of Ti samples was sintered for a reduced amount of time. The justification for the relatively short holding time of $2\,\mathrm{h}$ is to stimulate only partial sintering [24] and increase the porosity.

2.5. SEM imaging and EDS

Surface microstructure, strut spacing, and width were characterized using a scanning electron microscope (SEM). The atomic makeup of the material was measured qualitatively and quantitatively using energy-dispersive spectroscopy (EDS). Before analysis could take place the samples had to be made conductive to avoid charging effects. First conductive double sided stickers were placed on an imaging stage. Then samples were placed on the stickers. Using a compressed air gun the samples were lightly brushed with clean air to remove loose particles and contaminants. Next the samples were covered in a thin layer of gold using a sputtering process. The coating machine (Auto Fine Coater, JEOL JFC-1300, Japan) was loaded with the sample, the chamber was put under vacuum to a pressure below 0.1 mbar and the sample was sputtered for 90 s. After the samples were coated they were placed in the SEM (JSM-IT100LA, JEOL, Tokyo, Japan). For the EDS analysis the stage was positioned such that the working distance was at 10 mm, when the microscope was in focus. The beam current from the thermionic emission was set to 60 nA. Acceleration voltage was set to 15 kV, giving the electrons 15 keV of energy, which is enough energy for most elements to be detectable with EDS. The exceptions being very low (below Beryllium) and very high (above Uranium) atomic number elements. For our analysis these conditions were sufficient.

The SEM was used to capture images unsintered and sintered samples of all tested scaffolds at a various magnification levels. For the mutlimaterial scaffolds the interface where these materials connect was also imaged.

2.6. μ-CT

Using a μ-CT scanner (Xradia Context MicroCT, ZEISS) the internal structure for one TiAk sample was obtained. The voxel size of the scan was approximately 6 x 6 x 6 µm, which is smaller than most ceramic and metal particles in the starting materials. The primary objective was to identify internal defects from the manufacturing and or sintering process. Many of these defects can be difficult to spot even when cutting, polishing and using the SEM. Using CT the defects can be observed without destroying the sample.

2.7. X-ray diffraction spectrometry

X-ray diffraction (XRD) spectrometry was performed on sintered samples to find the phase composition. A Bragg-Brentano geometry D8 Advance X-ray diffractometer (Bruker,Billerica, Massachusetts,United States) was used for the characterization. The copper X-ray source produced Cu Kα radiation, the acceleration voltage was 45 kV and the tube current 45 mA. The scan angle was between $5°$ and $110°$ in $0.04°$ increments. The integration time at each position was 2 s. The measurement data was evaluated using Bruker DiffracSuite.EVA version 6.1. (Bruker,Billerica, Massachusetts,United States).

2.8. Porosity of the scaffolds

Porosity measurements were performed according to the ASTM B963-14 standard [25][12]. All samples were weighed after sintering before oil impregnation. The standard's preferred method was used in which scaffolds are submerged in oil, and then put under a weak vaccuum of 7 kPa for 30 min, followed by a period of 30 min at atomspheric pressure. Sunflower oil (Jumbo, the Netherlands) was used as impregnant and had a density of $0.919\,\mathrm{g\,cm^{-3}}$. After impregnation with oil the samples sequentially removed from the oil, wiped to remove superficial excesses of oil, and then weighed in both air and pure ethanol (density of $0.789\,\mathrm{g\,cm^{-3}}$). The surface connected porosity of the samples can then be calculated using Equation 2.3. These measurements yield 3 values from which the porosity can be determined. The first measurement gives the dry weight in air. If the average density of the scaffold material was known the filled volume could already be calculated to find the porosity. However, this is assumed to be unknown. The second value is the weight when saturated with oil. From these two values it's possible to calculate the weight of the oil (Equation 2.1) in the pores, and since the density of the oil is known also the pore volume. With V_{pores} the pore volume in $\mathrm{cm^3}$, ρ_{oil} the oil density in $\mathrm{g\,cm^{-3}}$ and m_{oil}, m_{sat} and m_{air} the mass of the oil, the saturated scaffold and unsaturated scaffold in g, respectively.

$$V_{pores} = m_{oil}\frac{1}{\rho_{oil}} = (m_{sat} - m_{air})\frac{1}{\rho_{oil}} \tag{2.1}$$

[12] Newer versions of the standard such as ASTM B963-17 and ASTM B963-22 don't change the method.

The final measurement where the scaffold is submerged in pure ethanol gives the scaffold density. By submerging the oil filled scaffold in ethanol the recorded weight is reduced by the Archimedes forces which themselves are a result of gravity. The reduction in weight is proportional to the submerged (open) volume and the density of the ethanol via Equation 2.2. In which V_{sub} is the total submerged volume, ρ_{EtOH} is the density of ethanol The submerged volume and m_{sub} the mass[13] of the oil saturated scaffold submerged in ethanol.

$$m_{sat} - m_{sub} = V_{sub}\rho_{EtOH} \tag{2.2}$$

Combining Equation 2.1 and 2.2 the porosity can be calculated via Equation 2.3 which is equivalent to the equation in the ASTM B963-14 standard[14].

$$\%_{por} = 100 \cdot (\frac{V_{pores}}{V_{sub}}) = 100 \cdot \rho_{EtOH} \frac{m_{sat} - m_{air}}{\rho_{oil}(m_{sat} - m_{sub})} \tag{2.3}$$

[13] A critical reader might consider this statement erroneous, the mass isn't changing by submerging. The weight is changing but weight is a reaction force not a mass. The correct but cumbersome definition would be the mass as measured by a scale calibrated in air.

[14] Except the liquid used for submersing the samples in the ASTM B963-14 standard is water instead of ethanol.

2.9. Mechanical testing of the scaffolds

Mechanical testing was performed on a Z100 universal testing machine (Zwick/Roell, Ulm, Germany) for this a 100 kN load cell was used. Tests were in accordance with ISO standard 13314:2011 [26] which describes compression testing for porous metal structures.

Two flat steel plateaus were attached to the machine, secured with a pin and locked with a round nut. In the testXpert III control software parameters, such as the total displacement, preload, displacement rate and maximum force were entered. The preload was set at 10 N, the displacement rate at 0.05 mm s^{-1}, and the total displacement to 5 mm which corresponds to a strain of approximately -50 to -55%. Samples were positioned between the two plateaus in the center and compressed. After every test the largest piece was recovered, scaffold debris was cleaned from the plates before the next test.

$$E = \frac{\sigma}{\epsilon} \tag{2.4}$$

Testing data was processed in the following way: The elastic modulus was extracted from the elastic region where the slope was constant. This was done manually. Equation 2.4, in which σ is the stress and ϵ is the strain, was used to calculate the elastic modulus E from the slope. To calculate the stress at yield each line was offset +0.2% strain and the intercept with the stress-strain curve acquired.

2.10. Statistical analysis

statistical analysis was performed on the results of the mechanical tests. First a one-way ANOVA was performed to see if there was a difference between groups. Followed by a Bonferroni post hoc test in order to find between which groups the differences were significant.

2.11. Conclusions of materials and methods

In this chapter all the steps from the production to the ink to printing to characterization were given in detail.

While performing the printing and sintering some minor inconveniences were discovered and thus some recommendations can be made. It was found that the cartridges were not perfectly cylindrical but slightly tapered resulting in increased drag on the piston as printing progresses. It is hypothesized that this (elaborated in appendix D) reduces flowrate while printing is going on. As such filling the cartridge all the way to the top may make the flowrate less dependent on cartridge fill level. The gripes with flowrate control didn't end there, inconsistency between batches and pressure fluctuation around the setpoint were frequent occurrences. The former is caused by the strong non linear relation between viscosity and HPMC concentration in the binder. At the high binder concentration of 5.5w% HPMC any evaporation of water during ink mixing can make a noticeable difference. And the later is a result of the pressure control mechanism of the printer.

One recommendation could be to produce the ink for all samples as a single batch to minimize the spread, but instead moving to a method of volumetric extrusion may be more fruitful. Such a move would decouple the flowrate from the viscosity. A major part of the recommendations presented in the discussion is centered around this idea.

Lastly, on one occasion the steel plate used to cover the crucibles during sintering ended up touching some of the samples. An alloy between the steel and Ti6Al4V was formed which had a lower melting point than either pure alloy. A total of three samples were destroyed of which one dummy and two good samples. Replacing this crucible cover with a titanium plate will not only prevent this catastrophic melting, but also protect the samples as titanium is more susceptive to contaminants[15] than steel.

[15] Titanium reacts with many compounds to form nitrides, oxides and carbides, it's a difficult metal to sinter.

3

Results

3.1. Characteristics of sintered scaffolds

The printing process produced a green state body which, at least at first glance, closely resembles the design. Details such as the layer pattern and layer height are all there. The first discrepancy is the flat bottom layer, this is where the ink met the glass during printing, and it's a bit squished. This squishing is intentional and required to secure it to the print surface. Some actual defects may present themselves on the surface, defects such as: broken strands, air pockets, sagging and coalescence. But, the majority of the defects remain obscured from view, below the surface or deep inside the scaffold. Section 3.4 touches upon these internal defects using µ-CT imagery.

After sintering the scaffolds, which can be seen in Figure 3.2, came out of the oven still resembling the design. In Figure 3.2e the differences in shrinkage between the Ti half and the TiAk half stand out, Ti shrinking more than the TiAk composite. The CS designs may appear unaffected by the difference in shrinkage but in 3.2g the Ti core is slightly recesed. In a CS with a TiAk core and Ti shell (not shown) it is reversed, with the core slightly bulging above the shell.

In Figure 3.1 the top surface of the Ti and TiAk scaffolds can be seen. The struts follow the design to a T, except for some minor air pockets. In Figure 3.1b the akermanite particles (white) are clearly visible and appear evenly distributed.

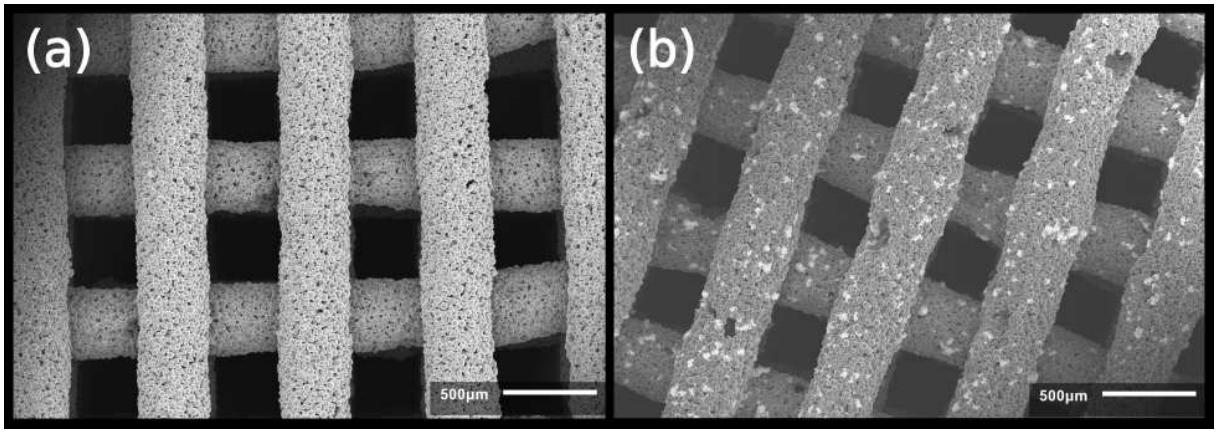

Figure 3.1: Strut morphology of (a) Ti and (b) TiAk scaffold.

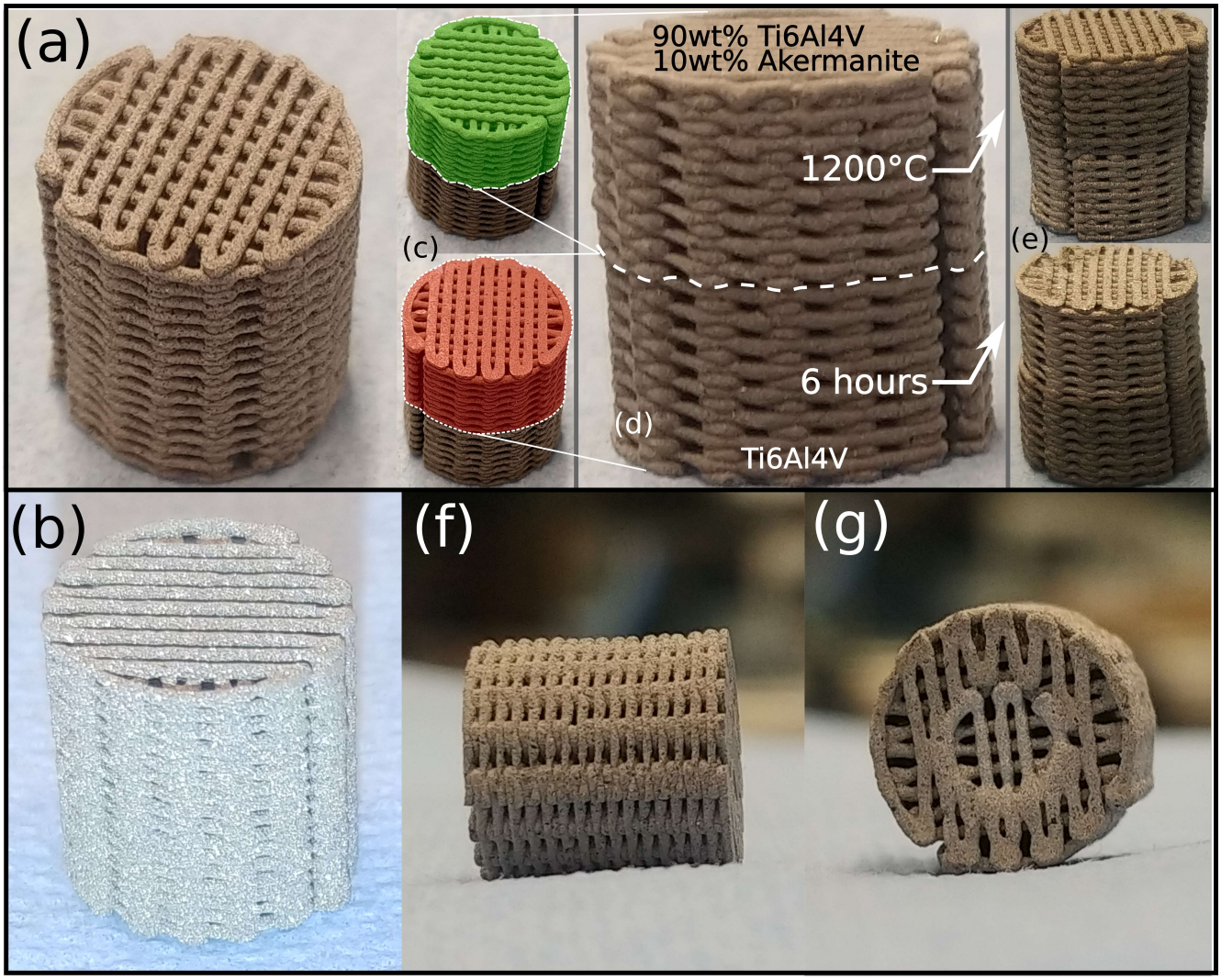

Figure 3.2: The different scaffold types: (a) full Ti (2 hours at $1200\,^{\circ}$C), (b) Full TiAk scaffold (6 hours at $1200\,^{\circ}$C), this image was intentionally overexposed to reveal akermanite particles. (c) Unsintered HH scaffold with the top (in green) made from Ti and the bottom (in red) made from TiAk. (d) Sideview of the HH scaffold (e) Sintered HH scaffold (f) CS sideview and (g) CS frontview with Ti core and TiAk shell.

3.2. EDS results

EDS is a mostly qualitative analysis method, and not particularly suited for quantitative analysis. Additionally, the penetration depth of EDS limits it to superficial analysis which may or may not be a bad thing depending on the volume of interest. A longer integration makes EDS analysis a little less eratic as peaks can be more clearly distinguised as well as the ratio of different elements. Integration time was 10 min for all EDS measurements.

3.2.1. Ti6Al4V and akermanite scaffolds

Akermanite is a ceramic which remains stable during sintering even at temperatures of up to $1250\,^{\circ}$C [11]. The sintered samples had visually distinct regions on the SEM images and the EDS analysis in Figure 3.3 shows that these regions contain phases of titanium alloy and calcium silicate ceramic. EDS results of the particle assumed to be akermanite (Number two in the figure) also show some titanium and no magnesium. The absence of any magnesium may be due to it being a relatively light element and it being less than 9 % in akermanite. Since the EDS has some interaction volume some titanium may be present and giving these returns.

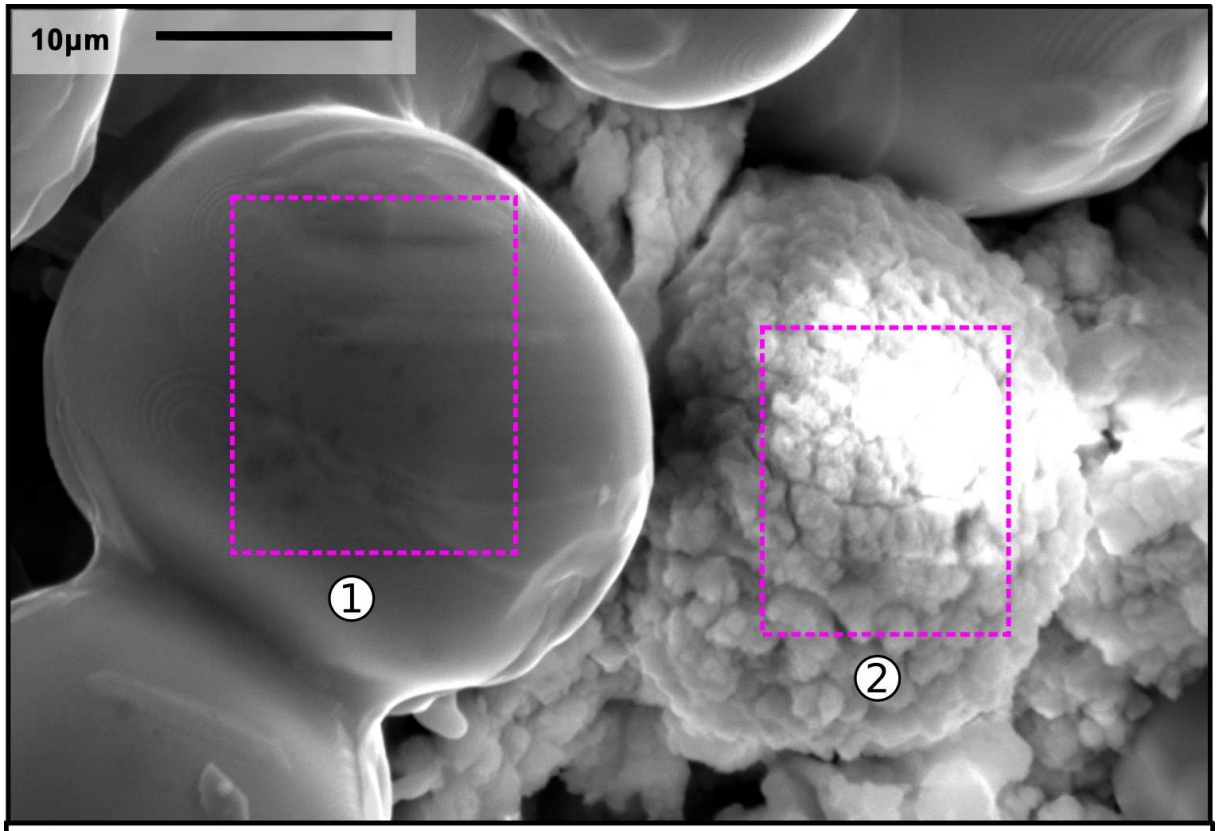

#	C	O	Al	Ca	Ti	Si	V
1	-	1.66	5.58	0.17	86.11	0.61	5.79
2	6.67	49.76	0.38	29.95	11.69	1.55	-

Figure 3.3: EDS results of Ti6Al4V + Akermanite composite scaffold

3.2.2. EDS Mapping of Core Shell Scaffold

EDS mapping was used to identify the spread of calcium and silicon through the scaffold. Figure 3.4 shows that calcium remained confined to the area of the akermanite particle and silicon only diffused slightly.

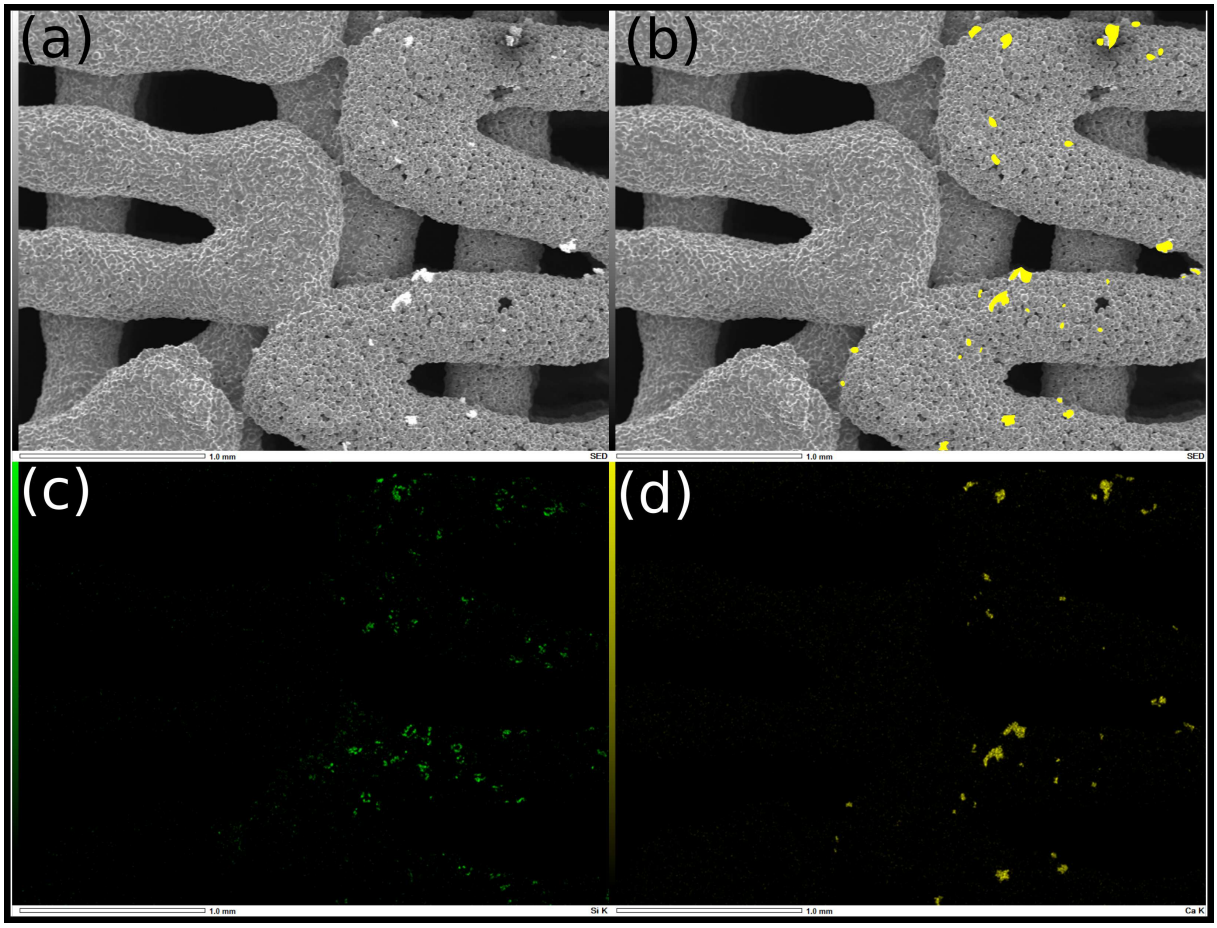

Figure 3.4: EDS map of CS Ti TiAk scaffold at minimal magnification: The ordinary SEM image (a) shows the Ti core and the TiAk shell. In (b) the calcium mapping result from (d) is overlaid, which lines up exactly. Mapping for the silicon (d) did not line up with the particles but was confined to the TiAk shell of this scaffold.

3.3. Partial Sintering, Porosity and Strut width

The holding time during sintering of Ti scaffolds was kept short at two hours at $1200\,^{\circ}$C) for one set, and six hours at $1200\,^{\circ}$C) for another. This leads to only partial sintering in the two hour set. This decreases stiffness and strength. SEM images (Figure 3.5) illustrate the large differences in the formation in of sintering necks. In the six hours set particles are joined together, while in the two hour set merging barely started.

This technique can be used as a global modifier, if a scaffold is too stiff reduce the sintering time and every part of the scaffold will come out sintered less. Essentially it allows one to drop the stiffness at the expense of strength.

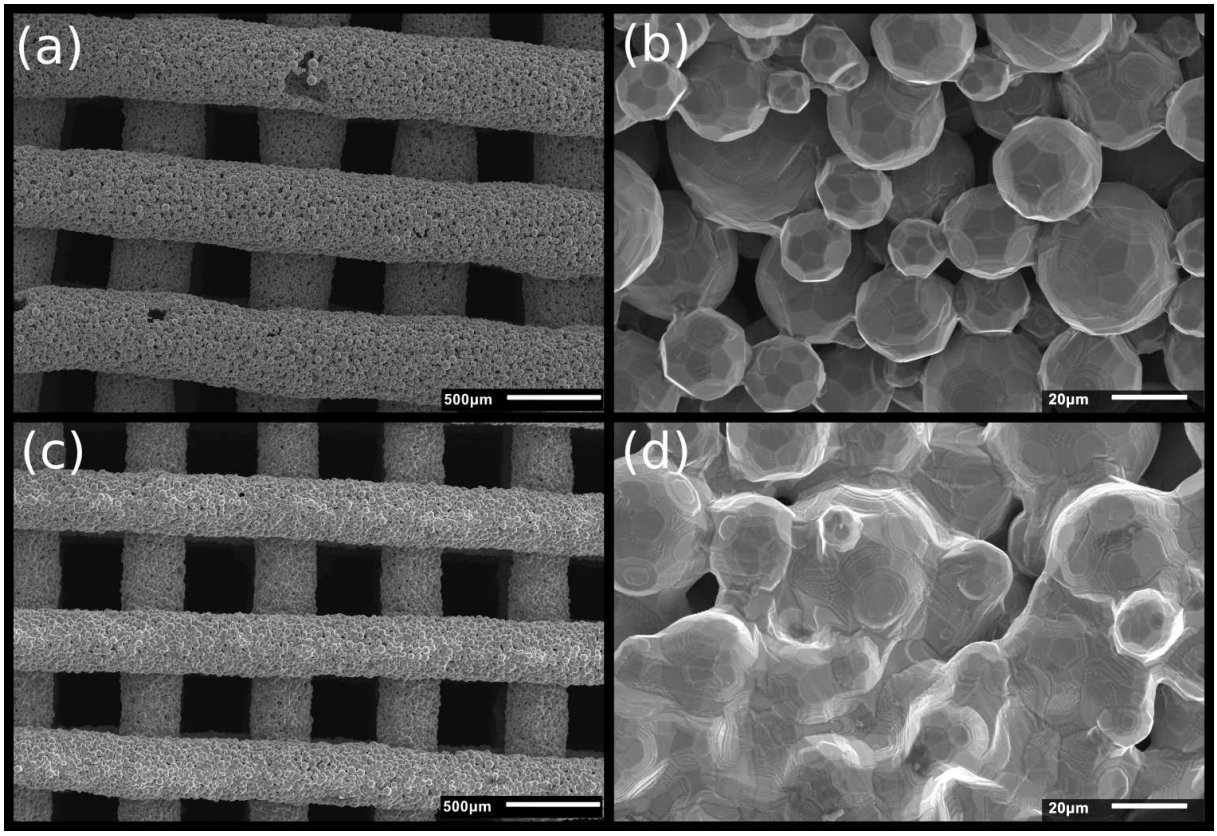

Figure 3.5: The effect of sintering on Ti6Al4V scaffolds: (a) The struts of a scaffold sintered for two hours and (b) the neck formation on the particles. (c) The struts of scaffold sintered for six hours and (d) the particles close up.

Table 3.1: Strut width and porosity of scaffolds after sintering compared to the design specification

Sample group	Strut width (µm)	Connected porosity (-)	Design porosity (-)
Ti (sintered 2 hours)	460 ± 10	70 ± 2	58
Ti (sintered 6 hours)	336 ± 4	65 ± 2	58
TiAk	386 ± 24	67 ± 2	58
CS Ti TiAk		42 ± 1	60
Core	455 ± 7		
Shell	442 ± 14		
CS TiAk Ti		43 ± 6	60
Core	520 ± 22		
Shell	407 ± 18		

3.4. Defects and μ-CT

Previously various defects were mentioned such as: broken strands, air pockets, sagging and coalescence. Defects like these can be attributed to at least two sources: First the quality of the ink (inhomogeneity in the broadest sense and formulation) and second errors in the flowrate (tracking of the ideal flowrate).

In some cases these defects are visible on the surface, and the most common externally visible defect is air pockets. These air pockets are introduced into the ink when the binder is mixed with the powder, and as such are distributed throughout the scaffold.

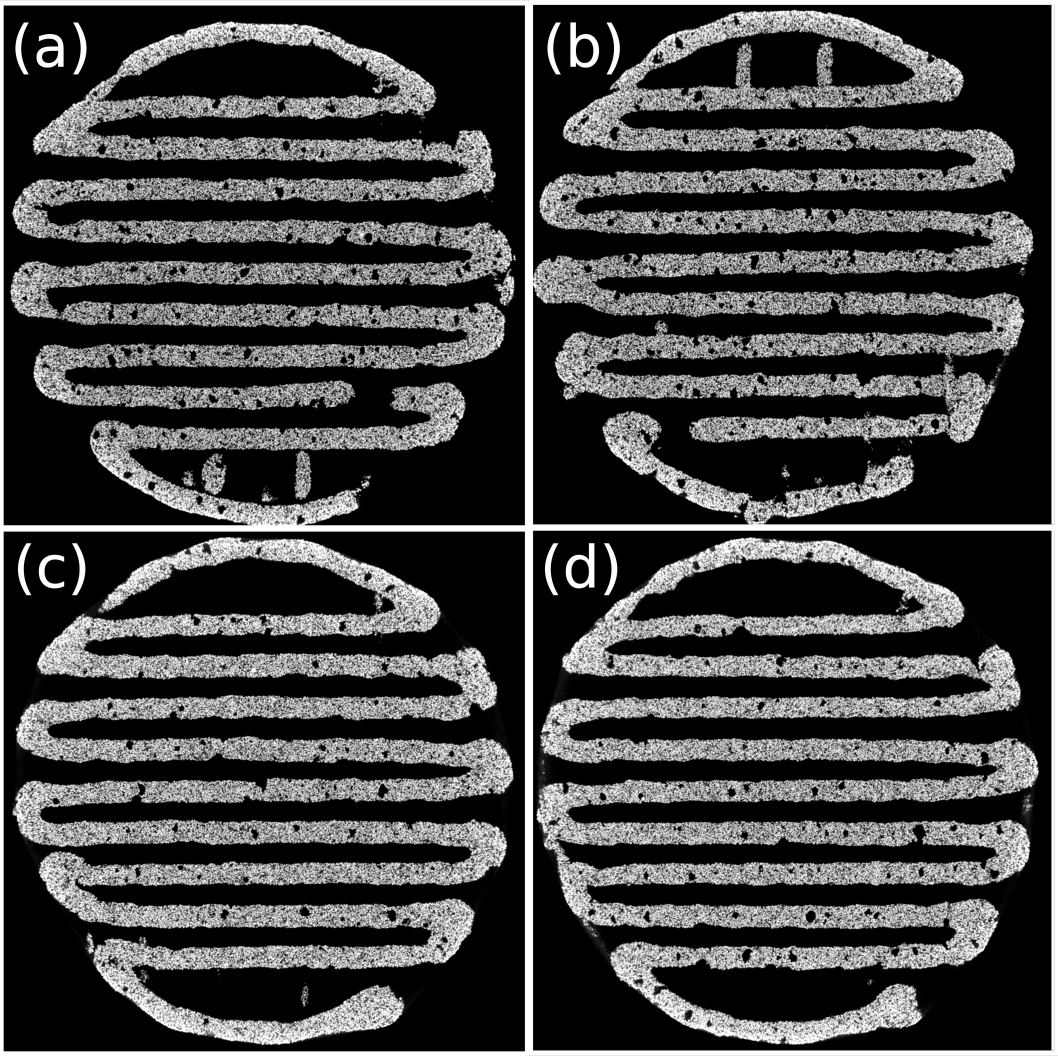

Figure 3.6: Four CT slices taken in the printing plane of individual layers after skew correction in Dragonfly: (a) and (b) show broken strands near the bottom right and bottom left corners. Layers (c) and (d) have no broken strands. Every layer has distributed air pockets, which are larger than the porosity that is present between particles.

Broken strands are another manufacturing issue, and one that can have a number of causes. Under-extrusion can cause it, even when the ink is otherwise perfect. If too little material is extruded the material will have to stretch, something it can do only do so much. Another cause for under-extrusion is when a large bubble of air makes it to the nozzle leading to a temporary halt in extrusion, while not technically a strand break the result is very similar.

Coalescing or the joining of two (strands) has also been observed. The statement that over-extrusion causes coalescence is trivial. What is not trivial is that under-extrusion can cause it as well. Similar to the broken strands mentioned earlier, lack of material can also cause a lack of attachment to any previous layers or the build platform. When a segment of ink isn't attached to anything it can be dragged into itself to form coalesced strands.

Sagging is another source of error and happens when ink is suspended without support. Like a beam, sagging gets worse the further away the ink is from any support. Sagging is not exclusive to overhangs, sagging can also occur when layers are insufficiently dried and unable to bear the load placed on top of them. Some sagging can be seen in Figure 3.6a at the bottom and 3.6b at the top. In these two images there is no sagging in places where the struts are only $400\,\mu$m apart, but at the start and endpoints the arc follows the cylinder shape causing a long overhanging segment in the layer printed on top. These

segments on top can sag.

The side view of the scaffold that can be seen in Figure 3.7, however, is not an example of sagging. Sagging appears as a beam that is curved downwards, but the top of the strut isn't curved downwards. The extra material that is reducing the pore height thus must come from over-extrusion. As the nozzle moves over an open area the downstream conditions (back pressure) change, and the flowrate increases. Figure 3.7 is rather the result of over-extrusion, the two white lines illustrate the layer shape according to the design, while the red and green arrows indicate over-extrusion and absence of sagging, respectively.

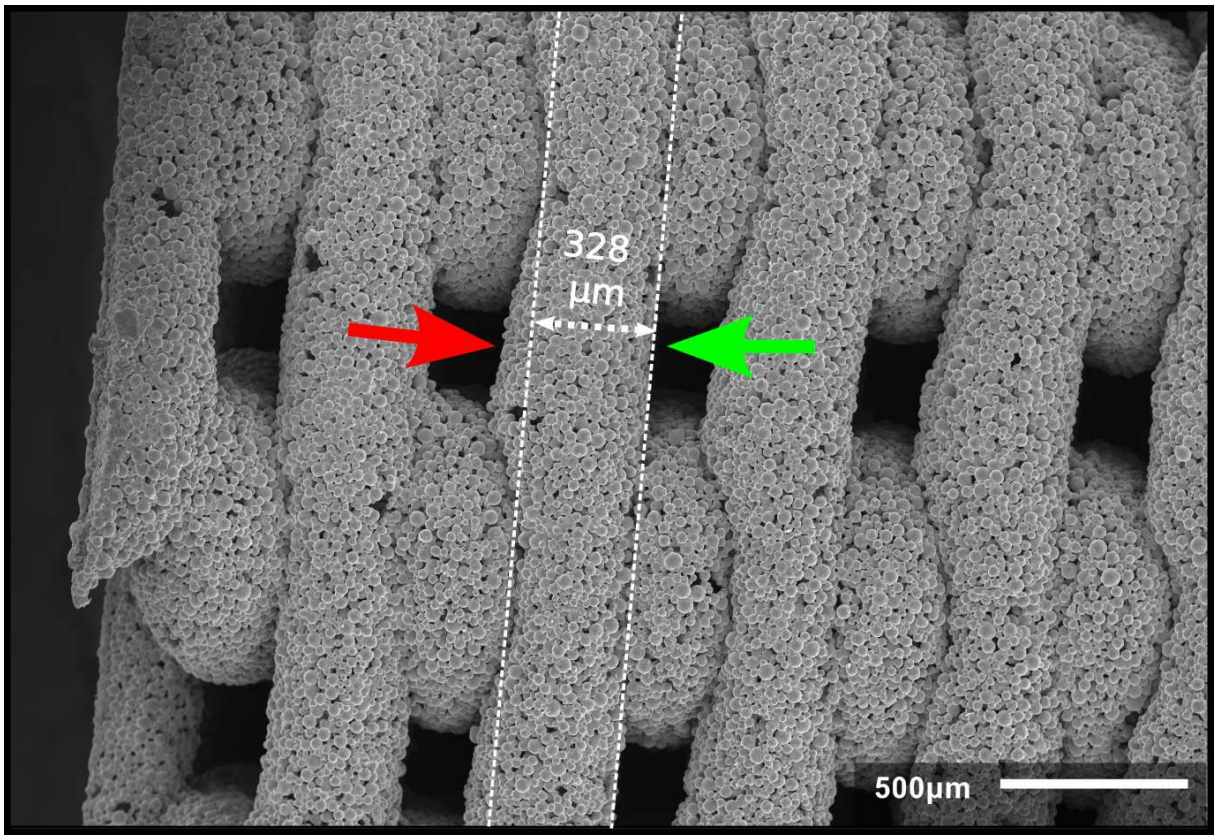

Figure 3.7: Side view of a scaffold with over-extrusion (at the green arrow) but without sagging (at the red arrow). The dotted white lines indicates the design height ($328\,\mu$m) and the shape of the strut (straight).

3.5. XRD results

XRD results (Figure 3.8) for scaffolds prepared with only Ti6Al4V have two phases present. With the first phase being Ti6Al4V. One other phase is present in the form of 60% titanium and 40% vanadium, based on the low peaks this is a minor phase. The akermanite starting material consists of akermanite as well as some diopside, which is closely related to akermanite. In the XRD result for sintered Ti6Al4V + akermanite composite, no akermanite could be detected. However, there was, supposedly, portlandite (calcium hydroxide) and titanium silicide. The presence of calcium hydroxide is implausible because it decomposes to calcium oxide and water well below the sintering temperature [27] of $1200\,^{\circ}$C. No compounds containing magnesium were detected, either it was too minor a phase to detect or perhaps there aren't any left.

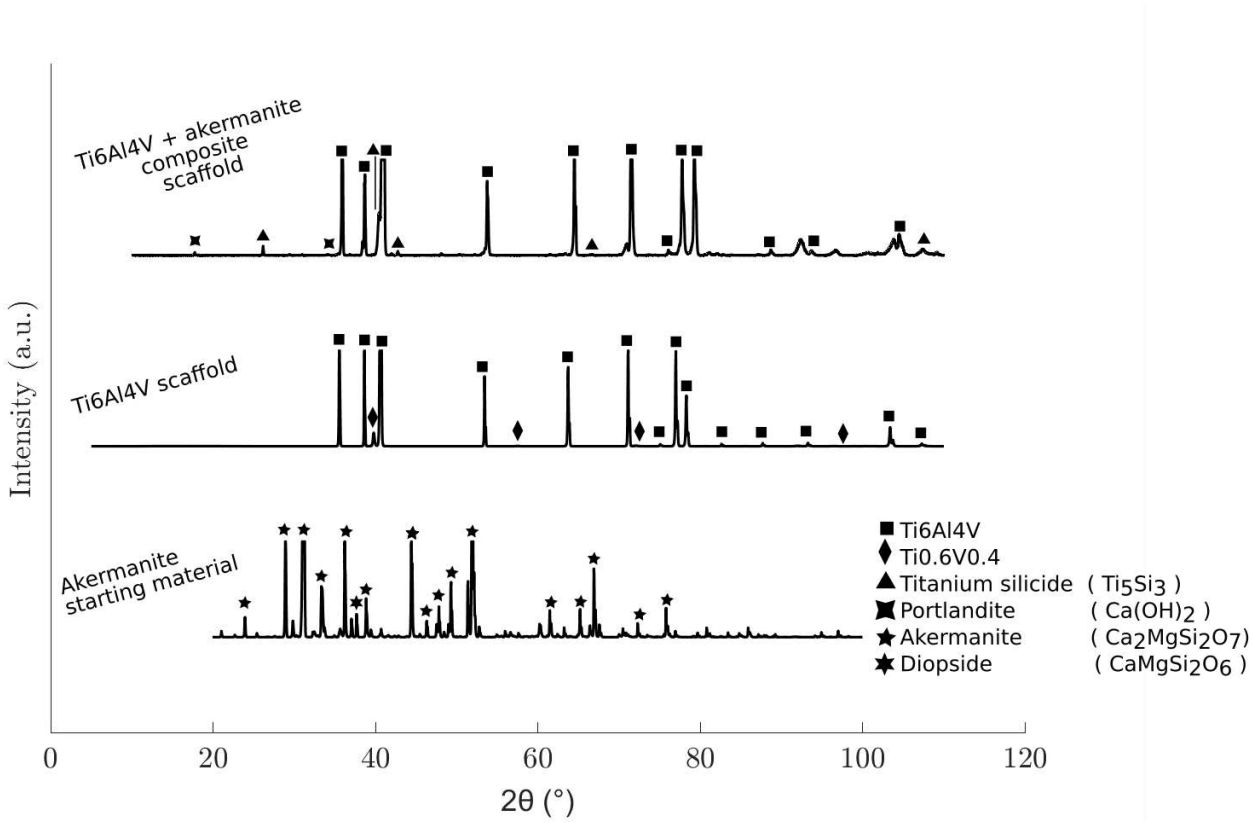

Figure 3.8: XRD spectra of Akermanite powder (starting material), sintered Ti6Al4V scaffold and sintered Ti6Al4V + akermanite composite scaffold

3.6. Mechanical properties

In the mechanical compression tests two types of behaviour were visible, the first is that of a metallic sample which has a linear elastic region followed by strain hardening and compaction. The second is that of a ceramic sample which fractures after absorbing only a small amount of energy. In Figure 3.9a this metalic behaviour and in 3.9c the ceramic behaviour can be seen side by side.

Young's modulus of the five types of scaffolds was 1159 $\pm$ 104 MPa, 858 $\pm$ 61 MPa, 1273 $\pm$ 213 MPa, 2244 $\pm$ 308 MPa, 4250 $\pm$ 371 MPa for Ti, TiAk, HH, CS Ti TiAk and CS TiAk Ti, respectively. And the yield strength, in the same order, was 72.6 $\pm$ 5.2 MPa, 9.2 $\pm$ 2.5 MPa, 13.8 $\pm$ 2.9 MPa, 145 $\pm$ 19 MPa, 260 $\pm$ 11 MPa.

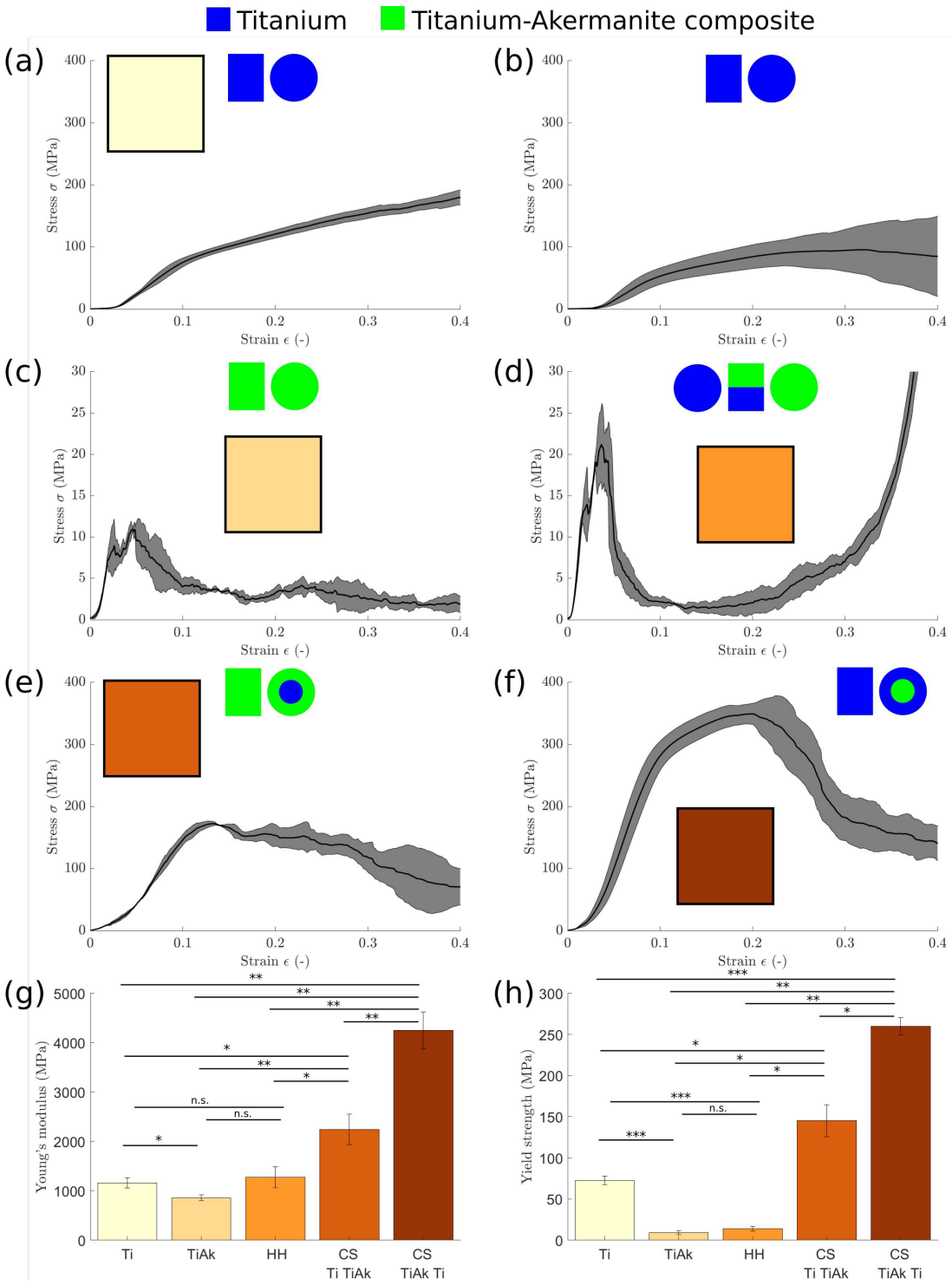

Figure 3.9: Compressive mechanical properties of five scaffold types: Stress strain curves of (a) Ti sintered for six hours at $1200\,^{\circ}$C, (b) Ti sintered for two hours at $1200\,^{\circ}$C, (c) TiAk, (d) HH, (e) CS Ti TiAk and (f) CS TiAk Ti. Data is sumarized in tables: (g) for Young's modulus and (h) for yield strength. ANOVA results were p = $5.57 \cdot 10^{-8}$ and p = $1.91 \cdot 10^{-10}$ for Young's modulus and yield strength, respectively. A total of ten post-hoc tests were done for both, thus the significance level with Bonferroni correction was < 0.005. Meaning only '**' and '***' were truly significant.
n.s. = p $\geq$ 0.05 (not significant), * = p < 0.05, ** = p < 0.005 and *** = p < 0.0005

3.6.1. Half-half scaffold failure mode

The HH scaffolds was made to prove that Ti and the TiAk composite could successfully bond, this they did. Upon testing, however, the TiAk side failed first before the Ti side started yielding. Figure 3.9b shows the HH stress strain curve, Here the ceramic side crumbles and gets compacted, and only then the metallic side starts to deform. This behaviour makes sense as the yield strength of the Ti scaffold is over four times higher than that of TiAk, and thus the side made of TiAk will yield while the small elastic deformation of the Ti side is only temporary.

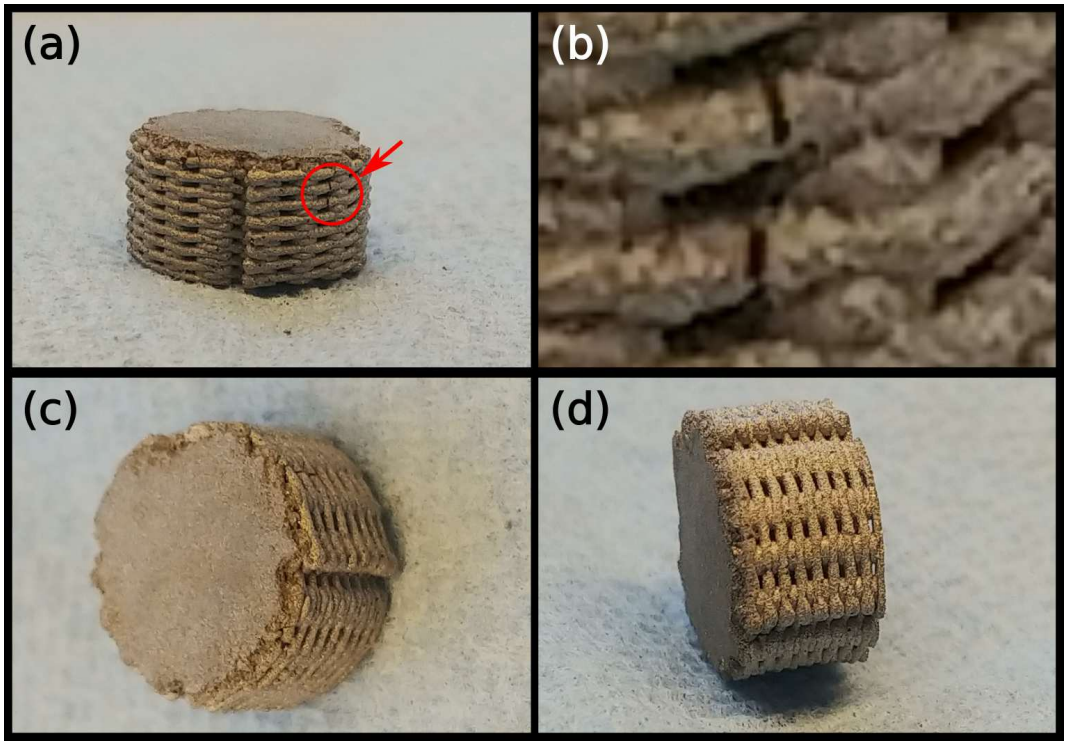

Figure 3.10: HH scaffold remains after compression: (a) Minor crack in two strands on the Ti side. (b) A close-up of the cracks (c) HH remains bottom (TiAk side) (d) sideview of the remains

3.6.2. Core-shell failure mode Core = Ti Shell = TiAk

Failures behaviour of the CS depended on the material. When the core was Ti and the shell was TiAk composite something similar to the HH scaffold happens. Even a minor strain, as low as 5%, cracks the ceramic like composite. As the strain is increased the uncontained failure quickly follows, expelling shards of debris. At 15% to 20% strain the outer shell completely detatches itself from the Ti core. Footage captured during compression tests, of this failure, is shown in Figure 3.11 for all six CS (Ti) (TiAk) samples. Failure of parts of the shell show up as minor blips in the stress strain graph in Figure 3.9c which may imply the TiAk shell isn't carrying much of the load.

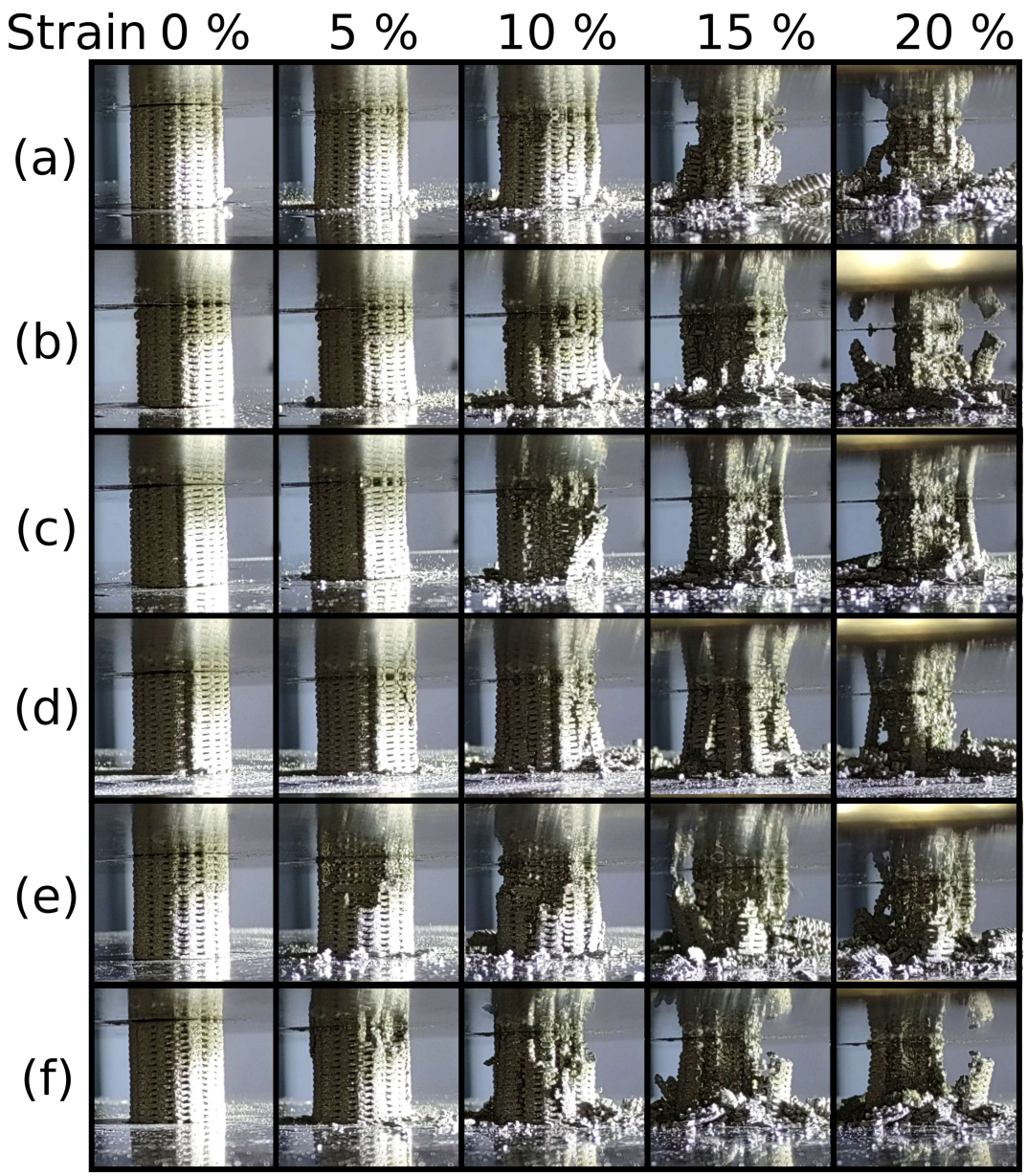

Figure 3.11: Uncontained failure of CS (Ti) (TiAk) samples, (a) through (f), with shell detachment during compression testing.

3.6.3. Core-shell failure mode Core = TiAk Shell = Ti

When the core and shell material is swapped the mechanical strength increases dramatically. The area of the scaffold made from Ti increases from approximately $20\,\mathrm{cm}^2$ to almost $60\,\mathrm{cm}^2$, a three times increase. Similarly, the yield strength increases similarly from $134\,\mathrm{MPa}$ to $301\,\mathrm{MPa}$, a 2.2 times increase. Having Ti as the shell also keeps any pieces of the core contained. This difference is clear from the still images taken during compression, shown in Figure 3.12 during failure the TiAk core remains fully contained.

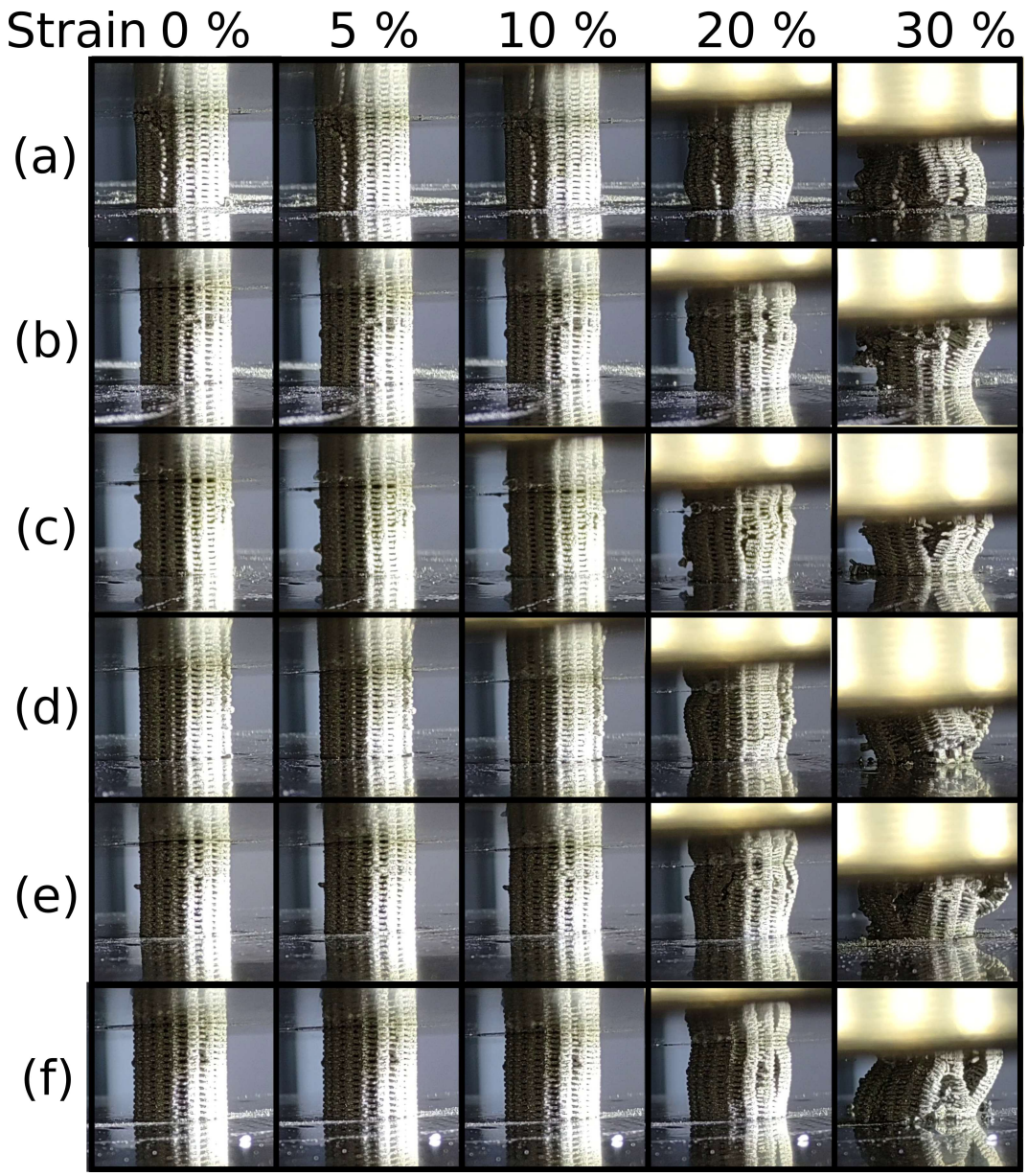

Figure 3.12: Fully contained failure of CS (TiAk) (Ti) samples, (a) through (f), with shell buckling during compression testing.

3.6.4. Variability of extrusion-based 3D printed scaffolds

Despite procedure and parameters being fixed between prints the variance between batches of the same type was much larger than variances within a batch. Even when two batches were printed on the same day, with the same pressure the weight of the scaffolds could differ by over 20% both ways.

For this reason the mechanical test results were always taken from a single batch, rather than trying to combine two batches that are the same in name only.

The only difference between batches like these is that before printing ink was mixed anew, and a new conical tip was used. The exact cause is unknown but it could be the ink drying during mixing, or perhaps the nozzle tip being slightly different each time. It could even be the amount of air bubbles introduced during mixing. Regardless, of which of these, if any, is the biggest contributor proper control over the flowrate would mitigate ink drying and differences between the conical tips.

3.7. Summary of results chapter

The composite with akermanite did succesfully sinter. But the mechanical strength of these samples was almost eight times lower than the same geometry made from Ti6Al4V, though their stiffness was also slightly lower. The core shell scaffolds did offer good mechanical properties but the CS Ti TiAk configuration had a problematic failure mode where the shell shattered with a lot of debris.

The akermanite composite alone was not able to absorb as much energy (brittleness) and yielded at a minimal deformation. Despite this it should be noted that the yield strength of the Ti6Al4V + akermanite samples imply they would be strong enough to serve as a (trabecular) bone scaffold though their low toughness[1] means they are a less than ideal candidate for it.

[1] the ability to absorb energy without breaking

4

Discussion

4.1. Mechanical test results

Mechanical properties obtained from the mechanical test show the samples aren't overly stiff yet still hold substantial strength. In fact the stiffness of the Ti scaffold was hundreds of times lower in compression than solid Ti6Al4V [28]. While the porous design played a role in this, partial sintering can as well. In SEM images individual Ti6Al4V particles were still distinguishable in with a sintering time of $2\,\mathrm{h}$ but barely when sintered for $6\,\mathrm{h}$. Additionally, the partial sintering also leads to less part shrinkage, but has limited influence on porosity. Furthermore, the partial sintering is a global operation which affects the entire scaffold, as such it can be complementary regardless of the design.

Composite scaffolds made from TiAk composite without reinforcing structure didn't fare as well, and despite only 10w% of the composite being akermanite onset of failure happened at just a few % of strain. The brittleness of akermanite [29] dominated the composite's behavior.

HH scaffolds which have an abrupt transition from Ti to TiAk composite halfway, performed similar to those entirely consisting of TiAk, and there was no significant difference in Young's modulus and yield strength between these two groups.

CS scaffolds were the strongest and stiffest in the test group, using the Ti in either the core or the shell makes them much stronger than using TiAk alone. The CS TiAk Ti scaffold was the stiffest and had the highest yield strength but neither of these were it's most noteworthy property. What really set it apart from the CS Ti TiAk scaffold was it's failure mode, which unlike with CS Ti TiAk was fully contained under compressive loading. Stiffness of the CS TiAk Ti scaffolds could be reduced further by manipulating the sintering time or decreasing the thickness of the Ti shell.

4.2. Comparison Between the Mechanical Properties of Porous Scaffolds and Those of Human bone Tissue.

In previous discussions of the results the properties of scaffolds created for this study were compared to each other. In this section instead we will take a look at how they stack up against human bone. In particular we'll break down how stiffness and strength of scaffolds compares to both trabecular and cortical bone. Rather than look at bone from very specific locations the high and low end of the range will be specified. Data on compressive elastic modulus and compressive yield strength for the comparison was obtained from [30] and [31].

In Figure 4.1 the stiffness is displayed from low to high. Ti scaffolds are on the high end of the trabecular range. Composite TiAk scaffolds which are presumed[1] to have higher osteo-inductive properties fall in the middle of this range.

The CS scaffolds with a TiAk core and Ti shell performed most similar to cortical bone. In terms of

[1] Though no assay has been done in this study to prove or disprove it.

stiffness they were identical to the low end of cortical bone. In terms of yield strength these scaffolds exceeded even the high end of cortical bone.

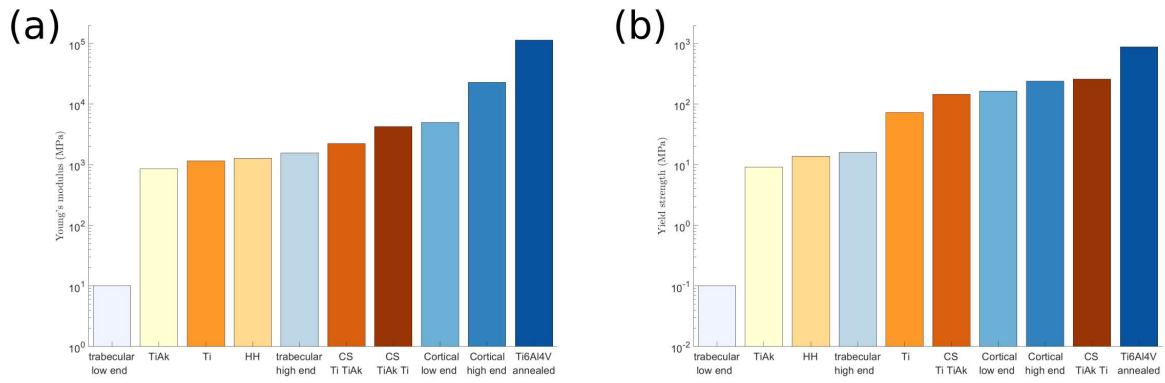

Figure 4.1: A comparison of (a) stiffness and (b) strength between the scaffolds produced in this study and reference data for cortical and trabecular bone. This reference data was obtained from [30] and [31]

4.3. Reflection on the research questions

Primarily the goal of this thesis project has been to answer the research questions, now the time has come to reflect on them. The research questions were:

- Can mechanical properties similar to that of bone be obtained with Ti6Al4V through design and sintering conditions?
- Will interfaces between Ti6Al4V and akermanite-Ti6Al4V composite successfully bond?
- Do these multifunctional scaffolds still have sufficient mechanical properties compared to bone?

Two out of three initial hypotheses to these questions were correct, namely the first two. Which stated that, this could be done, and this will happen, respectively. However, for the second it may be argued that the composite wasn't one containing any akermanite, after sintering.

The third hypothesis predicted that the multifunctional scaffolds would have sufficient mechanical properties compared to bone because these TiAk composites also had substantial amounts of strong Ti6Al4V. It turned out that isn't really true, on their own the TiAk composite scaffolds were 15-20 times weaker than cortical bone. Which puts it in the high end of the trabecular range instead. However, by combining the two types in a core-shell design the compressive yield strength of cortical bone was even exceeded at similar stiffness.

4.4. Discussion on defects mitigation

In the results a number of defect types were presented, namely, broken strands, sagging, coalescence and air inclusions. Regrettably mitigating one of these may introduce new issues and fixing one without introducing new issues require a very different approach.

By far the most common defect is air inclusions, that come from mixing a powder ,which has air sitting between particles, with a liquid binder. In order to get the air out, one may be tempted to apply a vacuum or centrifuge the ink. However, neither of those will affect just the air. Pulling a vacuum, for example, will also boil the water in the ink. Centrifuging will certainly help make the air move up, but will also make the heavy particles move down. Not to say centrifuging is entirely pointless, but the resulting pellet and supernatant need to be mixed again. And, this will re-introduce air.

As mentioned before one issue can be solved, but it will create a new different issue. In the case of air inclusion, reducing the viscosity, will make air rise quicker and particles sink faster. A weak agitator can then be used to prevent the particles from falling out of solution while not introducing new air.

Sagging is an issue relating to ’long’ overhangs or those at extreme overhang angles. Gravity is exerted on segments that can’t cope and the most straightforward solution is to put support material under these segments. In some cases small changes to the design or changing the print orientation can also work, but support material is the most general.

Finally, coalescence and strand break. Both of these problems can be caused by wrong flowrate for the current speed of the printhead. Strand break can also be caused by air in the ink, which was already addressed. Making the flowrate correct for the current speed of the printhead will reduce such defects. However, with the pressure driven extrusion on the stock Gesim Bioscaffolder it will always be wrong some of the time.

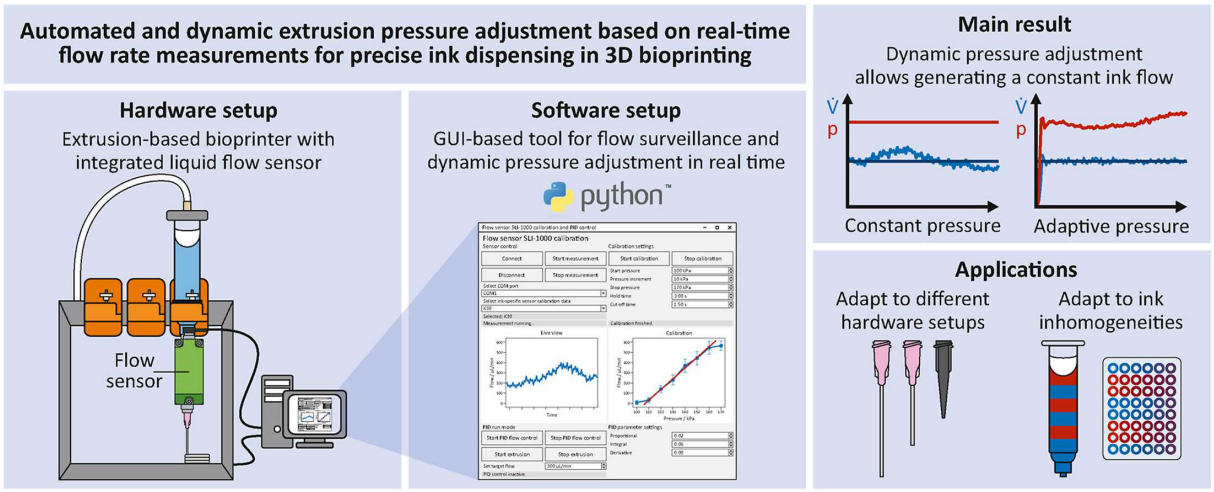

Figure 4.2: Graphical abstract of closed-loop flow control on Gesim Bioscaffolder reproduced from [32]

4.5. Recommendations for a more versatile printing platform

Direct ink writing has proven itself to be a very capable technique for additive manufacturing objects from a wide range of materials. While the Gesim Bioscaffolder intended application is bio-scaffold fabrication, it performs remarkably well for printing non bio-inks too. The Gesim Bioscaffolder is, however, lacking in a number of areas. This section will identify those shortcoming followed by recommendations.

1. Pressure based rather than volumetric extrusion gives unpredictable results with poor repeatability.
2. Multi material printing in practice doesn't work that well, because of ink drying in the tip.
3. Multi material printing is limited to at most 3 unique compositions[2].
4. The stiff and heavy construction negatively impact speed and acceleration.
5. The printing volume is limited to the cartridge size of either $10\,\mathrm{mL}$ or $30\,\mathrm{mL}$.
6. Unstable ink can not be used[3].
7. No documented hardware interfaces are available to implement advanced features.
8. No application programming interface (API) documented[4].

4.5.1. Volumetric extrusion with open and closed systems

The first item on the list of shortcomings is about pressure based extrusions. Bio-printers that use this type of extrusion, in open-loop, will inevitably produce parts that differ from their CAD model. The important flowrate variable is not controlled, in fact by fixing the pressure the flowrate will certainly be wrong some of the time as printhead velocity isn't constant. An attempt can be made to decrease the discrepant relation between the desired and actual flow. Making the pressure dependent on the flowrate requested by gcode is one approach, and this can work if the flow-pressure relation is known and this relation is time-invariant. Often this relation, however, is neither known nor time-invariant[5]. With closed-loop control the system tracks the flow of a volumetric extrusion based system which is the desired behaviour.

Downsides of pressure based extrusions are well known and correction by means of closed-loop control or by switching to a different mechanism have been proposed. For the Gesim Bioscaffolder, in particular, Werner et al [32] used a SLI-1000 flow meter (Sensirion, Stäfa, Switzerland) for closed-loop control. Because of point 7 and 8 on the list this, however, was a precarious undertaking. Their implementation relied

[2]Unless cartridges are swapped manually.

[3]Pressurized cartridges filled with ink are difficult to agitate

[4]An API allows communication with external software, without it external control inputs can only be entered through the graphical user interface (GUI).

[5]Not known because of batch-to-batch variations. Not time-invariant because: ink mixtures have inhomogeneities, nozzle fouling can causes back pressure and even factors such as cartridge fill level can play a role.

on first extracting the flowrate readings from the sensor, passing that to a software based[6] PID controller and feeding the output (pressure setpoint) back into Gesim Robotics. Because there was no (documented) API the values had to be set via the graphical user interface also controlled through Python. The technique did lead to an improvement in setpoint tracking for a fixed setpoint as can be seen in the results in Figure 4.2.

Performance improvements in this paper came at a cost, but not only due to the increased complexity. In a few tests the PID loop was unstable and went into an oscillatory state. Constantly chasing the setpoint, applying too much pressure, overshooting, reducing pressure too much, undershooting etc. There are also questions that aren't answered about dynamic performance such as what is the response time, what is the settling time and how much overshoot is there? A much more fundamental question is why, why insist on pressure based extrusion when volumetric alternatives exist? For bio-inks, pressure driven extrusion has the benefit applying lower shear than some mechanical driven systems and thus destroying fewer cells [33]. Additionally, there are single use options available that minimize the risk of cross contamination between batches. These factors undoubtedly played a role in favour of pneumatic extrusion, not only by Gesim in their Bioscaffolder, but also in other bioprinters, such as the R-GEN 100 by REGENHU (ZI du Vivier 22, 1690 Villaz-St-Pierre, Switzerland).

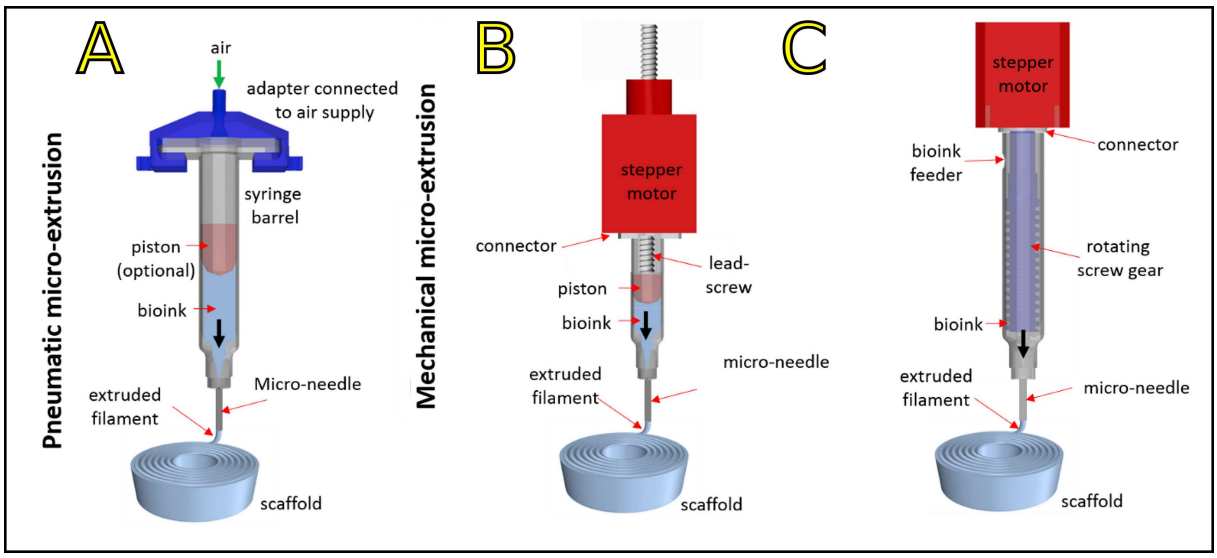

Figure 4.3: Various extrusion mechanisms for bioprinting. With **A** a pressure based system similar to what is used in the Gesim, **B** a syringe pump and **C** a screw pump adapted from [33]

When the bio-printing design constraint is dropped, in other words, if regular inks without cells are used the issue goes away, and a wide variety of extrusion mechanisms is suitable. A selection of mechanisms can be seen in Figure 4.3. Note that **A** and **B** are closed systems where it's not possible to add material while it's running. On the other hand, a configuration like **C** can be filled while it's running. This may seem like a trivial property, for now, but it will become clear why it is vital for further recommendations. As mentioned previously the lack of flowrate control makes **A** less suitable. While **B** is a volumetric extrusion method, the discrete nature of the (stepper) motor creates pulsating flow. Finally, **C** has the same pulsating problem but unlike the others it can be fed with new material without need to dissamble.

[6] written in Python

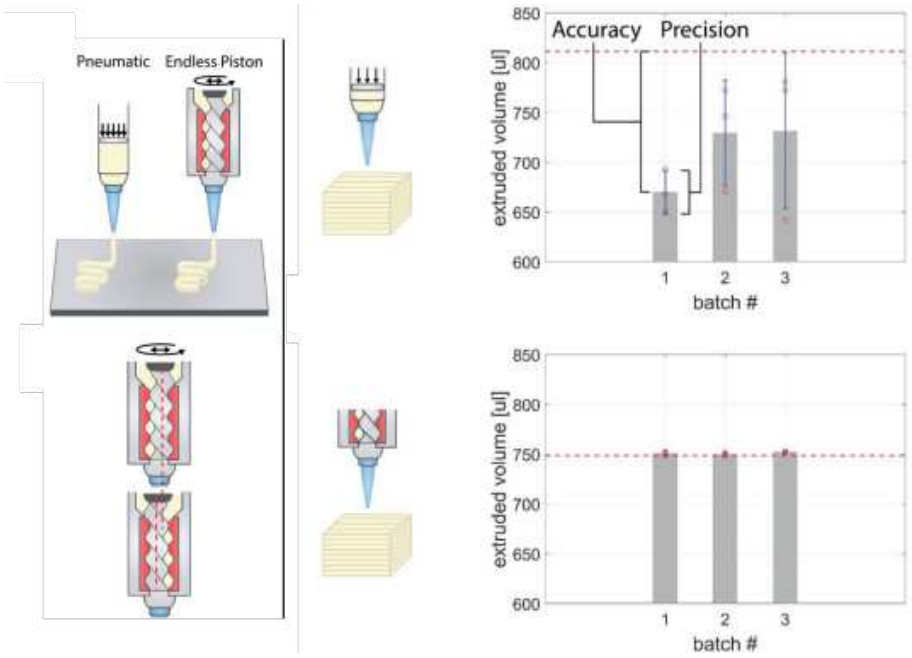

Figure 4.4: The eccentric endless cavity of the PCP pump compared to pneumatic extrusion (left) and the differences in accuracy and precision (right) adapted from [34]

Another pump type exists which is the progressing cavity pump (PCP), this pump type is often overlooked and a paper from 2020 claims to be the first to use this type of pump for bioprinting [34]. In the PCP mechanism, as the name implies, fluid filled cavities are moved from a reservoir side to a dispensing point. Not only can they be fed from the top during operation they also offer nearly continuous flow, high volumetric accuracy, operation over a large viscosity range, the ability to pump slurries and low applied shear stresses. Fisch et al [34] found that these pumps offered 41 times higher accuracy and 35 times higher precision than a pneumatic mechanism. Nearly as remarkable was the cell viability which only dropped 3% compared to the pneumatic method. An infographic of the PCP pump and it's performance in this study can be seen in Figure 4.4. For all these reasons the PCP pump seems like a well suited choice not just for non bio DIW but just as much for bio-printing.

A discussion of the PCP pump [35] wouldn't be complete without listing its lesser aspects. First of all is the eccentric motion of the pump shaft, instead of rotating around an axis the shaft moves from side to side. A specialized coupling is needed to drive it from a rotating motor axis. The pump design has a rotor and a stator, the stator cavity has N lobes, the rotor always has 1 lobe less. An interesting consequence is that as number of lobes increases the less eccentric it becomes, similarly, the more lobes the pump has the longer it needs to be to achieve good sealing performance. For bio-printing in particular the requirement for the pump surfaces to be either single use or sterilizable can also be problematic. The PCP pump is made up of two precision parts, single use parts would therefore be extremely costly, disassembly and autoclaving would be cumbersome, this is a clear downside to this otherwise superior pumping mechanism.

4.5.2. Fully automated (massive) multi material operation

In the previous section an extrusion mechanism, superior to pressure driven extrusion, was identified. This PCP type pump has a linear relation between motor rotation speed and flowrate. It is more accurate and precise than the non volumetric pressure driven approaches. Additionally, it is an open system. The material at the inlet side is at atmospheric pressure, and it stays that way even if the pump is operating. This last property is vital in the implementation of automated multi material operation as well as unstable ink dispensing.

The major problems with multi material printing on the Gesim Bioscaffolder is that ink in one nozzle dries out while another nozzle is printing. Since the ink is formulated such that it dries within minutes

this inherent behaviour can not be changed. There are workarounds like occasionally wetting the nozzle that is not in use to prevent the ink from dying out. Under the assumption that the input material can be changed automatically, two possible solutions for this problem could be: 1) only using a single nozzle for all materials or 2) purging any idle nozzles with a solution that doesn't dry out and clog. This is where the open nature of the PCP pump comes in, it allows a user to add material without disassembly.

A multi material printing system designed on either of these bases would have at least three (but preferably four) PCP pumps and one stirring mechanism. For the single nozzle case one PCP pump is on the printhead dispensing from the accompanying ink reservoir, another is on a mixing stage which purpose is to deposit mixed materials into the ink reservoir. The other two pumps are dedicated for dispensing component A and B into the mixing stage. A schematic of this setup can be seen in Figure 4.5. Optionally, the mixing stage can be incorporated into the printhead ink resevoir which would thus require only 3 PCP pumps, but that'd be heavy and take up valuable space. To overcome the slow speed and acceleration that plagues the Gesim Bioscaffolder (item 4 on the list of shortcomings) keeping the printhead mass low is vital.

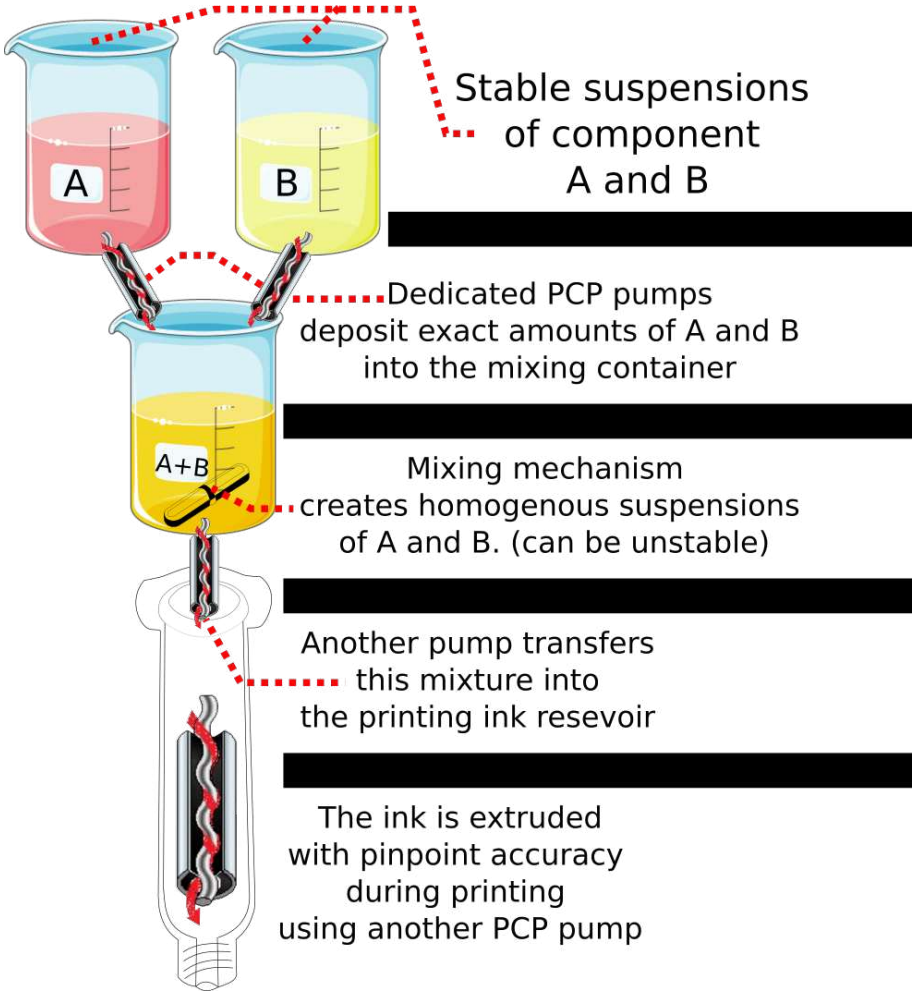

Figure 4.5: Graphical illustration of multi material printing system, illustrations obtained through Wikimedia commons: beaker (smart servier), and pcp pump (Gbmc2010)

A setup like this can be expanded with additional compounds from which, any desirable ratio can be created, and thanks to the PCP pumps all this can be done with sufficient accuracy. Every layer can be made up of a different material, with proper implementation (hardware, firmware, slicer) many different mixtures can even be used within a single layer. Less stable inks can also be used since stability is only required for the duration of one layer rather than the entire print process, simply mix component **A** (stable ink) with component **B** (a liquid, water for example) and print. This flexibility makes it a versatile multi

material system. There are use cases where cross contamination needs to be avoided and then there is the choice of dedicated extruder (either on their own printhead or all on the same printhead like the Gesim has) or purging with some cleaning liquid. As discussed earlier the additional extruder can contain a watery solution that doesn't dry out/clog, while idle.

4.5.3. Support materials for use in direct ink writing

Support materials in fused filament fabrication

Additive manufacturing is sometimes talked up as a disruptive technology, giving engineers unlimited design freedom with regards to the geometry. In reality though, this is never really the case. The designer is limited by the process limitations, and must take them into account during design (Design for manufacturing). In extrusion based printing overhangs and thin parts can be problematic, in a way that isn't really the case for processes like selective laser melting (SLM). In SLM even if an area is unsupported, the powder bed will ensure it doesn't collapse, however, a very rough surface will remain. It would be advantageous to have a material that can be deposited as support, or perhaps an augmented new printing method for the DIW process.

Even in fused filament fabrication (FFF) dedicated support material is only rarely used and there can be many reasons for this. A common reason is undoubtedly that there is no second extruder, therefore the printer cannot do it. But other factors such as support material cost and support material adhesion may play a role as well. In some cases using the main material as support material is sufficient. Support material in FFF also requires post processing, generally this involves dissolving; in water (Polyvinyl Alcohol), acetone (Acrylonitrile butadiene styrene), limonene (High impact polystyrene) or sodium hydroxide (Polylactic acid). For the DIW of metal suspensions, followed by high temperature sintering, these plastic filaments could already suffice as support. However, pyrolysis leaves behind a substantial amount of carbon residue. Preferably a part is completely free of support material and residue after processing.

Ionic compounds as an alternative to polymeric supports

Three materials were identified as potential support material candidates for DIW of non bio inks. Namely, ammonium bicarbonate, sodium chloride, and potassium sulfate. These three salts do not leave behind residue after post processing. Ammonium bicarbonate in particular has only gaseous decomposition products at elevated temperatures. Sodium chloride and potassium sulfate have relatively high melting points and are water soluble. Because the Ammonium (bi)carbonate decomposes at low temperatures, it will bear no load at sintering temperatures, therefore a requirement remains that the dried metal ink needs to, at least, be able to bear it's own weight. Sodium chloride (Mp = $801\,^{\circ}$C[36]) and Potassium sulfate (Mp = $1069\,^{\circ}$C[37]) on the other hand, will be able to offer support due to their higher melting points [38]. A summary of the presumed pros and cons of these three materials is given in Table 4.1, the rest of this section elaborates on this table.

Table 4.1: Summary of pros and cons of support ink based on ammonium bicarbonate, sodium chloride and potassium sulfate.

	Upsides What beneficial properties does the material offer as support?	**Unknowns** What influences may or may not be important?	**Downsides** What detrimental properties can be expected?
Ammonium bicarbonate	1. Decomposition leaves no residue 2. Sintering/Debinding removes the support, there is no post processing 3. Low cost and available in high purity	1. Compatiblity with rheology modifiers 2. Moderate water solubility may cause support defects	1. Ammonia gas released during thermal decomposition 2. Only offers support during printing 3. Decomposition is strongly endothermic
Sodium chloride	1. Low toxicity at low concentrations 2. Low cost and available in high purity	1. Compatiblity with rheology modifiers 2. Moderate water solubility may cause support defects 3. Reactions betweent the support and base material	1. Relatively low melting point 2. Solutions are corrosive especially to iron alloys 3. Surface inclusions may happen during sintering
Potassium sulfate	1. Low toxicity at low concentrations 2. Low cost and available in high purity 3. High melting point	1. Compatiblity with rheology modifiers 2. Moderate water solubility may cause support defects 3. Reactions betweent the support and base material	1. Surface inclusions may happen during sintering 2. Blood plasma content of Potassium and Sulfate are much lower than Sodium and chloride ions.

Practical limitations of ionic compound systems

This section is about providing ideas for what might be good support materials, and identifying some of the pitfalls early on for whomever uses these recommendations as a starting point. There is, to my knowledge, no literature using these salts as support material. However, properties like melting point, water solubility, additive interaction and toxicity can be used to make an educated guess about applicability. Ammonium bicarbonate isn't toxic and easy to get rid of in full, but decomposition is highly endothermic, and one of the reaction products is ammonia gas. Because the ammonia gas is an undesirable side product of the decomposition, ammonium bicarbonate is a much preferred option over ammonium carbonate. As it decomposes into twice as much carbon dioxide and half as much ammonia per mol.

Neither of the high melting point salts maintains their solid state at the $1200\,^{\circ}$C sintering temperature, which is what was used in this study for the Ti6Al4V. However, sintering does commence at lower temperatures, but at a reduced densification rate. Sodium chloride was chosen as a candidate because it's abundantly available, has a high melting point, moderate solubility in water and low toxicity. Potassium sulfate is similar but has an even higher melting point, few ionic compounds have a melting point this high[7].

Water solubility is useful for removing the support material after sintering, but it can create difficulties when printing the support. Upon drying a layer of support the water will become supersaturated with salt. Salt in solution will crash out and form crystals when this happens, and this may create printing defects. There are solvents such as ethanol in which (practically) none of these salts dissolve. Furthermore, rheology modifiers and binders exist for ethanol as well, thus support ink formulations with ethanol instead of water are plausible. Ultimately, it is still unclear whether the crystallization upon drying is actually an unaddressed challenge or insignificant footnote.

[7] One example of a salt with a nearly as high melting point is sodium fluoride, it's a nasty compound compared to potassium sulfate.

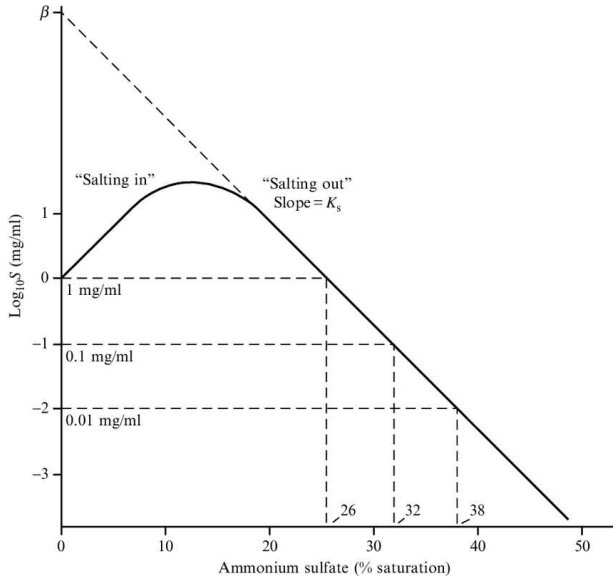

Figure 4.6: Protein[8] solubility as a function of ammonium sulfate concentration reproduced from [39]

When the support ink is made up of only water and a dissolved salt[9] no rheology modifier to increase the viscosity will be needed. Nearly saturated solutions are very stable, unless they get supersaturated when some solvent is evaporated. Additionally, since all the salt is in solution, in other words the are no solid particles, this support ink can flow through a very small nozzle without clogging. However, such a solution will become a loose powder when the solvent is evaporated, and for this reason it is desirable to have some binder. When the support ink is loaded with quantities above the solubility limit then it is not longer stable [10] and countermeasures need to be taken to stabilize the ink. These can be to increase the viscosity of the solution or reduce the size of the salt particles, both will increase the settling time. Increasing the viscosity may not be straightforward, as it was with the Ti6Al4V powder, unlike these salts Ti6Al4V is completely insoluble in water. Because the salts do dissolve in water interactions with the rheology modifier are to be expected.

A phenomenon known as salting-out [40, 41] shifts the solubility limit of large molecules, like methylcellulose, downwards. The sodium, ammonium and potassium cation, and chloride, carbonate, and sulfate anion can cause salting out. The tendency to salt out is given by the Hofmeister series, Which is given by the following inequality "$Li^+ > Na^+ > K^+ > Cs^+$ and $SO_4^{2-} > F^- > Cl^- > Br^- \gg I^- > SCN^-$" [40]. Ions left of the double inequality sign cause salting out. When salting-out happens the homogeneous viscosity of the liquid is lost and the ink will not be stable.

Large molecules, however, first salt-in (becoming more soluble) before salting out. The solubility curve for large molecules has a hump going from the baseline solubility up to a maximum, and coming back down to the baseline. This baseline value depends on ions in the salt and how soluble the salt is. An illustration of this hump is presented in Figure 4.6 which shows both salting-in and salting-out. This property can be exploited to keep the large binder molecules dissolved while also having some amount of salt in solution.

The compatibility of these salts with the deposited metal particles is also unclear. During printing, salt from the support material may seep between the metal particles. There it might be difficult to leech out, especially if it's trapped during sintering. Additionally, reaction products may be created. The chloride and sulfate cations might damage the metal surface at elevated temperatures. This issue is non-existent

[8] Or rather large molecule in general.

[9] in quantities below the solubility limit

[10] all three salts have densities unequal to water

with ammonium bicarbonate as it will evaporate at low temperatures, and the gaseous nature of it's decomposition products means it can escape even through small pores.

Ammonium bicarbonate has one additional problem: it is inherently unstable when moist, it breaks down gradually even at room temperature [42]. This means it can't be in the moist state for extended amounts of time. It's likely not an issue in the printing reservoir, because ammonia and carbon dioxide [11] will accumulate in a closed container, making further decomposition thermodynamically unfavourable. Therefore, losses are assumed to be minor. When the support ink is deposited in a thin layer and dried slowly though it could be that by the time the moisture is gone, so is the ammonium bicarbonate. For this reason and the salting out mentioned earlier, ethanol and a compatible binder, such as ethylcellulose may be needed.

Potassium sulfate ($111\,\mathrm{g\,kg^{-1}}$, [37]) is less soluble than either ammonium bicarbonate ($210\,\mathrm{g\,kg^{-1}}$, [42]) and sodium chloride ($358\,\mathrm{g\,kg^{-1}}$, [36]).[12] Because of it's lower solubility, even at the solubility limit of $111\,\mathrm{g\,kg^{-1}}$, large molecules may not settle-out. If there is no settling-out at saturation, the ink can be heavily loaded with potassium sulfate just as is the case with titanium particles. Mcbain et al reported this very behaviour for potassium sulfate and the protein based biopolymer gelatin [43], in this work a 10% solution of gelatin did not salt-out despite it being saturated with potassium sulfate.

Thermal expansion can also cause trouble, again for ammonium bicarbonate this is not relevant as it decomposes before significant thermal expansion occurs. Additionally, the thermal expansion depends on the particular metal and the temperature. If the volumetric expansion across the entire sintering temperature range is almost equal between the support and base material then it is far less likely that there would be an issue. The inverse is also true as the shrinkage on cooling down will be almost equal, though at that point the metal will be sintered and not as easily deformed by the salt. While limited data is available near the melting points of sodium chloride and potassium sulfate some data is available at lower temperatures.

Thermal expansion happens in all three dimensions, remarkably for potassium sulfate not all directions in a crystal have the same thermal expansion coefficient [44]. Because there will be many different grains of potassium sulfate as well as a non uni-directional orientation within these grains, on average this gives the same thermal expansion in all directions. Volume changes in literature are often expressed in the relative volume change $\frac{V}{V_0}$. At $500\,^\circ$C $\frac{V}{V_0}$ [13] is equal to 1.07, 1.05 and 1.02 for sodium chloride [45], potassium sulfate [44] and Ti6Al4V[46], respectively. Based on these values thermal expansion may be an issue, at least for Ti6Al4V. But metals such as magnesium alloy which have a higher coefficient of thermal expansion [47] may not have any issues, as their $\frac{V}{V_0}$ is near 1.05.

Concluding statement

Taking all these factors into account ammonium bicarbonate and potassium sulfate appear as most favourable candidates. Both have some benefits and some drawbacks. Most importantly potassium sulfate can (probably) be used with water and methylcellulose, does not break down over time, and will offer support during sintering. However, the salt may damage the part during sintering, thermal expansion differences may crack the part on heating and removing the support requires a salt-leeching step. Ammonium bicarbonate on the other hand will not require post processing, but will (probably) require an organic solvent such as ethanol and specialized binders. Since the ammonium bicarbonate may require a flammable organic solvent, in order to to eliminate salting out and room temperature decomposition, it seems less favourable than potassium sulfate in that regard. However, if a support material is needed that will leave (almost) no residue then ammonium bicarbonate may still be the best choice.

[11] From the decomposition of ammonium bicarbonate in water.

[12] All solubility values taken at $20\,^\circ$C.

[13] with V_0 taken at $20\,^\circ$C

5

Conclusion

In this thesis direct ink writing was used to create multifunctional scaffolds. Partial sintering was used in one case as a method to reduce the overall stiffness. This methods was used successfully, and it was possible to create pure Ti scaffolds with stiffness comparable to the high end of the trabecular range. The multimaterial multifunctional core shell scaffolds had stiffness similar to the low end of the cortical range. Both types of scaffolds boasted strength similar or better than real trabecular and cortical bone, respectively.

Multi material scaffold manufacturing was systematic and uneventful. There were no technical limitations that limit the amount of compositions that could be used in one print, but a practical limitation is only three inks can be installed on the machine at any one time. Using more inks than this requires many manual actions by the operator. Four types of manufacturing related defects were identified. There were strand break, sagging, air pockets and coalescence. For each, a (partial) fix was identified, however, for the failures related to air in the ink the fix may lead to stability problems.

It was found that Ti6Al4V + akermanite composites (90:10w%) could be sintered and interface with Ti6Al4V. The composite itself was found to be relatively weak with a yield strength of only 9.2 $\pm$ 2.5 MPa, however it had a comparable low stiffness of 858 $\pm$ 61 MPa. This puts the composite in the middle of the trabecular range. Upon inspection of the failure mode though it became clear that using it on it's own as a bone implant would be ill advised. The composite tended to crack and shatter with minimal energy absorbed.

The core shell design with the Ti6Al4V + akermanite composite as the core and a Ti6Al4V shell, the poor yield strength of the composite was less critical. Even if it were to crack in this configuration the loose particles were contained within the Ti6Al4V shell. The compressive elastic modulus was 4250 $\pm$ 371 MPa and the yield strength 260 $\pm$ 11 MPa. In summary this core shell scaffold had mechanical properties far superior to the plain composite but still, potentially, maintains the added function of promoting osteo-induction.

References

[1] Filippo Migliorini et al. “Strategies for large bone defect reconstruction after trauma, infections or tumour excision: a comprehensive review of the literature”. In: *European Journal of Medical Research 2021 26:1* 26.1 (Oct. 2021), pp. 1–10. DOI: 10.1186/S40001-021-00593-9. URL: https://eurjmedres.biomedcentral.com/articles/10.1186/s40001-021-00593-9.

[2] Ahmad Oryan et al. “Bone regenerative medicine: classic options, novel strategies, and future directions”. In: *Journal of Orthopaedic Surgery and Research* 9.1 (Mar. 2014), p. 18. DOI: 10.1186/1749-799X-9-18. URL: /pmc/articles/PMC3995444/%20/pmc/articles/PMC3995444/?report=abstract%20https://www-ncbi-nlm-nih-gov.tudelft.idm.oclc.org/pmc/articles/PMC3995444/.

[3] Caoimhe Kiernan et al. “Endochondral Ossification: Recapitulating Bone Development for Bone Defect Repair”. In: *Developmental Biology and Musculoskeletal Tissue Engineering: Principles and Applications* (Jan. 2018), pp. 125–148. DOI: 10.1016/B978-0-12-811467-4.00006-1.

[4] Hao Chen et al. “Porous Scaffold Design for Additive Manufacturing in Orthopedics: A Review”. In: *Frontiers in Bioengineering and Biotechnology* 8 (June 2020), p. 535636. DOI: 10.3389/FBIOE.2020.00609/BIBTEX.

[5] Fuyuan Deng et al. “3D printed Ti6Al4V bone scaffolds with different pore structure effects on bone ingrowth”. In: *Journal of Biological Engineering* 15.1 (Dec. 2021), pp. 1–13. DOI: 10.1186/S13036-021-00255-8/FIGURES/10. URL: https://jbioleng.biomedcentral.com/articles/10.1186/s13036-021-00255-8.

[6] Naghmeh Abbasi et al. “Porous scaffolds for bone regeneration”. In: *Journal of Science: Advanced Materials and Devices* 5.1 (Mar. 2020), pp. 1–9. DOI: 10.1016/J.JSAMD.2020.01.007.

[7] Fei Liu et al. “Functionally graded porous scaffolds in multiple patterns: New design method, physical and mechanical properties”. In: *Materials & Design* 160 (Dec. 2018), pp. 849–860. DOI: 10.1016/J.MATDES.2018.09.053.

[8] Lorna J. Gibson et al. *Cellular Solids: Structure and Properties*. Cambridge University Press, 1990. Chap. 4, pp. 93–123. URL: https://books.google.com/books/about/Cellular_Solids.html?hl=nl&id=IySUr5sn4N8C.

[9] Lunguo Xia et al. “Akermanite bioceramics promote osteogenesis, angiogenesis and suppress osteoclastogenesis for osteoporotic bone regeneration”. In: *Scientific Reports 2016 6:1* 6.1 (Feb. 2016), pp. 1–17. DOI: 10.1038/SREP22005. URL: https://www-nature-com.tudelft.idm.oclc.org/articles/srep22005.

[10] Natalia V. Bulina et al. “A Study of Thermal Stability of Hydroxyapatite”. In: *Minerals 2021, Vol. 11, Page 1310* 11.12 (Nov. 2021), p. 1310. DOI: 10.3390/MIN11121310. URL: https://www.mdpi.com/2075-163X/11/12/1310/htm%20https://www.mdpi.com/2075-163X/11/12/1310.

[11] Hossein Mohammadi et al. “Microstructure evolution, grain growth kinetics and mechanical properties of Ca2MgSi2O7 bioceramics sintered at various temperatures”. In: *Processing and Application of Ceramics* 15.4 (2021), pp. 357–365. DOI: 10.2298/PAC2104357M. URL: https://doiserbia.nb.rs/Article.aspx?ID=1820-61312104357M.

[12] Paweena Diloksumpan et al. “Orthotopic Bone Regeneration within 3D Printed Bioceramic Scaffolds with Region-Dependent Porosity Gradients in an Equine Model”. In: (2020). DOI: 10.1002/adhm.201901807. URL: https://doi.org/10.1002/adhm.201901807.

[13] M A S R Saadi et al. “Direct Ink Writing: A 3D Printing Technology for Diverse Materials”. In: *Advanced Materials* 34.28 (July 2022), p. 2108855. DOI: 10.1002/ADMA.202108855. URL: https:

//onlinelibrary-wiley-com.tudelft.idm.oclc.org/doi/full/10.1002/adma.202108855%20https://onlinelibrary-wiley-com.tudelft.idm.oclc.org/doi/abs/10.1002/adma.202108855%20https://onlinelibrary-wiley-com.tudelft.idm.oclc.org/doi/10.1002/adma.202108855.

[14] Sigmund Arntsønn Tronvoll et al. “Investigating pressure advance algorithms for filament-based melt extrusion additive manufacturing: theory, practice and simulations”. In: *Rapid Prototyping Journal* 25.5 (Aug. 2019), pp. 830–839. DOI: 10.1108/RPJ-10-2018-0275/FULL/PDF.

[15] Reinout Holtrup. “Tuning liquefier dynamics: A strategy for accuracy improvement in extrusion based additive manufacturing with PEEK”. PhD thesis. URL: http://essay.utwente.nl/93386/.

[16] Anna Bellini et al. “Liquefier Dynamics in Fused Deposition”. In: *Journal of Manufacturing Science and Engineering* 126.2 (May 2004), pp. 237–246. DOI: 10.1115/1.1688377. URL: https://dx-doi-org.tudelft.idm.oclc.org/10.1115/1.1688377.

[17] *Kinematics - Klipper documentation*. URL: https://www.klipper3d.org/Kinematics.html.

[18] Vassilis Karageorgiou et al. “Porosity of 3D biomaterial scaffolds and osteogenesis”. In: *Biomaterials* 26.27 (Sept. 2005), pp. 5474–5491. DOI: 10.1016/J.BIOMATERIALS.2005.02.002.

[19] James H. Gosman et al. “Development of Cortical Bone Geometry in the Human Femoral and Tibial Diaphysis”. In: *The Anatomical Record* 296.5 (May 2013), pp. 774–787. DOI: 10.1002/AR.22688. URL: https://onlinelibrary-wiley-com.tudelft.idm.oclc.org/doi/full/10.1002/ar.22688%20https://onlinelibrary-wiley-com.tudelft.idm.oclc.org/doi/abs/10.1002/ar.22688%20https://anatomypubs-onlinelibrary-wiley-com.tudelft.idm.oclc.org/doi/10.1002/ar.22688.

[20] Yasser Shahzad et al. “Relevancy of Nizatidine’s Release from Floating Tablets with Viscosity of Various Cellulose Ethers”. In: *Sci 2021, Vol. 3, Page 22* 3.2 (Apr. 2021), p. 22. DOI: 10.3390/SCI3020022. URL: https://www.mdpi.com/2413-4155/3/2/22/htm%20https://www.mdpi.com/2413-4155/3/2/22.

[21] Chi L Li et al. “The use of hypromellose in oral drug delivery”. In: *Journal of Pharmacy and Pharmacology* 57.5 (May 2005), pp. 533–546. DOI: 10.1211/0022357055957. URL: https://onlinelibrary.wiley.com/doi/full/10.1211/0022357055957%20https://onlinelibrary.wiley.com/doi/abs/10.1211/0022357055957%20https://onlinelibrary.wiley.com/doi/10.1211/0022357055957.

[22] Ching Mien Oh et al. “A Study on the Impact of Hydroxypropyl Methylcellulose on the Viscosity of PEG Melt Suspensions Using Surface Plots and Principal Component Analysis”. In: *AAPS PharmSciTech* 16.2 (Apr. 2015), p. 466. DOI: 10.1208/S12249-014-0204-X. URL: /pmc/articles/PMC4370968/%20/pmc/articles/PMC4370968/?report=abstract%20https://www.ncbi.nlm.nih.gov/pmc/articles/PMC4370968/.

[23] Meriem Nadour et al. “Effects of Methylcellulose on the Properties and Morphology of Polysulfone Membranes Prepared by Phase Inversion”. In: *Materials Research* 20.2 (Jan. 2017), pp. 339–348. DOI: 10.1590/1980-5373-MR-2016-0544. URL: https://www.scielo.br/j/mr/a/GK9p3y4n9bpGv8FfRF5XngK/?lang=en.

[24] J.H. Shepherd et al. “Synthetic hydroxyapatite for tissue engineering applications”. In: *Hydroxyapatite (Hap) for Biomedical Applications* (Jan. 2015), pp. 235–267. DOI: 10.1016/B978-1-78242-033-0.00011-0.

[25] *B963 Standard Test Methods for Oil Content, Oil-Impregnation Efficiency, and Surface-Connected Porosity of Sintered Powder Metallurgy (PM) Products Using Archimedes’ Principle*. URL: https://www.astm.org/b0963-14.html.

[26] *ISO 13314:2011 - Mechanical testing of metals — Ductility testing — Compression test for porous and cellular metals*. URL: https://www.iso.org/standard/53669.html.

[27] R. Sh Mikhail et al. “Kinetics of the thermal decomposition of calcium hydroxide”. In: *Journal of Colloid and Interface Science* 21.4 (Apr. 1966), pp. 394–404. DOI: 10.1016/0095-8522(66)90005-5.

[28] ASM International. *Atlas of stress-strain curves.* ASM International, 2002, p. 816.

[29] Pei Feng et al. “Toughening and strengthening mechanisms of porous akermanite scaffolds reinforced with nano-titania”. In: *RSC Advances* 5.5 (Dec. 2014), pp. 3498–3507. DOI: 10.1039/C4RA12095G. URL: https://pubs-rsc-org.tudelft.idm.oclc.org/en/content/articlehtml/2015/ra/c4ra12095g%20https://pubs-rsc-org.tudelft.idm.oclc.org/en/content/articlelanding/2015/ra/c4ra12095g.

[30] Xue-Nan Gu et al. “A review on magnesium alloys as biodegradable materials”. In: (). DOI: 10.1007/s11706-010-0024-1.

[31] Lutz Christian Gerhardt et al. “Bioactive Glass and Glass-Ceramic Scaffolds for Bone Tissue Engineering”. In: *Materials 2010, Vol. 3, Pages 3867-3910* 3.7 (July 2010), pp. 3867–3910. DOI: 10.3390/MA3073867. URL: https://www.mdpi.com/1996-1944/3/7/3867/htm%20https://www.mdpi.com/1996-1944/3/7/3867.

[32] Lukas Wenger et al. “Automated and dynamic extrusion pressure adjustment based on real-time flow rate measurements for precise ink dispensing in 3D bioprinting”. In: *Bioprinting* 28 (Dec. 2022), e00229. DOI: 10.1016/J.BPRINT.2022.E00229.

[33] Ibrahim T. Ozbolat et al. “Current advances and future perspectives in extrusion-based bioprinting”. In: *Biomaterials* 76 (Jan. 2016), pp. 321–343. DOI: 10.1016/J.BIOMATERIALS.2015.10.076.

[34] Philipp Fisch et al. “Improved accuracy and precision of bioprinting through progressive cavity pump-controlled extrusion”. In: *Biofabrication* 13.1 (Dec. 2020), p. 015012. DOI: 10.1088/1758-5090/ABC39B. URL: https://iopscience.iop.org/article/10.1088/1758-5090/abc39b%20https://iopscience.iop.org/article/10.1088/1758-5090/abc39b/meta.

[35] Christian. Wittrisch et al. *Progressing cavity pumps : oil well production artificial lift*, p. 219. URL: https://www.worldcat.org/title/841495156.

[36] *Sodium chloride | ClNa | ChemSpider*. URL: https://www.chemspider.com/Chemical-Structure.5044.html?rid=9ea78b73-c016-4365-a6e5-243019d88df7.

[37] *Potassium sulfate | K2O4S | ChemSpider*. URL: https://www.chemspider.com/Chemical-Structure.22915.html?rid=85d6cdd1-6e9f-4390-af36-653435dcc039.

[38] *The Merck Index Online - chemicals, drugs and biologicals*. URL: https://merckindex.rsc.org/.

[39] Richard R. Burgess. “Chapter 20 Protein Precipitation Techniques”. In: *Methods in Enzymology* 463.C (Jan. 2009), pp. 331–342. DOI: 10.1016/S0076-6879(09)63020-2.

[40] Koji Nishida et al. “Salting-out and salting-in effects of amphiphilic salt on cloud point of aqueous methylcellulose”. In: *Process Biochemistry* 59 (Aug. 2017), pp. 52–57. DOI: 10.1016/J.PROCBIO.2016.12.009.

[41] Yirong Xu et al. “Controllable gelation of methylcellulose by a salt mixture”. In: *Langmuir* 20.15 (July 2004), pp. 6134–6138. DOI: 10.1021/LA049907R/ASSET/IMAGES/MEDIUM/LA049907RN00001.GIF. URL: https://pubs.acs.org/doi/abs/10.1021/la049907r.

[42] Karl F. Tiefenbacher. “Technology of Minor Ingredients for Wafers and Waffles”. In: *Wafer and Waffle* (Jan. 2017), pp. 227–311. DOI: 10.1016/B978-0-12-809438-9.00004-1.

[43] James W. McBain et al. “THE SALTING OUT OF GELATIN INTO TWO LIQUID LAYERS WITH SODIUM CHLORIDE AND OTHER SALTS”. In: *The Journal of General Physiology* 12.1 (Sept. 1928), p. 1. DOI: 10.1085/JGP.12.1.1. URL: /pmc/articles/PMC2323696/?report=abstract%20https://www.ncbi.nlm.nih.gov/pmc/articles/PMC2323696/.

[44] Michihiro Miyake et al. “Phase transition of potassium sulfate, K2SO4 (III); thermodynamical and phenomenological study”. In: *Physics and Chemistry of Minerals* 7.5 (1981), pp. 211–215. DOI: 10.1007/BF00311891/METRICS. URL: https://link.springer.com/article/10.1007/BF00311891.

[45] D G M Powell et al. “Thermal Expansion and Other Properties of Sodium Chloride”. In: *Australian Journal of Physics* 18.3 (1965), pp. 205–218. DOI: 10.1071/PH650205. URL: https://www.publish.csiro.au/ph/ph650205.

[46] Samy Hocine et al. “Verification of selective laser melting heat source models with operando X-ray diffraction data”. In: *Additive Manufacturing* 37 (Jan. 2021). DOI: 10.1016/J.ADDMA.2020.101747.

[47] He Yang et al. “Hot Forming Characteristics of Magnesium Alloy AZ31 and Three-Dimensional FE Modeling and Simulation of the Hot Splitting Spinning Process”. In: *Magnesium Alloys - Design, Processing and Properties* (Jan. 2011). DOI: 10.5772/13778. URL: https://www.researchgate.net/publication/221910115_Hot_Forming_Characteristics_of_Magnesium_Alloy_AZ31_and_Three-Dimensional_FE_Modeling_and_Simulation_of_the_Hot_Splitting_Spinning_Process.

[48] Seyed Ataollah Naghavi et al. “On the Morphological Deviation in Additive Manufacturing of Porous Ti6Al4V Scaffold: A Design Consideration”. In: *Materials* 15.14 (July 2022). DOI: 10.3390/MA15144729. URL: https://www.researchgate.net/publication/361799109_On_the_Morphological_Deviation_in_Additive_Manufacturing_of_Porous_Ti6Al4V_Scaffold_A_Design_Consideration.

[49] V. Seyda et al. “Investigation of Aging Processes of Ti-6Al-4 V Powder Material in Laser Melting”. In: *Physics Procedia* 39 (Jan. 2012), pp. 425–431. DOI: 10.1016/J.PHPRO.2012.10.057.

[50] *Ti6Al4V Spherical Titanium Alloy Powder, Grade 5 - Heeger Materials*. URL: https://heegermaterials.com/spherical-powder/1300-ti6al4v-spherical-titanium-alloy-powder-grade-5.html.

[51] *Spherical TC4 Titanium-Based Powder (Ti-6Al-4V) | Stanford Advanced Materials*. URL: https://www.samaterials.com/3d-printing-powder/1904-spherical-tc4-titanium-alloy-powder.html.

[52] Mohammad Qasim Shaikh et al. “Supportless printing of lattice structures by metal fused filament fabrication (MF 3) of Ti-6Al-4V: design and analysis”. In: (). DOI: 10.1108/RPJ-01-2021-0015. URL: https://www.emerald.com/insight/1355-2546.htm.

[53] Paramjot Singh et al. “Additive manufacturing of Ti-6Al-4V alloy by metal fused filament fabrication (MF3): producing parts comparable to that of metal injection molding”. In: *Progress in Additive Manufacturing* 6.4 (Dec. 2021), pp. 593–606. DOI: 10.1007/S40964-021-00167-5/FIGURES/8. URL: https://link-springer-com.tudelft.idm.oclc.org/article/10.1007/s40964-021-00167-5.

[54] Kelc Robi et al. “The Physiology of Sports Injuries and Repair Processes”. In: *Current Issues in Sports and Exercise Medicine* (May 2013). DOI: 10.5772/54234. URL: https://www.researchgate.net/publication/241623404_The_Physiology_of_Sports_Injuries_and_Repair_Processes.

[55] Cathal O’Connell et al. “Characterizing Bioinks for Extrusion Bioprinting: Printability and Rheology”. In: *Methods in Molecular Biology* 2140 (2020), pp. 111–133. DOI: 10.1007/978-1-0716-0520-2{_}7/FIGURES/16. URL: https://link.springer.com/protocol/10.1007/978-1-0716-0520-2_7.

[56] Md Ahasan Habib et al. “Rheological analysis of bio-ink for 3D bio-printing processes”. In: *Journal of Manufacturing Processes* 76 (Apr. 2022), pp. 708–718. DOI: 10.1016/J.JMAPRO.2022.02.048.

[57] Dong Youn Shin et al. “Electrostatic-Force-Assisted Dispensing Printing to Construct High-Aspect-Ratio of 0.79 Electrodes on a Textured Surface with Improved Adhesion and Contact Resistivity”. In: *Scientific Reports 2015 5:1* 5.1 (Nov. 2015), pp. 1–7. DOI: 10.1038/SREP16704. URL: https://www-nature-com.tudelft.idm.oclc.org/articles/srep16704.

[58] Feng Zhang et al. “The recent development of vat photopolymerization: A review”. In: *Additive Manufacturing* 48 (Dec. 2021), p. 102423. DOI: 10.1016/J.ADDMA.2021.102423.

[59] McKenzie L. Coughlin et al. *Methyl cellulose solutions and gels: fibril formation and gelation properties*. Jan. 2021. DOI: 10.1016/j.progpolymsci.2020.101324.

[60] Prasansha Rastogi et al. “Review of alginate-based hydrogel bioprinting for application in tissue engineering”. In: *Biofabrication* 11.4 (Sept. 2019). DOI: 10.1088/1758-5090/ab331e.

[61] Sumesh P. Thampi et al. “Drying Drops of Colloidal Dispersions”. In: *https://doi-org.tudelft.idm.oclc.org/10.1146/annurev-chembioeng-101121-085056* 14 (June 2023), pp. 53–83. DOI: 10.1146/ANNUREV-CHEMBIOENG-101121-085056. URL: https://www-annualreviews-org.tudelft.idm.oclc.org/doi/abs/10.1146/annurev-chembioeng-101121-085056.

[62] Jungho Park et al. “Control of colloidal particle deposit patterns within picoliter droplets ejected by ink-jet printing”. In: *Langmuir* 22.8 (Apr. 2006), pp. 3506–3513. DOI: 10.1021/LA053450J/ASSET/IMAGES/LARGE/LA053450JF00007.JPEG. URL: https://pubs-acs-org.tudelft.idm.oclc.org/doi/full/10.1021/la053450j.

[63] Ying Song Yu et al. “Evaporative deposition of polystyrene microparticles on PDMS surface”. In: *Scientific Reports* 7.1 (Dec. 2017). DOI: 10.1038/S41598-017-14593-5.

[64] Wing Chung Liu et al. “Magnetically assisted drop-on-demand 3D printing of microstructured multimaterial composites”. In: *Nature Communications* 13.1 (Dec. 2022). DOI: 10.1038/s41467-022-32792-1.

[65] Wei Han et al. “Learning from “Coffee Rings”: Ordered Structures Enabled by Controlled Evaporative Self-Assembly”. In: *Angewandte Chemie International Edition* 51.7 (Feb. 2012), pp. 1534–1546. DOI: 10.1002/ANIE.201104454. URL: https://onlinelibrary-wiley-com.tudelft.idm.oclc.org/doi/full/10.1002/anie.201104454%20https://onlinelibrary-wiley-com.tudelft.idm.oclc.org/doi/abs/10.1002/anie.201104454%20https://onlinelibrary-wiley-com.tudelft.idm.oclc.org/doi/10.1002/anie.201104454.

[66] I. Poirier et al. “Saccharomyces cerevisiae viability is strongly dependant on rehydration kinetics and the temperature of dried cells”. In: *Journal of Applied Microbiology* 86.1 (Jan. 1999), pp. 87–92. DOI: 10.1046/J.1365-2672.1999.00638.X. URL: https://onlinelibrary-wiley-com.tudelft.idm.oclc.org/doi/full/10.1046/j.1365-2672.1999.00638.x%20https://onlinelibrary-wiley-com.tudelft.idm.oclc.org/doi/abs/10.1046/j.1365-2672.1999.00638.x%20https://ami-journals-onlinelibrary-wiley-com.tudelft.idm.oclc.org/doi/10.1046/j.1365-2672.1999.00638.x.

[67] *Ultimaker turns 10 - UltiMaker*. Date accessed: 07/08/2023. URL: https://ultimaker.com/learn/ultimaker-turns-10/.

[68] Thomas R Kramer et al. “The NIST RS274NGC Interpreter-Version 3 Disclaimer Acknowledgements”. In: (2000).

[69] K. Niespodziana et al. “Fabrication and properties of titanium-hydroxyapatite nanocomposites”. In: *Materials Chemistry and Physics* 123.1 (Sept. 2010), pp. 160–165. DOI: 10.1016/J.MATCHEMPHYS.2010.03.076. URL: https://www.researchgate.net/publication/229116286_Fabrication_and_properties_of_titanium-Hydroxyapatite_nanocomposites.

[70] Sujata Swain et al. “Comparative Study of Hydroxyapatite Synthesized by High Energy Ball Milling in Wet and Dry Conditions”. In: *Springer Proceedings in Materials* 13 (2021), pp. 195–202. DOI: 10.1007/978-981-16-3937-1{_}20/TABLES/1. URL: https://link-springer-com.tudelft.idm.oclc.org/chapter/10.1007/978-981-16-3937-1_20.

[71] Adelia Kashimbetova et al. “Pressure-less spark plasma sintering of 3D-plotted titanium porous structures”. In: *Journal of Materials Research and Technology* 22 (Jan. 2023), pp. 2147–2157. DOI: 10.1016/J.JMRT.2022.12.072.

A

Density Grading Through Design

A.1. Materials and methods

A.1.1. Scaffold design

Scaffold design for this research was done such that they'd be suitable for pressure driven extrusion-based 3D printing. A software package delivered with the printer named GeSiM Robotics (GeSiM Bio-instruments, Germany) was used to design the scaffolds. The shape of the scaffold was chosen to be cylindrical with a diameter of 10 mm and a height of almost 10.5 mm. Every layer was sliced such that it could be printed as 1 continuous line, the design linewidth was 410 µm and the line distance was between 200 µm to 400 µm. Every layer except the first was 328 µm thick for a total of 32 layers, the first one was approximately 280 µm thick to ensure good adhesion. Neither layer height nor line distance were chosen arbitrary, these were chosen such as to fall into a range favourable for bone in-growth [18]. For this pores needed to be bigger than 100 µm, but preferably >300 µm.

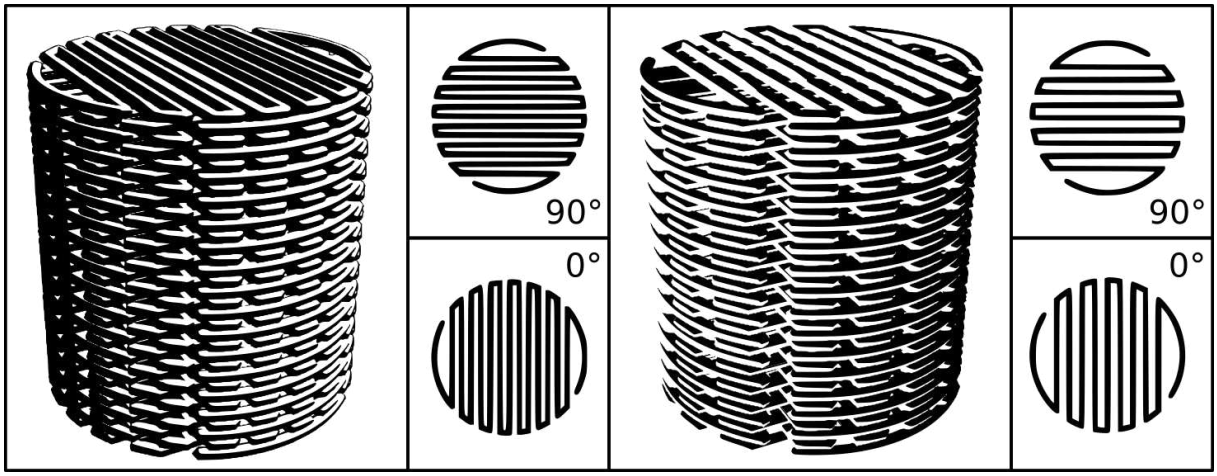

Figure A.1: Ungraded designs with 200 µm (left) and 400 µm (right) strut spacing.

Overall there were three geometrically unique designs. The first two (Figure A.1) were the simplest and had a constant line distance and a 90 degree angle shift between layers. One had a (inter) line distance of 200 µm the other 400 µm. The last of these three designs introduced engineered porosity and had a line distance that varied linearly from 200 µm in the first layer, to 400 µm, i.e., a 6.5 µm increase per layer. Cross sections of all 32 layers for this design can be seen in Figure A.2. There were also multimaterial scaffolds but their design was the same as the 400 µm design mentioned earlier, with the exception that from the 17^{th} layer onward the material changes to the second mixture.

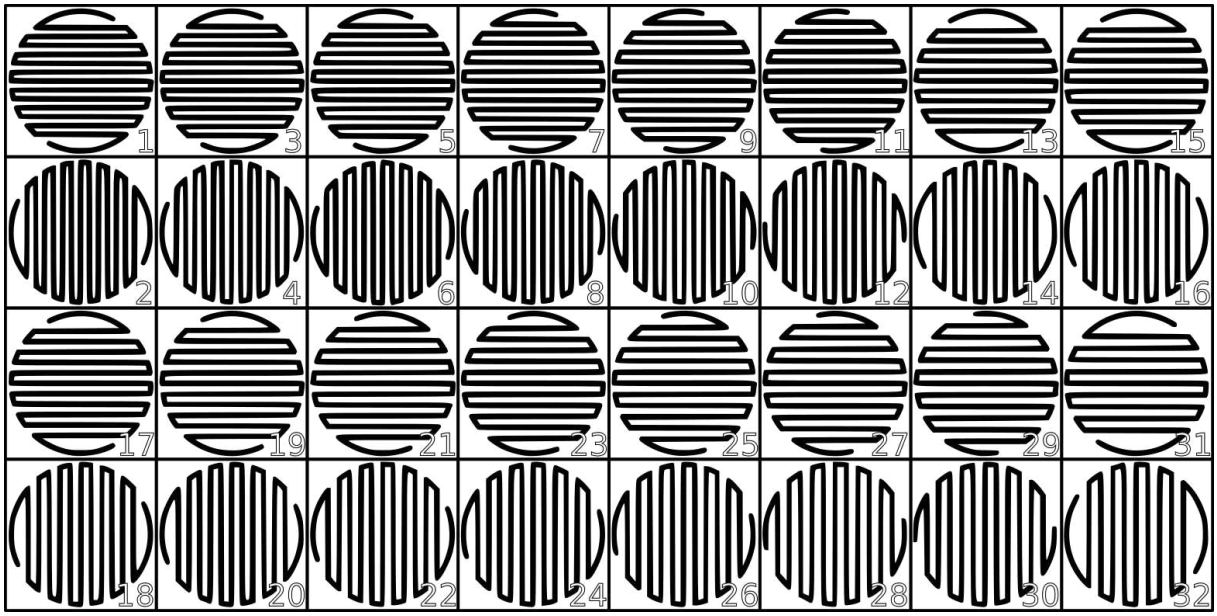

Figure A.2: Density grading with line distance from $200\,\mu m$ (layer 1) to $400\,\mu m$ (layer 32).

A.2. Results

A.2.1. Porosity of the scaffolds

Porosity results are summarized in Table A.1. The average measured porosity was higher than the design porosity due to the partial sintering, with the exception of the 200-400 graded samples which were not more porous than their design porosity. From the apparent density of Ti6Al4V powders which is between 2.2 and $2.8\,g\,cm^{-3}$ [48, 49, 50, 51] the initial[1] void volume percentage is between 50 and 37%. During sintering, densification takes places, and this pore volume is reduced, but if the sintering time is short and/or the temperature is low some of this porosity remains. The partial sintering can increase the porosity according to Equation A.1. In which ΔV_{por} is the change in pore volume because of porous struts in cm^3, V_s the volume of the structure in cm^3 and $\%_{void}$ the percentage of the structure that consists of voids.

$$\Delta V_{por} = V_s \cdot \%_{void} \tag{A.1}$$

Table A.1: Calculated connected porosity for partially sintered Ti6Al4V scaffolds

Sample group	m_{air} (g)	m_{sat} (g)	m_{sub} (g)	Porosity (%)
SP200 sample #6	**1.33**	**1.74**	**1.12**	**56**
SP200 sample #7	**1.28**	**1.68**	**1.11**	**61**
SP200 sample #8	**1.29**	**1.71**	**1.13**	**62**
SP200 average	**-**	**-**	**-**	**60 $\pm$6**
SP200 design	**-**	**-**	**-**	**47**
SP400 sample #6	**0.99**	**1.48**	**0.89**	**72**
SP400 sample #7	**0.93**	**1.41**	**0.82**	**71**
SP400 sample #8	**0.98**	**1.45**	**0.85**	**67**
SP400 average	**-**	**-**	**-**	**70 $\pm$5**
SP400 design	**-**	**-**	**-**	**60**
SP200-400 sample #6	**1.40**	**1.66**	**1.19**	**47**
SP200-400 sample #7	**1.37**	**1.63**	**1.16**	**48**
SP200-400 sample #8	**1.27**	**1.61**	**1.10**	**56**
SP200-400 average	**-**	**-**	**-**	**50 $\pm$10**
SP200-400 design	**-**	**-**	**-**	**54**

[1] Initial meaning before sintering.

A.3. Dimensional accuracy after sintering

The sintering process leads to densification and shrinkage. The dimensions changes after sintering are given in Table 4.1. A number of observations can be made. First, the bottom diameter after sintering remains bigger than the top diameter, the elephant foot that all samples have to some degree remains. Second, shrinkage isn't isotropic as shrinkage in height is not the same[2] as in diameter. Third, only partial sintering has occurred, shrinkage is lower than the 15% or higher shrinkage reported by others [52, 53] who have used higher temperatures, longer sintering times and low vacuum conditions[3]. Finally, the shrinkage of the density graded SP200-400 scaffold was greater than the SP200 and SP400 scaffolds, despite equal sintering settings[4].

Table A.2: Print geometry of Ti6Al4V scaffolds after sintering compared to the design specification

Sample group	Scaffold Height (mm)	Shrinkage (%)	Top diameter (mm)	Shrinkage (%)	Bottom diameter (mm)	Shrinkage (%)
Design	**10.50**	**-**	**10.00**	**-**	**10.00**	**-**
SP200	**10.38 ± 0.21**	**1.1**	**9.60 ± 0.51**	**4.0**	**9.70 ± 0.45**	**3.0**
SP400	**10.36 ± 0.31**	**1.3**	**9.55 ± 0.62**	**4.5**	**9.74 ± 0.51**	**2.6**
SP200-400	**9.80 ± 0.53**	**6.7**	**9.15 ± 0.34**	**8.5**	**9.36 ± 0.34**	**6.4**

Dimensional accuracy of Ti6Al4V + akermanite

Scaffolds containing akermanite were exposed to sintering temperatures for a longer time, the results of this can be seen in Table A.3. Despite the three times longer sintering time there is only $5\,\%$ to $7\,\%$ shrinkage in Ti6Al4V + akermanite composite scaffolds. The multimaterial scaffold shows a large amount of shrinkage, yet only on the side consisting of only Ti6Al4V.

Table A.3: Print geometry of Ti6Al4V + akermanite scaffolds after sintering compared to the design specification

Sample group	Scaffold Height (mm)	Shrinkage (%)	Top diameter (mm)	Shrinkage (%)	Bottom diameter (mm)	Shrinkage (%)
Design	**10.50**	**-**	**10.00**	**-**	**10.00**	**-**
SP200	**9.95 ± 0.11**	**5.2**	**9.31 ± 0.18**	**6.9**	**9.33 ± 0.34**	**6.7**
SP400	**9.99 ± 0.08**	**4.8**	**9.30 ± 0.26**	**7.0**	**9.40 ± 0.26**	**6.0**
Ti6Al4V + akermanite top SP00 Ti6Al4V bottom	**9.42 ± 0.06**	**10.3**	**9.45 ± 0.16**	**5.5**	**8.85 ± 0.22**	**11.5**

[2] Percentage wise

[3] The conditions used were $1250\,^{\circ}$C sintering temperature, 4 hour sintering time, and $20\,$Pa pressure.

[4] Though equal settings may not have given equal conditions.

A.3.1. Mechanical properties of the scaffolds

Ti6Al4V graded and ungraded scaffolds

In Figure A.3 the results of the mechanical compression test are displayed and Figure A.12 displays the corresponding scaffolds. Six samples for each design were compressed, three out of each sample sets. Figures A.3a through A.3c all have the same Y axis limits for clarity.

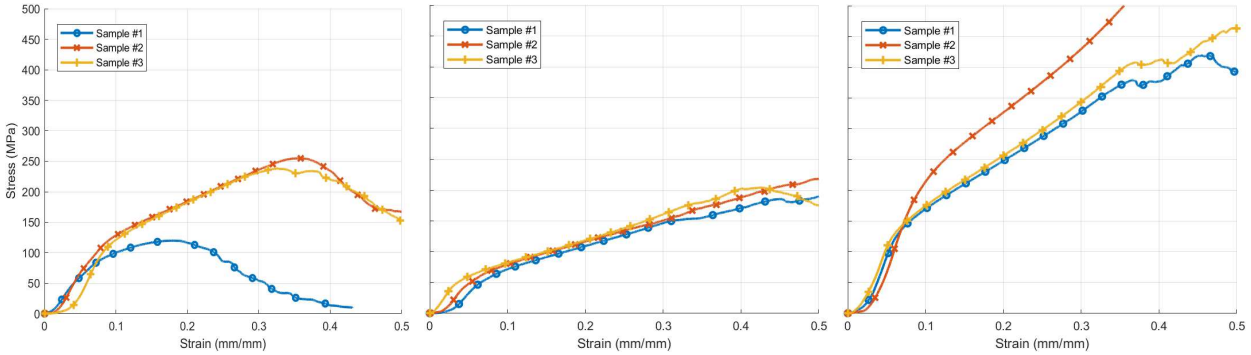

(a) 200 µm spacing **(b)** 400 µm spacing **(c)** 200-400 µm spacing

Figure A.3: Stress-strain curves for three designs made from Ti6Al4V alloy (first sample set)

Stress strain data obtained from the second second sample set, for which an alternate sintering approach was used to minimize batch to batch variation, can be seen in Figure A.4.

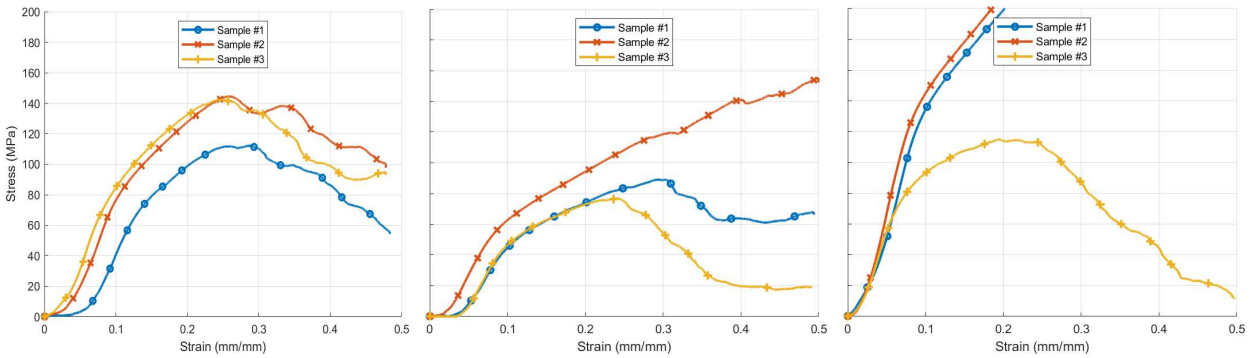

(a) 200 µm spacing **(b)** 400 µm spacing **(c)** 200-400 µm spacing

Figure A.4: Stress-strain curves for three designs made from Ti6Al4V alloy (second sample set)

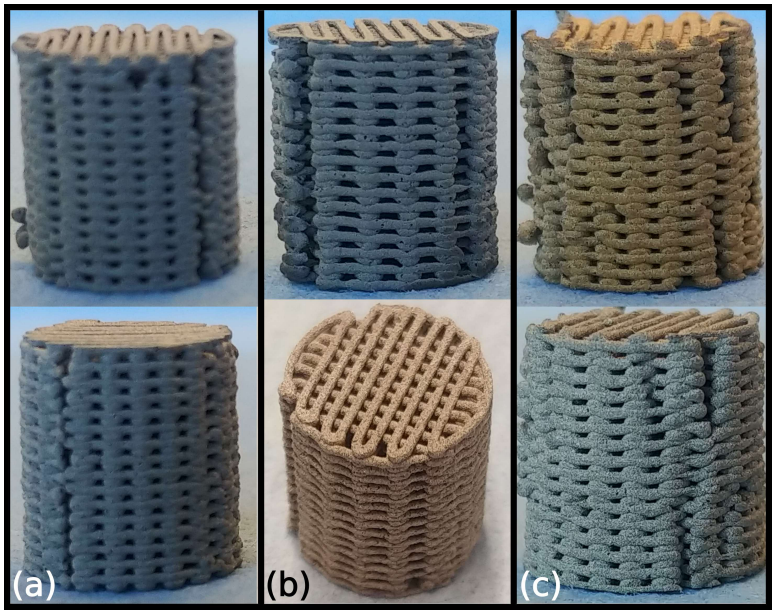

Figure A.5: The three different scaffold types (a) 200 µm spacing,(b) 400 µm spacing and 200-400 µm spacing (c)

At the start of the elastic region of the stress-strain curves there is a 'toe'[5] where the slope isn't constant. This toe region transitions to the linear region after a certain strain, but it isn't at the same strain for all scaffolds. This can be seen in Figure A.6 where the toe region is displayed in greater detail. For example, the stress-strain curve for sample #3, the linear slope almost intersects the origin, while for sample #1 it only starts at approximately 4% strain. This shape isn't uncommon in stress-strain graphs, the cause may be the uneven top of the scaffold deforming.

[5]This is a term to describe this form in a stress-strain graph [54]

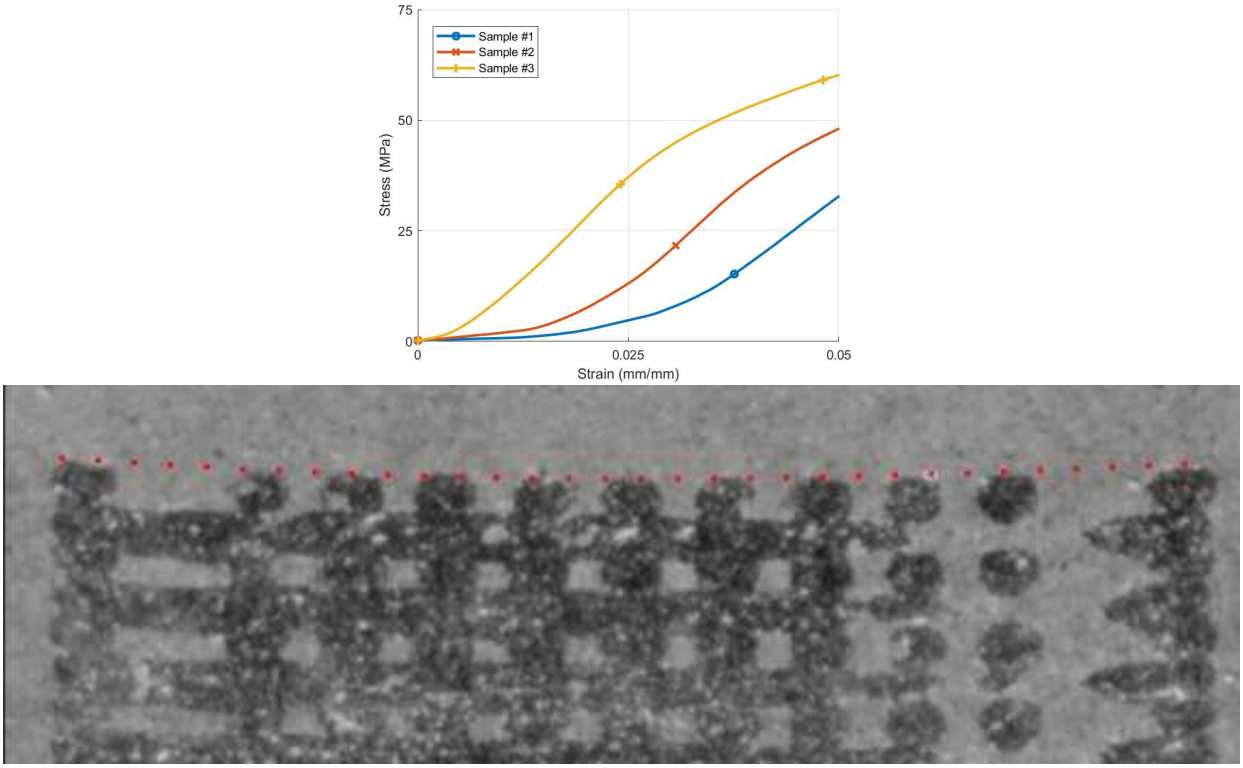

Figure A.6: Toe region of the 400 spacing stress-strain graph enlarged (top), and the slight concave shape at the top of some scaffolds captured from a cut and polished section, obtained via flatbed scanner. (bottom)

After this linear elastic region there is a plastic region with strain hardening. The yield strain was between 3% and 6%, which is significantly higher than fully dense Ti6Al4V obtained from literature. The (compressive) yield strain according to the ASM Atlas of Stress-Strain Curves [28] for a solid Ti6Al4V sheet in the aged condition is around 0.8%. The stress-strain relation for this solid sheet can be seen in Figure A.3.1, note the high strength of the dense Ti6Al4V alloy. One conclusion which can be drawn from this comparisson is that the porous samples in this work can be strained more before yielding than sheet stock.

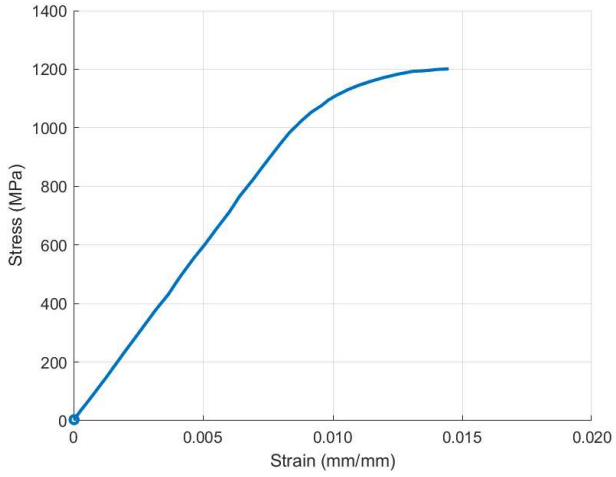

Figure A.7: Ti-6Al-4V aged titanium alloy sheet,compressive stress-strain curves at room and elevated temperatures redrawn from [28] [6]

There are two samples from the first sample set that are outliers from the rest, sample #1 of the 200 µm scaffolds, and sample #2 from the 200 µm to 400 µm scaffolds. The first appears to be a defective sample. While the samples used for mechanical tests were hand picked and didn't have externally visible defects there may have been internal defects. Defects such as voids, due to air bubbles in the ink or printing defects that are contained internally. The second outlier is stiffer and stronger than the other two, it was also approximately 10% heavier and came from a different printing session. Elastic modulus and yield stress results are displayed in Figure A.8.

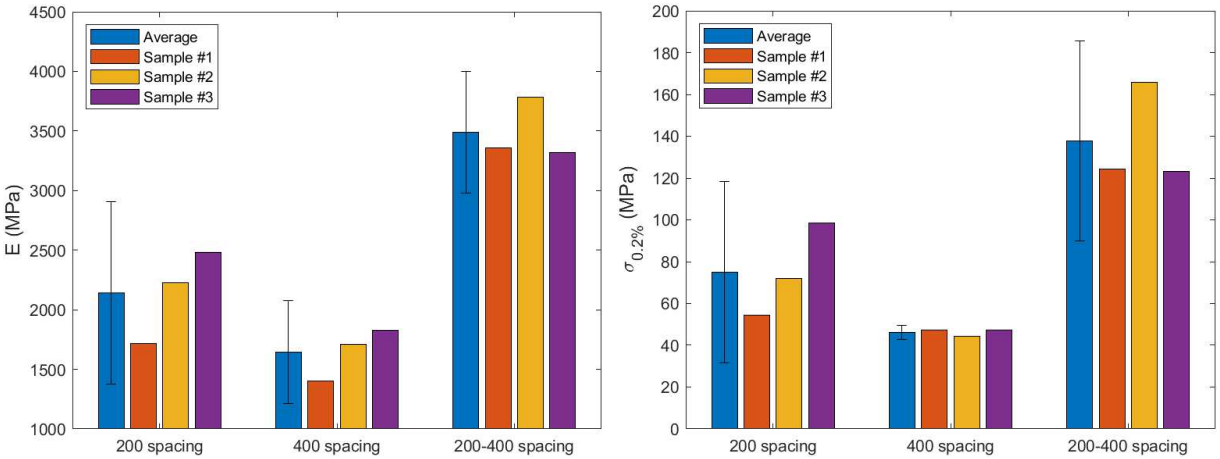

(a) Young's modulus (compressive)

(b) 0.2% yield strength

Figure A.8: Mechanical properties first sample set of Ti6Al4V scaffolds

From the results of the first set of samples what stands out is the high stiffness and strength of the graded scaffold. That is in disagreement with the hypothesis but it is too early to reject it just yet. Since there was a suspicion that sintering conditions could've played a substantial role, a doubt that would soon be taken away after testing the second sample set. Note that differences between SP200 and SP400 weren't quite significant (α = 0.05) for the Young's modulus (p = 0.13) nor the yield strength (p = 0.09).

Results for the second sample set follow the pattern seen in the first beat for beat. Concerns that sintering in batches were the only cause for the high stiffness in the graded scaffolds were therefore unfounded. Note that the 3rd sample of the 200-400 graded sample yielded early, which suggests this sample may have had internal defects. All differences in Young's modulus for this second sample set were significant, and the differences between 200SP and 200-400 graded, and between 400SP and graded were both highly significant (p $\approx$ 0.002). There was no significant difference in yield strength between the 200SP and 200-400 graded samples, but the presumed defective 3rd sample is to blame for this.

[6]Original source: "Summary of Mechanical and Physical Property Data Collected, Including Tensile Creep and Fatigue," Lockheed-Georgia, Dec 1962. As published in Aerospace Structural Metals Handbook, Vol 4, Code 3707, CINDAS/USAF CRDA Handbooks Operation, Purdue University, 1995, p 18

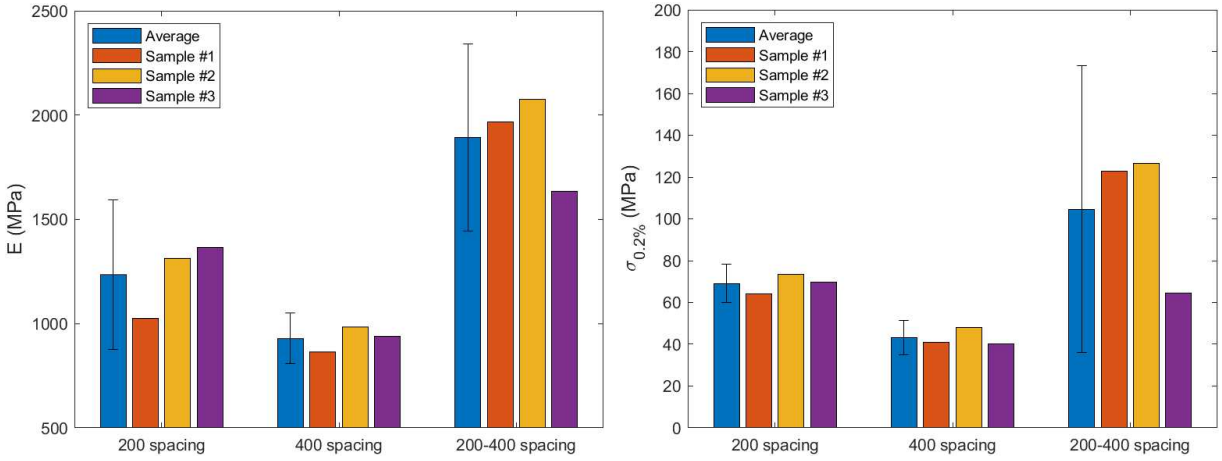

(a) Young's modulus (compressive)

(b) 0.2% yield strength

Figure A.9: Mechanical properties second sample set of Ti6Al4V scaffolds

Mechanical results normalized by mass

Across the two sample sets there was some variation in mass between groups. All samples printed together had a very minimal spread in weight. To give an idea of the spread the first set of 200 SP printed had an average mass of 1.32 g the second set had an average mass of 1.13 g, a 17% difference for the same geometry. The spread within a set was only up to 0.02 g sometimes as little as 0.001 g. Some of the contributing factors such as ink viscosity, air bubbles and extrusion pressure and perhaps others may have played a role. By normalizing the data we might be able to infer the impact of the geometry itself, rather than have differences obscured by this large spread between sets.

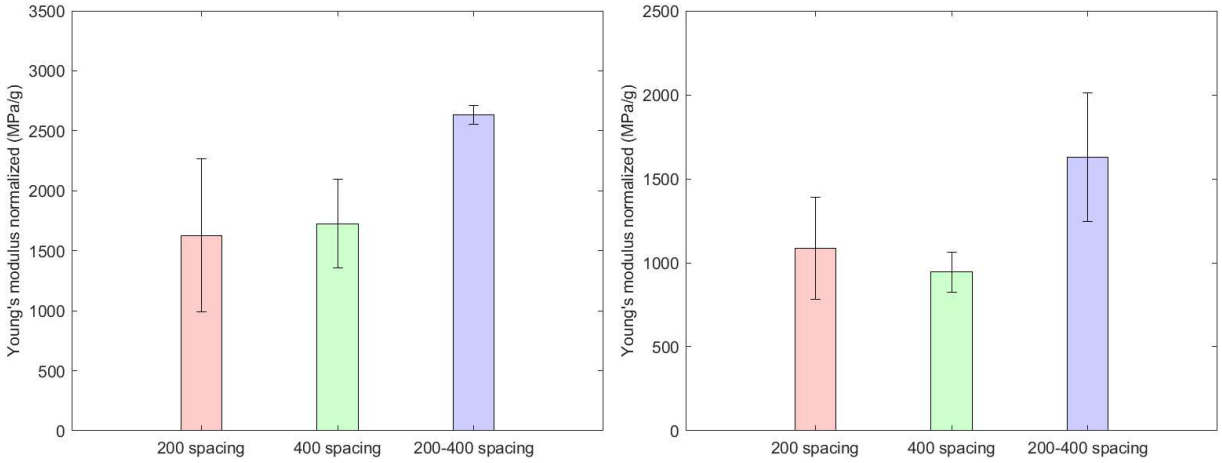

(a) First sample set

(b) Second sample set

Figure A.10: Young's modulus normalized

After normalization there is no significant difference between the 200 SP and 400 SP samples in either set. The graded scaffold, however, is significantly different. When the spacing is fixed the normalized stiffness is identical but when the spacing is varied this changes even after normalization. Also note that the scales are slightly different between sets.

Ti6Al4V and akermanite mixed and multimaterial scaffolds

Results of the mechanical tests can be seen in Figure A.11. Akermanite and Ti6Al4V composite scaffolds had an abrupt failure mode at a fairly low strain of 5%. Because the area under the stress-strain graph is a measure of absorbed energy, such a failure implies only a low amount of energy was absorbed before failure. Therefore, the scaffolds can be characterized as brittle. Akermanite is a ceramic and its addition

makes the scaffolds behave more like ceramics than metals.

While the single composite of Ti6Al4V and akermanite scaffolds had decreasing stress with increasing strain, the multimaterial scaffold (Figure A.11c) showed an increase. After approximately 20% strain the Ti6Al4V + akermanite composite, which made up half of the scaffold, began to compact. The second linear region that starts around 35% strain is a result of the pure Ti6Al4V side of the scaffold being compressed.

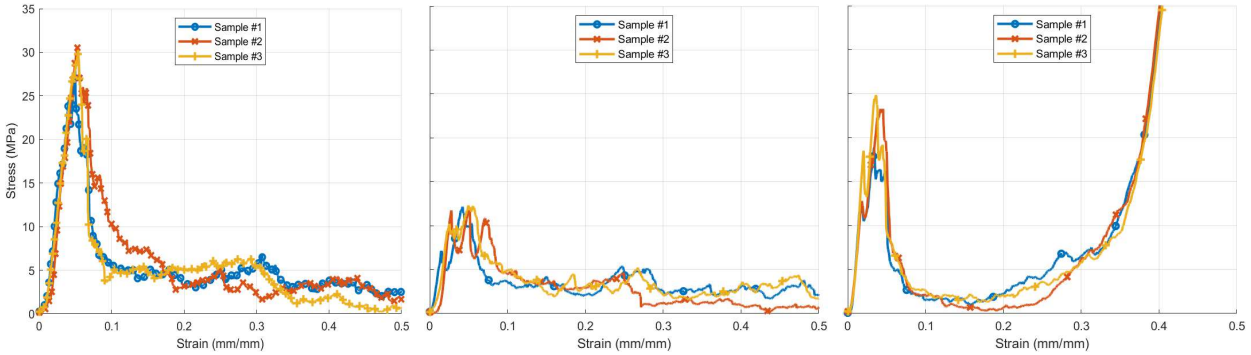

(a) 200 µm spacing **(b)** 400 µm spacing **(c)** 400 spacing multimaterial

Figure A.11: Stress-strain curves for three designs made from Ti6Al4V + akermanite composite

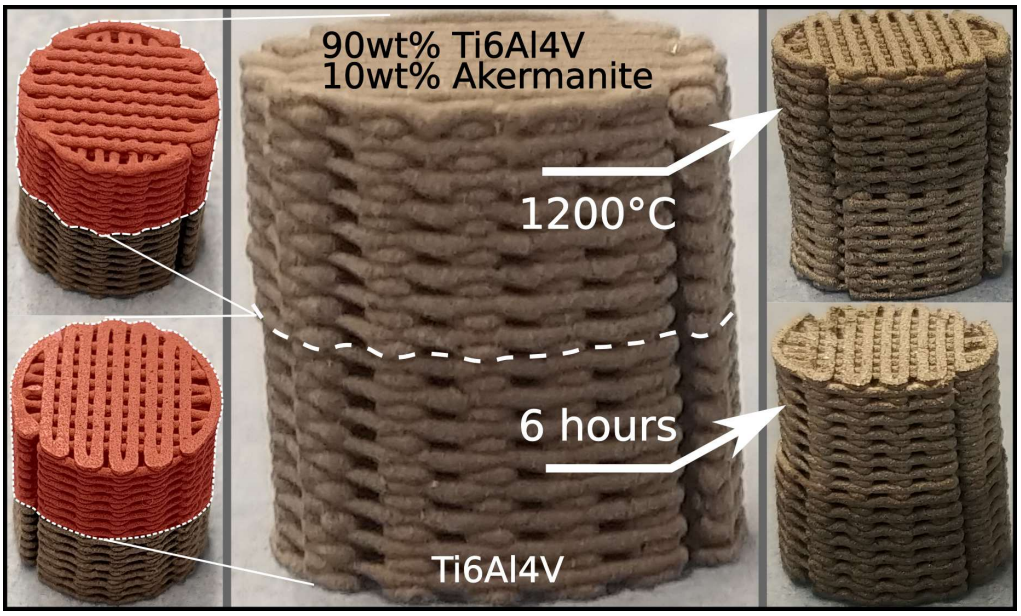

Figure A.12: Multimaterial scaffold of Ti6Al4V and Ti6Al4V + akermanite composite in unsintered (left and center) and sintered (right) states.

A summary of the elastic modulus and yield strength are given in Figure A.13. The two types of mixed composite scaffolds had comparable elastic modulus[7], but the 200 spacing case had a significantly higher yield strength ($p = 0.006$). Multimaterial scaffolds consisting of pure Ti6Al4V on the bottom and Ti6Al4V + akermanite composite on top were stiffer than either. This increase in stiffness did not come with a proportional increase in strength, and the multimaterial 400 spacing scaffold falls between mixed composite scaffolds, in that regard.

[7]The difference was insignificant with $p = 0.67$

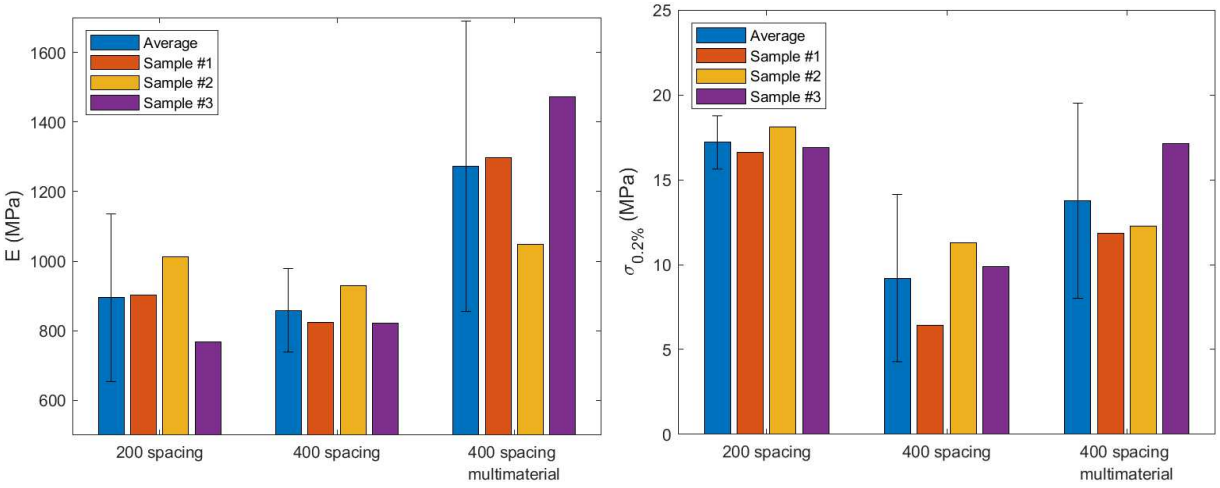

(a) Young's modulus (compressive) **(b)** 0.2% yield strength

Figure A.13: Mechanical properties of Ti6Al4V + akermanite scaffolds

Mechanical results normalized by mass

A.4. Mechanical test results

Result obtained by unconfined compression testing Ti6Al4V samples, indicated that increasing the spacing from 200 µm to 400 µm will somewhat decrease stiffness (23%) and moderately decrease strength (38%). The high stiffness and strength in the porosity graded 200 µm to 400 µm scaffolds, could not be explained. Normalizing the results by sample mass made it so that there was no significant difference between the two spacings.

Identically to the pure Ti6Al4V scaffolds discussed earlier, there was no significant difference in elastic modulus for the composite scaffolds. When the 200 and 400 µm results are normalized by mass the p values was 0.08. Not significant, but there might be a difference there.

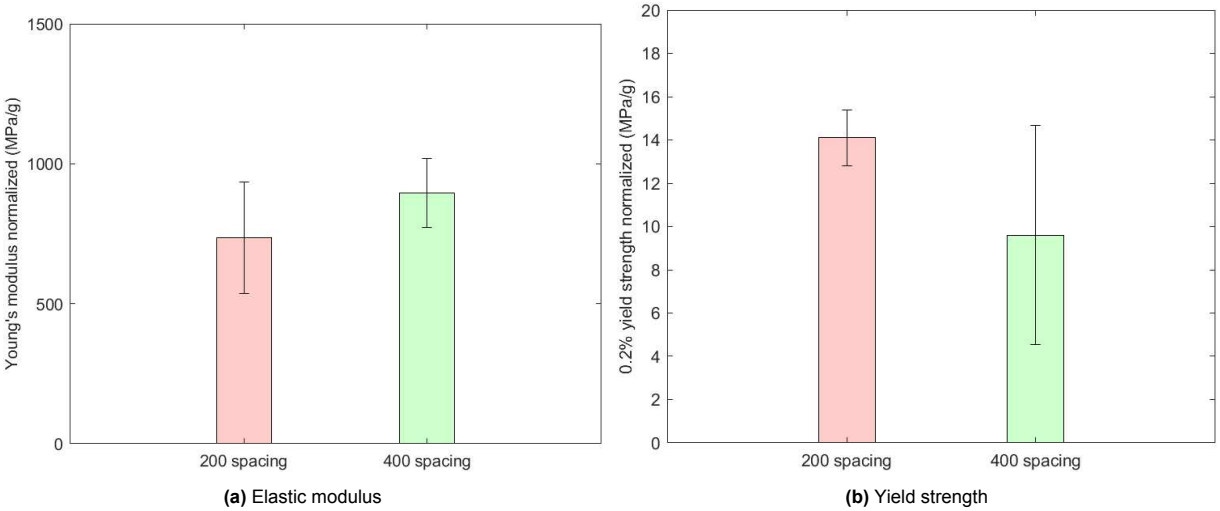

(a) Elastic modulus **(b)** Yield strength

Figure A.14: Mechanical properties of Ti6Al4V Akermanite composite scaffolds normalized

In terms of strength the 200 µm spacing scaffold is superior and this result was significant (p = 0.04).

The multimaterial scaffold, which has Ti6Al4V on one side and Ti6Al4V + akermanite composite on the other, had two slopes. For these results the first is taken. The second slope starts at around 40-50%

strain which is when the Ti6Al4V + akermanite composite has been crushed and compacted. What follows is a slope almost entirely from the Ti6Al4V side being compressed and we can give a rough estimate of 1600 MPa for that side. Roughly twice as high as the composite side.

A.5. SEM imaging

A.5.1. Strut width, strut spacing, defects and sagging

Manufacturing using extrusion based printing comes with differences and defects between the design input, and the part output. The pressure based extrusion printing used on the Gesim Bioscaffolder is sensitive to many error sources. Relatively little error is to be expected from positioning errors as the Bioscaffolder's following is constantly tracked with encoders and when a following error is detected the print is aborted. A much more significant and fundamental source of error comes from the flowrate. Using pressure driven extrusion has one unintended consequence; flowrate at any point in time depends on the ink rheology[8], all downstream conditions, and even the amount of ink left in the cartridge may play a role. The top view of the struts can be seen in Figure A.15.

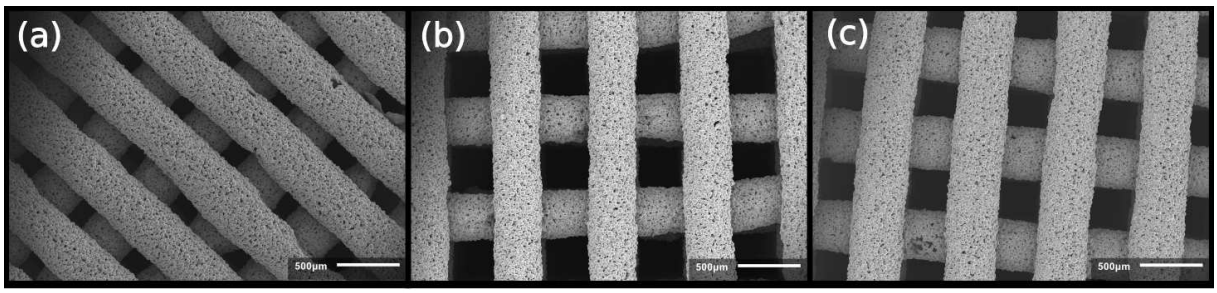

Figure A.15: Strut geometry of (a) 200 µm spacing, (b) 400 µm spacing, and (c) 200-400 µm spacing scaffolds

Strut width depends on the nozzle size, and the flowrate. Struts can't be much smaller than the nozzle, for most inks, except the most stretchable inks. In general the struts simply tear if the flowrate is insufficient leading to intermittent printing. Strut spacing is compromised if struts are too thick, the thicker strut will take up part of the spacing between adjacent struts. Strut width and strut spacing was obtained from SEM images, a summary is given in Table A.4.

Table A.4: Print geometry of Ti6Al4V scaffolds after sintering compared to the design specification

Sample group	Strut width (µm)	Strut spacing (µm)	Strut height (µm)	Pore height (µm)
SP200 Design	**410**	**200**	**328**	**328**
SP200 Sintered	**414.4 ± 25.3**	**169.2 ± 29.0**	**387.9 ± 26.8**	**215.2 ± 14.6**
SP400 Design	**410**	**400**	**328**	**328**
SP400 Sintered	**389.8 ± 20.8**	**384.3 ± 26.4**	**407.1 ± 20.2**	**229.8 ± 51.4**
SP200-400 Design	**410**	**200-400**	**328**	**328**
SP200-400 Sintered[9]	**426.6 ± 15.7**	**330.3 ± 16.3**	**394.1 ± 21.2**	**191.6 ± 19.5**

A.5.2. The effect of partial sintering

The holding time during sintering was kept relatively short (2 h at 1200 °C) in order to only partially sinter the structure to increase porosity and decrease stiffness. SEM images illustrate that this was successful. These images taken for the three different scaffolds[10] can be seen in Figure B.4.

[8] Ink rheology may not be the same throughout a batch of ink.

[9] Measurement taken at the top side where the design spacing is 400 µm

[10] All images were taken from the top surface. The sintering progress should be uniform throughout a scaffold as every part of it was under identical conditions during sintering.

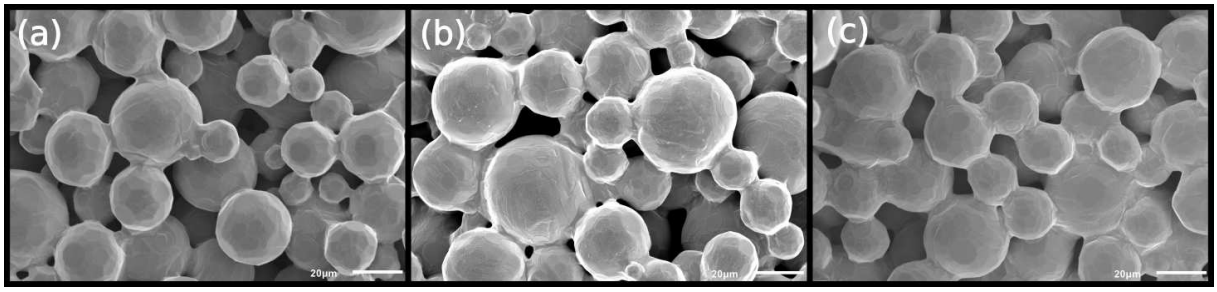

Figure A.16: Results of short sintering time on strut pore structure: (a) 200 µm spacing, (b) 400 µm spacing, and (c) 200-400 µm spacing scaffolds

A.6. Summary of results chapter

Normalizing for scaffold mass revealed that ungraded scaffolds have a strength that is closely related to their mass. After normalization there was no longer a significant difference between 200 µm and 400 µm spaced scaffolds.

Despite normalization the graded scaffolds were always significantly stiffer while we've been unable to explain this it leads us to conclude that the graded scaffold design is perhaps simply stiffer and stronger under compressive loading. FEM modeling could be used to prove or disprove this hypothesis.

B

Enhanced Direct Ink Writing Using Metastable Ink

B.1. Introduction - Printability criteria for non bioinks, a dissenting view

In DIW the rheological properties of the ink play an important role, whether these are bioinks [55, 56] or particulate inks. One property in particular is often described as a necessity, namely, shear thinning. Shear thinning fluids exhibit decreasing viscosity with increasing shear-rate. This behaviour is considered ideal for DIW because the viscosity drops when the fluid moves through the nozzle (Point A in Figure B.1). Additionally, after exiting the nozzle the fluid viscosity increases as the fluid is no longer sheared (Point B in Figure B.1). The extruded fluid is thus able to better maintain it's form and prevent collapse of the structure (Point C in Figure B.1). While this is an important property, there are many others that make or break a certain ink for a certain application.

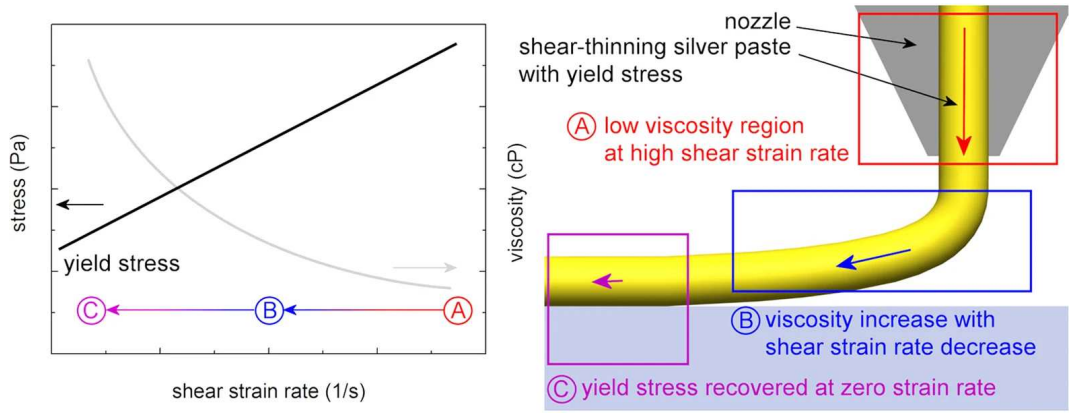

Figure B.1: The behaviour of a shear thinning liquid at three stages of extrusion reproduced from [57]

Examples of other critical properties are: viscosity magnitude, yield stress of the solution, and viscoelasticity. While nozzle geometry (size and shape) plays an important role in the pressure flow relation, so does ink viscosity. If either of these parameters restricts the flow too much printing is either not possible or flowrate limited and thus slow. The yield stress under tension determines if overhangs can be printed, the yield stress under compression on the other hand relates to the self-supportability. Finally, viscoelastic properties influence sagging and creeping of the ink after extrusion.

Another process by which some inks maintain their form after extrusion is cross linking of which gelation is one example. In cross linking, polymers are solvated in a solution, but upon a trigger they will start to crosslink or gel. The crosslinking process connects the polymers together into polymeric networks greatly increasing mechanical properties of the solution. The trigger event depends on the type of polymer it can

be photons, heat or a chemical. Some examples are : photopolymeric resins setting after exposure to light [58], methyl cellulose gelling above it's gelation temperature [59] and gelatin below; and sodium alginate crosslinking by calcium ions [60]. These reactions are often irreversible, however, in the case of methyl cellulose and gelatin the gelation can be reversed by changing the temperature.

A far less common approach to stabilizing extruded liquids is through desiccation, otherwise known as evaporative deposition[1][61]. Desiccation is the process of drying in other words removing a liquid component. Usually, desiccation refers to water but for our discussion it can be other liquids/solvents as well. The process uses a liquid with suspended particles, and has been used in inkjet printing [62] to control droplet morphology, to apply monolayer surface coatings [63], to manufacture multimaterial nacre like structures [64], and to create nanoscale structures using self assembly [65]. Upon drying, the particles are forced to settle into a thin layer, the phases of this process can be seen in Figure B.2. A significant portion of research related to this technique is on suppressing the coffee ring effect, but for the application in DIW this did not prove to be a relevant issue. While others have made use of this process, across multiple disciplines nonetheless, it has, to the best of our knowledge never been applied to DIW.

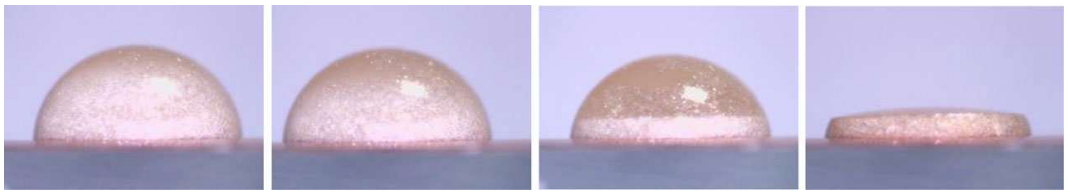

Figure B.2: The states of deposition and desiccation of a low viscosity suspension. From left to right deposition, settling, evaporation and desolvated. adapted from [64]

Ink formulations which behave this way are unlike the ones described prior. There is no cross linking and shear thinning is not required, if anything it might even be somewhat detrimental[2]. Still desiccation is closer to cross linking in the sense that it is a mostly irreversible process, during which, the mechanical properties greatly increase. Another thing to consider is that this technique is unlikely to be suitable for inks containing cells (bioinks). These cells have poor viability when dehydrated by means other than spray or freeze drying [66]. Regardless of whether they'd remain viable, cells will not survive high temperature post processing steps required for metals and ceramics, when these are applied globally[3].

The combination of evaporative deposition and DIW can be used to significantly increase the process resolution in the build direction. The ability to create very thin layers is not the only benefit though. Inclusions of air into the ink are virtually eliminated because of buoyancy of air and the low viscosity nature of the ink. Air is not only eliminated in the ink itself though, but also between layers. The deposition lines have a rectangular shape, instead of circular like the nozzle. Additionally, shear stresses applied by the nozzle are lower and propagate less. Ultimately, these stresses remain dependant on the viscosity, which has to be high enough to keep the ink mixture from separating. The yield stress at tearing is very low, and while this is beneficial in preventing tear-off artifacts it makes steep overhangs unprintable. However, increased resolution[4] makes gradual overhangs easier to print as the overhang per layer gets reduced. Despite it's flaws incorporation of evaporative deposition offers the promise of higher resolution DIW with fewer artifacts.

B.2. Methods and materials

Due to limited interest and limited time in depth characterization of the scaffolds was not performed. However, some photographs, SEM images and weighing has been performed and is available in the results section. In this section the designs, printing procedure are described.

[1] Not to be confused with thermal evaporation

[2] A slight ability to flow after the shear rate drops could help fill voids.

[3] Meaning if applied to the scaffold as a whole by means of a sintering furnace.

[4] In the build direction.

B.2.1. Scaffold design

A number of designs were made in Cura (Ultimaker BV, the Netherlands) to showcase the capabilities of extrusion-based 3D printing with low viscosity metastable ink. Particularly, in an application where it shines, namely, organic shapes. Again these designs were cylindrical but the infill pattern was a triply periodic minimal surface (TPMS) structure called gyroid. The organic shapes had very gradual overhangs making them easily printable without support material. The used linewidth was 200 µm, the layer thickness 40 µm and the line distance 1400 µm.

Another design with the 'line' type infill [5] with a linespacing of 600 µm and again a linewidth of 200 µm. Note that this design has significantly higher porosity than the regular SI400 spacing. Not only is the line spacing increased but the strut width is also decreased. The extremely thin layers make the struts rectangular instead of cylindrical. The theoretical porosity for the SI400 spacing SI410 strut diameter original design was 60.7%. While that of SI600 spacing SI200 strut width is 75%.

B.2.2. Cura interpretter for Gesim

The software that came with the printer was inadequate for making this advanced scaffolds. A more modern slicer, such as Cura or Prusaslicer was needed. The decision was made to use the former to aid gcode generation for the gyroid and 600 µm spacing scaffolds. Considering the layer height was reduced by a factor of 8 from 328 µm to 40 µm, manually creating gcode and sequences for the 600 µm spacing scaffold was considered not practically feasible[6]. The Cura slicer has been under constant development for almost a decade [67], it has the ability to slice complicated STL files and has many advanced features, which are not available in Gesim Robotics.

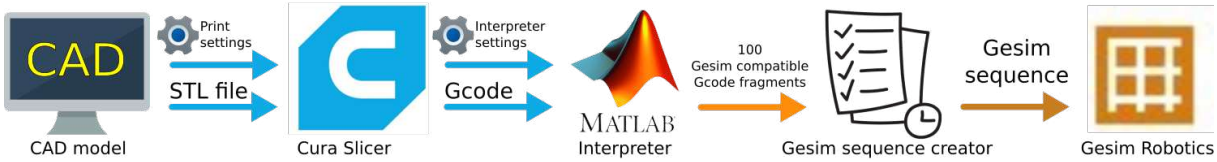

Figure B.3: Preparatory steps from CAD model to executable Gesim sequence. Icons obtained from Cura, Matlab and Gesim. Other graphics from Wikimedia commons : computer (paomedia), gear (Microsoft Corporation), checklist (Mam'Gobozi Design Factory)

The Gesim Bioscaffolder only accepts it's own flavour of gcode, but there are a great number of similarities with NIST's RS274 [68], which is the defacto standard most modern Gcode is based on. For different computer numerical control (CNC) applications additional gcode commands have to be implemented. For this reason there are many different implementations based on RS274, all different and all gcode processor dependent. Cura can export gcode in a variety of 'flavours' though none of them are compatible with the Gesim. In order to translate Cura's output to Gesim compatible gcode an interpreter was written in Matlab (The MathWorks Inc.,Natick, Massachusetts, United States). Besides providing the correct syntax it also implements material retraction emulation [7]; automated tip wetting, wiping and drying; and large gcode file support[8].

B.2.3. Ink preparation

The metastable ink of high fluidity was prepared a little different from the viscous ink discussed earlier. This new ink has a low viscosity and low metal loading, and was explicitly formulated to have a volume shrinkage of 80%. The binder type[9] and amount water can be chosen such that binder loading for both stable and unstable inks is equal after drying. For the sake of consistency only one type of HPMC was used therefore it was not possible to keep the binder loading equal. Equal binder loading would guarantees nearly equal and sufficient green strength for both inks, however, because this loading wasn't equal the metastable ink counter intuitively had more binder. Hardware limitations of the printer's proportional valve

[5] Similar to has been done in the main thesis.

[6] The required sequences would have in excess of 2300 steps.

[7] Flow and oozing is arrested by means of cutting the driving pressure.

[8] Gcode files bigger than 50,000 lines couldn't be executed, a workaround was created with which files up to 3,000,000 lines can be used.

[9] The viscosity grade of methylcellulose which is related to the molecular weight.

were such that the extruder pressure could not be set below 10 kPa. This presented no issue for the stable ink with a measured viscosity of over 200 Pa s whereas for the metastable ink it did. High fluidity and high extruder pressure leads to a great shear rate and high flow. Stable and metastable ink used binders with concentrations of 5.5w% and 2.8w%, respectively. The MC/HPMC viscosity as a function of temperature is very non linear at these high concentrations.

Preparation of the ink was similar the only major differences are that the quantities are changed and additional water is added. To make the ink 7.7 g:3.72 g:3.64 g of Ti6Al4V powder, binder, and water, respectively, were added to a glass vial. The contents were mixed to combine the water with the binder, and it was stored until printing.

B.2.4. Printing with the metastable ink

Printing with the metastable ink and using the Cura to Gesim interpreter was slightly different from what was discussed in the mainmater of this thesis. The ink preparation was performed in a bottle, and ink was only stirred and transferred into the syringe barrel at the printer, just before printing. This was done to stir up titanium particles and delay settling out. Additionally, in order to have enough flow control despite the Gesim Bioscaffolder's high minimal pressure (10 kPa) large conical nozzles did not provide enough back-pressure. And instead, a 200 µm cylindrical nozzle[10] was used with the cylindrical section being approximately 10 mm long. The print speed was also significantly higher (20 mm s^{-1}), but because of the reduced layer height (down from 328 µm to 40 µm) this did not result in a reduction in print times. A slight increase in print times resulted. Preparing for the printing is more straightforward as manual creation of the gcode files is cut back to creating one gcode file through Cura. The interpreter handles all the processing and outputs 100 Gesim compatible files. A universal sequence to run these files, in order, only needed to be created once.

B.2.5. Instability and agitation

In order to understand why there would be any benefits at all compared to more orthodox formulations, a comparison is in order. In a regular ink, particle loading is often maximized the idea being that insufficient loading will result in structures with a lot of (unintended) porosity. However, as material is added a tipping point is reached where the behaviour changes from a free flowing suspension to a immovable paste. And, while the specific point isn't set in stone it can not be avoided. Generally the solid volume fraction at which point this happens is between 40 % to 60 %[11]. So despite a best effort approach a large amount of the ink is undesirable filler. While there is no way of maintaining a free flowing liquid at too high volumetric loading, doing so at low volumetric loading is easy. By evaporating the carrier liquid layers with lower porosity can be made.

The metastable ink was sufficiently stable to finish printing, before settling out noticeably interfered with the printing process. It is hardly surprising that adding another input variable (ink viscosity) to the printing process can lead to a more optimal outcome (larger solution space). In fact in control system design, system performance can often be increased by putting the system in an inherently unstable state and stabilizing it with a control mechanism. In this case stabilizing the system is as simple as agitating the ink.

Agitation is complicated slightly because the container with the ink is sealed and pressurized. Feeding through mechanical agitation is therefore difficult as it might break the containment of the pressurized gas. Two types of magnetic feedthrough (with permanent magnets and electromagnets) offered a solution. Inside the pressurized tube was a stir element (similar to a magnetic stirbar) and on the outside were either permanent magnets that were moving or electromagnets that were turned on and off in order to spin the stir element. Magnetic coupling can deliver only a limited amount of torque and it was noted that permanent magnets were superior in this regard, on the other hand the electromagnets could reach higher stirring speeds. Since the aim is to stir a liquid that itself isn't very viscous the approach using electromagnets was developed further.

[10] An added benefit of this is that X and Y resolution doubled and nozzle area was reduced by a factor of 4.2.

[11] Anecdote from personal experiences.

B.3. Results

While this results section is limited to optical and electron microscope images they still manage to shine some light on some of the most notable differences. In a sense producing a part with this liquid ink is like applying paint, every layer has to dry before the next one is applied. As a result voids in the layer below are often filled in. Optically this makes the layer lines disappear, and perhaps the entire structure becomes more isotropic.

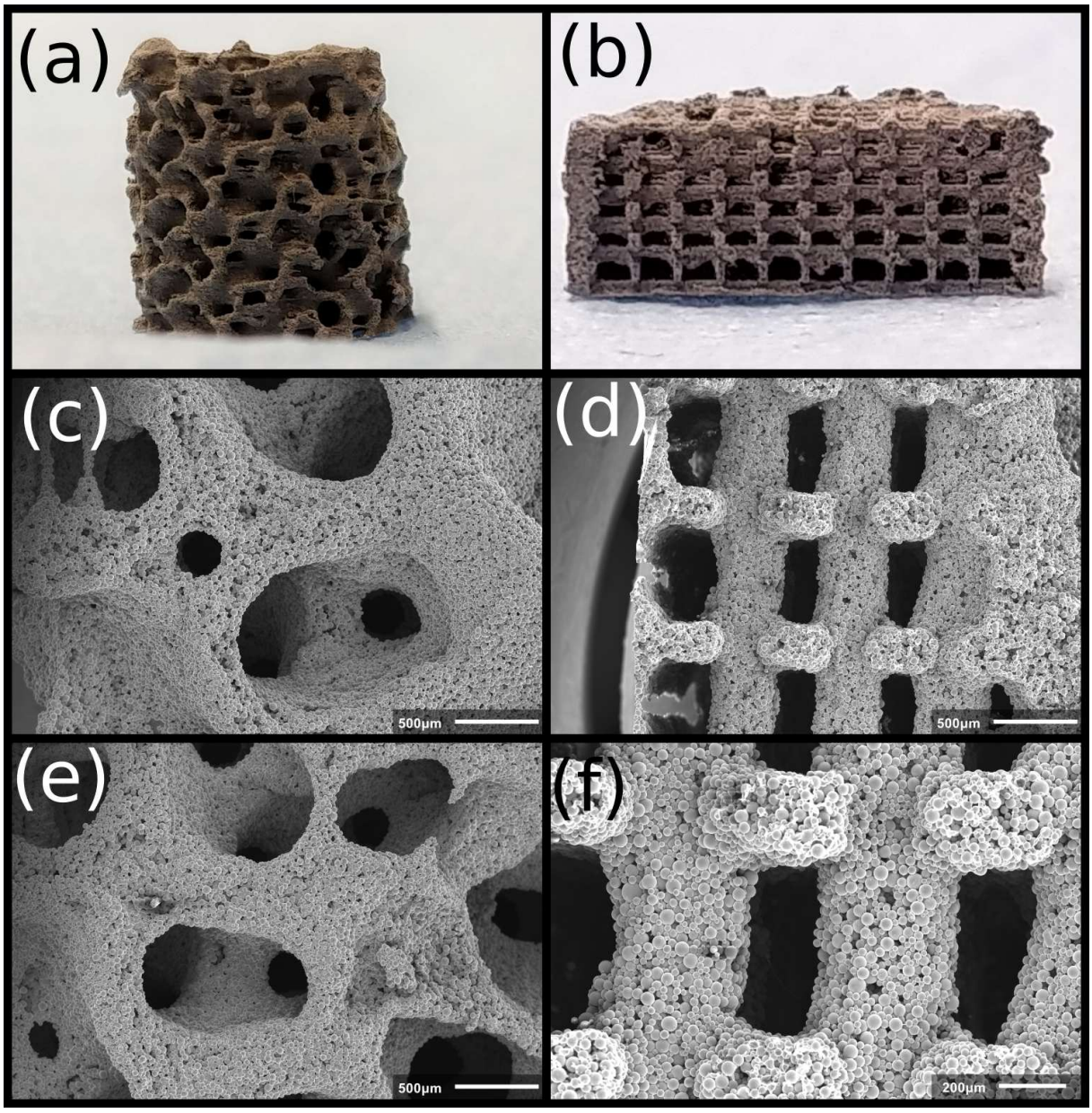

Figure B.4: Results of metastable ink writing: (a) A printed gyroid type strucutre, (b) a printed rectilinear structure with $600\,\mu m$ linewidth and $200\,\mu m$ struts, (c) unsintered gyroid, (d) rectilinear structure under SEM, (e) gyroid sintered, (f) rectilinear structure increased magnification.
In all SEM images the print direction was from left to right. Note in the rectilinear pattern that each strut was made up of multiple layers.

C

Appendix - Ti6Al4V and Nano Hydroxyapatite Scaffolds

C.1. Introduction

Hydroxyapatite (HA) is a calcium phosphate based bioceramic that is very similar to skeletal apatite. In the body these crystals are loaded onto the collagen fibrils that make up human bone. In order to increase the ability for bone to grow on scaffolds an attempt was made to include this mineral in the ink. The while the combination of Ti6Al4V and nano hydroxyapatite wouldn't sinter under any of the used preperation methods and sintering regimes in this chapter a write-up is given of what has unfolded.

C.2. Methods and materials

In the titanium only ink described previously, approximately 4.83 mL of the total volume (9.27 mL) is titanium. This volume fraction was kept constant in inks in which HA partially substituted Ti. Calculating the masses for any ratio of Ti to HA for a predetermined volume can be done using the following formula:

$$V_s = \frac{m_s w\%_A}{\rho_A} + \frac{m_s w\%_B}{\rho_B} \tag{C.1}$$

Where V_s is the volume of the solids, w% the weight percentage of component A or B and ρ the density of component A or B and m_s the solid mass. An example calculation with (V s=4.83, w%A =0.95, w%B =0.05, ρA =4.43 , ρB =3.05) yields:

$$4.83 = m_s(\frac{0.95}{4.43} + \frac{0.05}{3.05}) \rightarrow m_s = 20.92 \tag{C.2}$$

Two HA/titanium ink synthesis routes were attempted, one based on mechanical alloying [69], the other on wet ball milling [70]. The former resulted in barely printable ink due to HA nano powder agglomerations, with very limited sintering performance. In the SEM results (Section **??**) this is elaborated upon. For this reason an alternative approach was taken for the later. The w% of HA was 10% for both. The second synthesis route aimed to mitigate shortcoming, such as the clogging due to agglomerations and the lack of sintering. By adding a liquid component during milling agglomerations were prevented, and virgin Ti6Al4V powder was added after wet ball milling to aid sintering. The sintering results for this mixture were, regrettably, very similar to the first mixture. Though the dispersion as can be seen in the SEM results of the nano hydroxyapatite was significanlty better than for mechanical alloying.

Ti6Al4V and hydroxyapatite ink prepared via mechanical alloying

Nano hydroxyapatite powder was obtained from (Sigma Aldrich, Germany) and was used without further purification. It had a specified particle size <200 nm, however, it had agglomerated into lumps. To break these up, and distribute the HA evenly a technique named mechanical alloying was used. Mechanical alloying was done using a tumbler mill (*brand and model*), glass container, steel milling media and the powder mixture.

The 50 mL container contained roughly 20% milling media and 14% powder (27 g Ti6Al4V and 3 g of HA) by volume, though the apparent volume of the powder was significantly greater than 14%. The apparent volume was observed to decrease as ball milling progressed.

Hydroxyapatite displayed a tendency to cold weld to the container. In order to maintain the correct ratio the HA was scraped off with a powder spatula, repeatedly. Each milling cycle lasted 24 hours and was followed by scraping, before transferring contents to a clean container. The procedure was repeated two more times after which no more cold welding was visible. The mechanical alloy of HA and Ti was mixed with binder and transferred into a 10 mL syringe barrel for printing.

Ti6Al4V and hydroxyapatite ink prepared via wet ball milling

Wet ball milling is a processes where the milling media and powder load are submerged in a liquid. In this synthesis it serves two purposes, first preventing cold welding to the container, and second limiting HA agglomeration. A 50 mL glass bottled was packed with a 50:50w% mixture (3 g of Ti6Al4V and 3 g of HA) in 10 mL of anhydrous ethanol. The milling media was added which consisted of 4 mm diameter steel (not stainless) balls. Wet ball milling was performed on this mixture for 24 h.

The content was poured out into a beaker, and the container was washed two times with distilled water in order to get all the product out. The volume was topped up to 200 mL with more distilled water. The main reason for this was to increase flash point for safety reasons, but also in order to remove all ethanol from the final product. The ethanol and nearly all of the water was then removed by means of heating. The mixture wasn't heated to dryness as this had been found to introduce lumps. Instead, it was boiled until approximately 2 g of water remained (3 g Ti6Al4V, 3 g HA, and 2 g water).

Because of the remaining water, no amount of the 5.5w% binder would give the same final concentration. To overcome this issue a higher concentration binder of 10w% was used. An addition of 2.45 g of 10w% binder gave the desired binder concentration of 5.5w%, as well as similar binder volume. Finally to this mixture 24 g of virgin Ti6Al4V powder was added to create a 90:10w% (Ti6Al4V:HA) loaded ink.

C.2.1. SEM and EDS

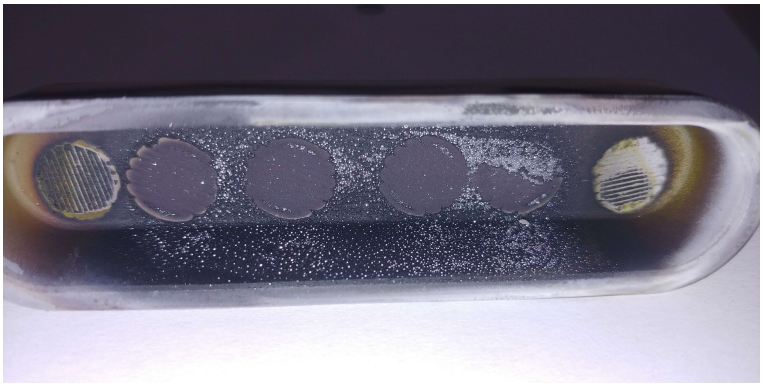

Figure C.1: Metallic residue found on the aluminia crucible after sintering mixtures of Ti6Al4V and HA.

Besides scaffolds, the residue found on the crucible wall[1] (Figure C.1) was also analyzed. Procedure for imagining the powder was very similar to the ones used for scaffolds. Powder was first pressed onto a conductive sticker with a clean nitrile glove. Then, compressed air was used from much closer to ensure there were no loose particles. The sputtering process was repeated without change. The chemical compositions of this powder was also obtained using the EDS for a selection of particles as well as a 10 min exposure to get a more accurate quantitative measurement of the compound.

[1] After sintering Ti6Al4V + nano hydroxyapatite scaffolds

C.2.2. Summary of methods section

Noteworthy were the troubles with mixed compositions of Ti6Al4V and hydroxyapatite. Prior to sintering and characterization this nano hydroxyapatite material was causing clogs. And, as will become apparent in the subsequent chapter its post processing failed to achieve sintering. Going forward the results section will elaborate on how these hydroxyapatite samples appeared under SEM, and why that doesn't bode well for mechanical performance.

C.3. Results

C.3.1. Morphology of Ti6Al4V combined with nano hydroxyapatite

Mixtures of Ti6Al4V and nano Hydroxyapatite in 9:1 ratios by weight were created in two different ways. The first method used dry mechanical alloying, and the second method used wet ball milling in ethanol. Resulting ink mixtures after extrusion and before and after sintering were distinctly different in appearance as can be seen in Figure C.2. The unsintered mechanically alloyed mixture had distinct chucks of HA and it was no longer nanosized, in contrast wet balling did maintain the nanosized nature and it had covered the spherical titanium particles to the point pores between particles were obscured. Neither mixture truly sintered, and Figure C.2c and C.2d both have spherical titanium particles without neck formation between them.

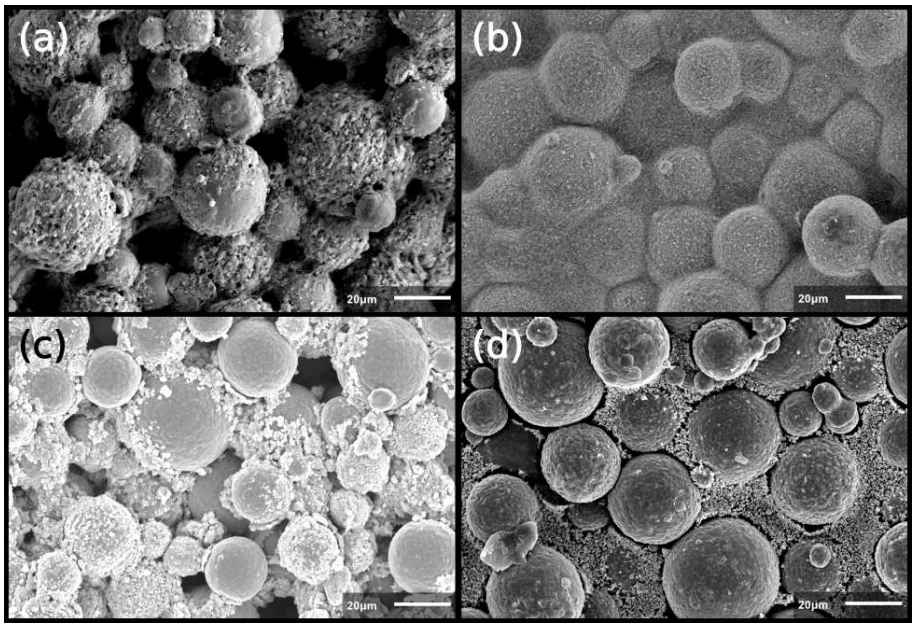

Figure C.2: Ti6Al4V/hydroxyapatite mixtures prepared in two different ways in sintered and unsintered state: (a) mechanically alloyed unsintered, (b) wet ball milled unsintered, and (c) mechanically alloyed after sintering, and (d) wet ball milled after sintering

C.3.2. Ti6Al4V/HA scaffolds before and after sintering

The multi composition scaffold consisting of 16 layers of Ti6Al4V and 16 layers of Ti6Al4V:HA composite in 9:10 ratio by weight had been sintered under the same $1200\,^{\circ}$C for 2 h conditions. The side that contains only Ti6Al4V has far progressed sintering (Figure C.3c), individual spherical particles can barely be made out anymore. There is a discrepancy between the settings, such as time and temperature, and the actual sintering conditions. The scaffold temperature during sintering may have been near $1200\,^{\circ}$C while that of other scaffolds, which didn't see this progressed sintering, may have been lower. While it wasn't possible to sand and polish the interface due to fragility, Figure C.3d illustrates the issue: Ti6Al4V + HA (left side) is practically unsintered while the Ti6Al4V (right side) is densely sintered.

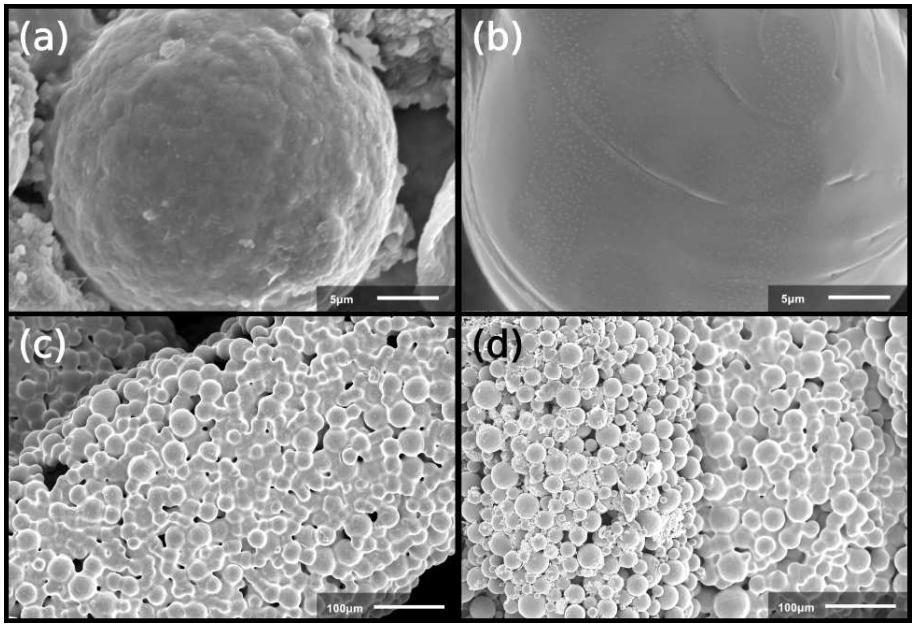

Figure C.3: Multimaterial scaffolds of Ti6Al4V and Ti6Al4V + hydroxyapatite mixtures: (a) Ti6Al4V particle with HA sintered, (b) Ti6Al4V particle without HA sintered, and (c) top side strut (Ti6Al4V) sintered, and (d) the Ti6Al4V-Ti6Al4V+HA interface

C.3.3. EDS results

EDS is a mostly qualitative analysis method, and not particularly suited for quantitative analysis. The low atomic number elements such as oxygen and carbon have less breaking radiation, few counts are to be expected and this reduces the accuracy of such elements further. Additionally, the penetration depth of EDS limits it to superficial analysis.

Ti6Al4V/HA scaffolds before and after sintering

The EDS results performed before and after sintering were inconclusive, it wasn't possible to tell the difference based on the results. The exception to this is that a small iron contamination was found in on measurement performed on the sintered sample. Though this contamination must have existed in the un-sintered sample as well, yet wasn't detected there.

The EDS results would show a majority calcium and phosphorous when the target was a clearly distinguishable hydroxyapatite particle, and when the target was a Ti6Al4V particle it would show almost exclusively titanium and aluminium, vanadium was absent from the results in all but one measurement. Determining the apatite content was thus not possible with the point measurements with short (1 min). A more reliable method would be to measure a larger surface and use a long integration times of several minutes as is performed in the next section on one of the pieces.

Boat scrapes
The materials recovered from the alumina crucible was found to consist of aluminium and calcium. There were also small amounts of carbon and oxygen present, very possibly high melting point tar left over from debinding. The analysis results can be seen in Figure C.4. A longer exposure (10 min) was also performed on piece number 5 which had 67.5, 18.1, 9.5, 4.9 w% of aluminium, calcium, carbon, and oxygen, respectively. For this EDS measurement an area of 18 x 12 µm was taken instead of a point.

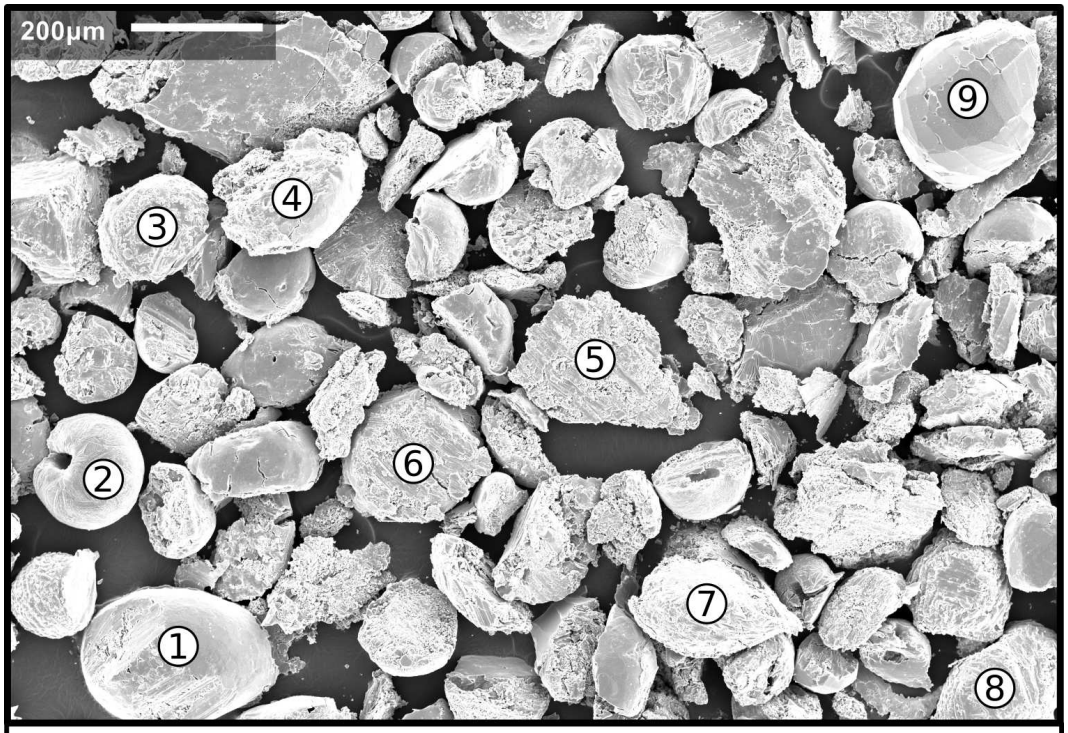

#	C	O	Al	Ca	Ti
1	18.84	3.84	69.44	7.31	0.57
2	16.86	-	59.39	23.74	-
3	18.58	-	58.03	23.38	-
4	17.09	-	71.48	11.43	-
5	19.77	1.40	71.62	7.21	-
6	11.15	-	67.15	23.52	-
7	14.60	2.02	59.87	23.52	-
8	12.68	-	60.41	26.91	-
9	18.78	-	57.65	23.07	-

Figure C.4: EDS results of the material recovered from the crucible

C.4. XRD results

The mixed material scaffold consisting of the Ti6Al4V and nano hydroxyapatite spectra are given in Figure C.5. There are two compounds containing iron which are contaminants, likely introduced during the ball milling. Additionally, no hydroxyapatite ($Ca_5(PO_4)_3OH$) phase exists anymore, and non of the phases contain calcium.

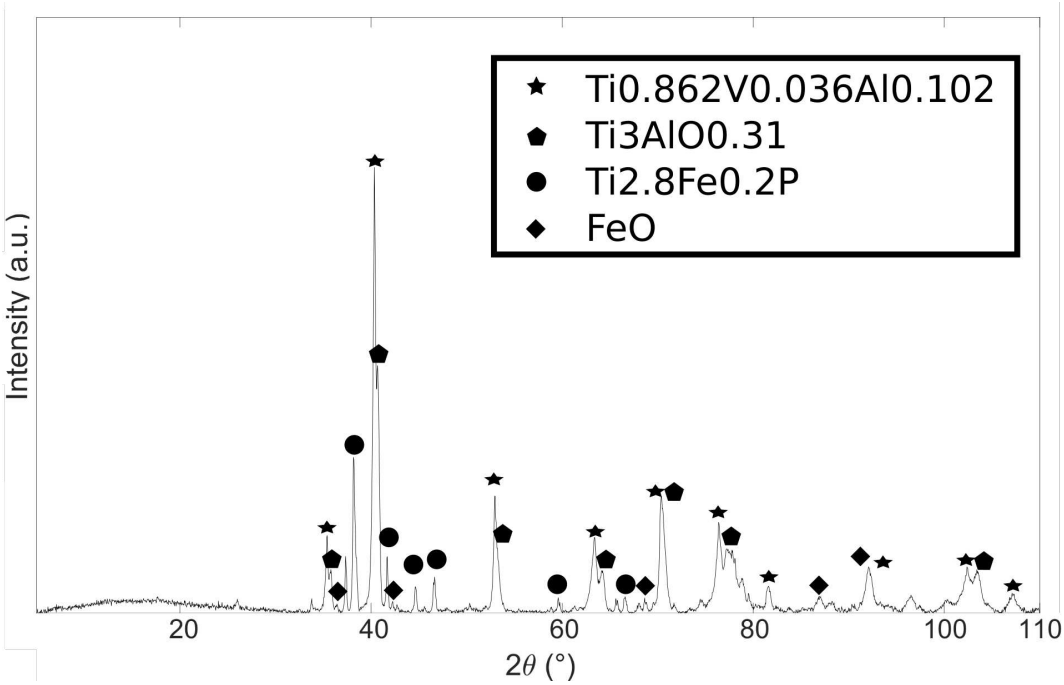

Figure C.5: XRD spectra of Ti6Al4V/HA scaffold

C.4.1. Summary of results section

Results from the various characterization methods were presented in this chapter. The most noteworthy result is that Ti6Al4V + hydroxyapatite composite did not sinter under any conditions.

C.5. Discusion - Challenges of Atmospheric Pressure Sintering for Ti6Al4V and Nano Hydroxyapatite Composite

In this research Ti6Al4V + nano hydroxyapatite scaffolds have been prepared in two different ways. Neither method resulted in successful sintering as was confirmed by the SEM results in Section C.3.2. Additionally, a degradation of the hydroxyapatite and a reaction with the aluminium in Ti6Al4V was also found to have occured. The reaction with the aluminium was deduced from metallic residue, found on the crucible after attempted sintering. Phase changes were found in XRD results, and calcium compounds were completely absent. However, EDS measurements of Ti6Al4V + nano hydroxyapatite scaffolds that had undergone a sintering attempt were found to still[2] contain some calcium.

Bulina et al conducted a study into the thermal stability of hydroxyapatite [10], and while it was found that it can be sintered or even melted without decomposition that was only possible under certain conditions. Two conditions were specified: First the calcium to phosphorous ratio has to be 1:1$\frac{2}{3}$, which is the stoichiometric ratio also found in hydroxyapatite. When this ratio was lower (calcium deficient) rapid conversion to calcium phosphates occurred at intermediate temperatures ($1000\,^{\circ}$C for 2 h). When the ratio was higher (phosphorous deficient) lime (CaO) was formed. The second condition given was that a high heating rate was required in order to minimize the breakdown of the hydroxide groups (dehydroxylation), which is said to begin at only $600\,^{\circ}$C. The furnace used in this thesis project did not have a high heating rate (it was $10\,^{\circ}\text{C}\,\text{min}^{-1}$), methods such as spark plasma sintering and laser heating can achieve higher rates. With these higher rates, sintering or even melting can occur before dehydroxylation decomposes the material.

[2] Perhaps the peaks of calcium compounds were obscured by others in the XRD analysis.

C.6. Conclusion - Ti6Al4V and Hydroxyapatite Composites

While this previously mentioned study shines some light on the cause of the failure, it is only focused on pure hydroxyapatite and not composites with other materials. The EDS analysis of the metallic crucible residue indicates that there is an aluminium calcium compound forming that can evaporate and deposit at the elevated temperatures. The Ti6Al4V alloy has excellent mechanical properties attributed to aluminium and vanadium stabilizing this alloy, however, the aluminium might react with calcium compounds at elevated temperatures and lead to undesirable results. For all these reasons it would be ill advised to attempt creation of such compositions, unless the sintering process can achieve an exceptionally high heating rate. Spark plasma sintering can hit these high sintering rates and has recently been demonstrated [71] to be preformed pressure-less on a 3D printed porous Ti6Al4V alloy scaffold.

D

Appendix - Flow rate dependence on cartridge fill level

During the manufacturing of the scaffolds using the Gesim Bioscaffolder, a gradual reduction in flow rate was observed every time. Initially, the hypothesis was that ink was drying on the nozzle tip and preventing outflow thus reducing the flowrate at a certain pressure. However, when the print was paused and the nozzle cleaned the flowrate did not recover to the initial value. The inks were homogenous and temporally stable so those couldn't have been factors either.

The ink during printing was contained in a Nordson EFD cartridge sealed with a piston. The piston prevents spills, but more importantly it prevent the pressurized driving gas from blowing a hole through the ink. This combination of a piston and cartridge are what made the flowrate dependant not only on ink rheology, pressure, and downstream conditions[1], but also on the position of the piston.

The piston in question is a thin flexible part that tightly seals against the walls of the cartridge. However, the walls of the Nordson EFD cartridges are not straight towards the dispensing end, instead they have a slight taper. As more of the ink is dispensed the diameter decreases, the fit between the piston and cartridge wall becomes tighter and tighter. an increasing amount of the force exerted on the piston by the pressurized gas is canceled out by friction between the piston and the cartridge wall. As a result of this the flowrate gradually decreases as the piston moves down during printing. While the reduction is small it can lead to underextrusion and print failure.

[1] nozzle size, nozzle shape, layerheight.